

# **Data Compression in Ultrasound Computed Tomography**

Zur Erlangung des akademischen Grades eines

**DOKTOR-INGENIEURS**

von der Fakultät für  
Elektrotechnik und Informationstechnik  
der Universität Karlsruhe (TH)  
genehmigte

**DISSERTATION**

von  
Dipl.-Ing. Rong Liu  
geboren in Xi'an

Tag der mündlichen Prüfung: 14.04.2011  
Hauptreferent: Prof. Dr. rer. nat. Olaf Dössel  
Korreferent: Prof. Dr. rer. nat. Hartmut Gemmeke

Ich versichere wahrheitsgemäß, die Dissertation bis auf die dort angegebene Hilfe selbständig angefertigt, alle benutzten Hilfsmittel vollständig und genau angegeben und alles kenntlich gemacht zu haben, was aus Arbeiten anderer und eigenen Veröffentlichungen unverändert oder mit Änderungen entnommen wurde.

---

(Rong Liu) Karlsruhe, den März 9, 2011

## **Abstract**

The large amount of data in the Karlsruhe 3D Ultrasound Computed Tomography (USCT) of about 20 GBytes per 3D dataset has to be reduced considerably to accelerate the data acquisition and analysis, and to reduce the necessary storage space. Ultrasound signals instead of images were compressed. The state-of-the-art and newly proposed compression methods were analyzed and implemented.

A software system was designed to support the development of data compression methods. A new lossless data compression, i.e. a cascade bit-wise run length method, was developed and compared with the state-of-the-art lossless data compression methods. Lossy compression methods were recommended for a higher compression ratio. The parameters of discrete wavelet transform, multi-fractal analysis, continuous wavelet transform, discrete cosine transform and spiking deconvolution based methods as well as a peak detection method and its modified version were adapted for data compression with a reduction of noise. Their computational complexities were compared.

A new evaluation scheme for comparison of compression methods was proposed. A comparison of reconstructed images instead of compressed signals was used to evaluate compression methods of ultrasound signals. As objective image quality estimators non reference and reference based estimators were investigated and compared. The original image achieved with the uncompressed datasets and an ideal reference image achieved with simulated datasets were constructed as reference image. Optical flow based and a committee model based image quality estimator were newly designed. The limitations of the optical flow based estimator were discussed. The committee model based estimator combines the advantages of different state-of-the-art image quality scores.

Finally, a discrete wavelet based data compression method at a compression ratio 15 was suggested for compression of USCT datasets.

# Acknowledgements

I would like to thank Professor Hartmut Gemmeke and Professor Olaf Dössel for giving the opportunity to pursue my PhD in Karlsruhe Institute of Technology. I benefited many from their great scientific attitude.

I thank my colleagues in Institute for Data Processing and Electronics and Institute of Biomedical Engineering. I'm extremely thankful to my lab members from the project Ultrasound Computed Tomography for their constant support and advice throughout the course of my PhD work.

I also thank my family, especially my husband Jianfeng Xu, my father Shuxin Liu, my mother Yuzhen Wu and my son Yiming Xu for their continuous and generous support.

Last but not least, I would like to express my gratitude to all those who helped me during the writing of this thesis.

# Contents

<b>Abstract</b>	<b>I</b>
<b>Acknowledgements</b>	<b>II</b>
<b>List of abbreviation</b>	<b>VI</b>
<b>1 Introduction</b>	<b>0</b>
1.1 Background . . . . .	0
1.2 Motivation and aim . . . . .	0
1.3 Contributions of the thesis . . . . .	1
<b>2 Search for suitable compression algorithms</b>	<b>5</b>
2.1 Signal compression in literature . . . . .	5
2.1.1 Definition . . . . .	5
2.1.2 State-of-the-art . . . . .	5
2.2 Characteristics of 3D USCT . . . . .	8
2.2.1 Experimental setup . . . . .	8
2.2.2 Data acquisition . . . . .	8
2.2.3 Image reconstruction . . . . .	9
2.3 Analysis of ultrasound signals in USCT . . . . .	12
2.3.1 Introduction . . . . .	12
2.3.2 Wave equation in tissue . . . . .	12
2.3.3 Model for A-scans . . . . .	14
2.3.3.1 Coded excitation . . . . .	14
2.3.3.2 Construction of model . . . . .	15
2.3.4 Multiple scattering . . . . .	17
2.3.5 Attenuation and dispersion . . . . .	20
2.4 New lossless compressions . . . . .	21
2.4.1 Compression based on neighboring A-scans . . . . .	21
2.4.2 Compression based on neighboring samples . . . . .	23
2.4.3 Cascading bitwise run length encoding . . . . .	24

2.4.4	Lossless compression in frequency domain . . .	26
2.4.5	Validation of adjacent A-scans and samples . . .	26
2.4.6	Validation of bitwise run length encoding . . . . .	28
2.5	Lossy compression methods . . . . .	29
2.5.1	Time domain based methods . . . . .	31
2.5.1.1	Threshold . . . . .	31
2.5.1.2	IK peak detection . . . . .	32
2.5.1.3	Modified IK algorithm . . . . .	33
2.5.1.4	Spiking deconvolution . . . . .	33
2.5.2	Frequency domain based methods . . . . .	34
2.5.2.1	Discrete cosine transform . . . . .	34
2.5.3	Time and frequency domain based methods . . .	35
2.5.3.1	Discrete wavelet transform . . . . .	35
2.5.3.2	Multi-fractal analysis . . . . .	36
2.5.3.3	Continuous wavelet transform . . . . .	37
2.5.4	Comparison of different compression methods .	38
2.6	Properties of adapted lossy compression . . . . .	42
2.6.1	Computational complexity . . . . .	42
2.6.1.1	Theoretical analysis . . . . .	42
2.6.1.2	Computing time . . . . .	44
2.6.2	Denoising ability of compression methods . . . .	46
2.6.2.1	Simulation of noisy datasets . . . . .	46
2.6.2.2	Compression of noisy datasets . . . . .	46
<b>3</b>	<b>Evaluation of signal compression methods</b>	<b>49</b>
3.1	Introduction . . . . .	49
3.1.1	An image quality based evaluation method . . . .	50
3.1.2	Terminologies and analysis . . . . .	51
3.1.3	Requirements and difficulties . . . . .	54
3.1.4	Summary . . . . .	56
3.2	Image quality estimators in literature . . . . .	56
3.2.1	Subjective estimators . . . . .	56
3.2.2	Objective estimators . . . . .	57
3.3	Assessment of no-reference image quality estimators .	59
3.3.1	Selected no-reference estimators . . . . .	59
3.3.2	Artificial images and distortions . . . . .	61
3.3.3	Analysis results . . . . .	62
3.4	Quality estimators with a reference . . . . .	63
3.4.1	Selected reference based estimators . . . . .	65
3.4.2	An optical flow based estimator . . . . .	68

3.4.2.1	Optical flow . . . . .	68
3.4.2.2	Design of estimator . . . . .	69
3.4.2.3	Assessment of performance . . . . .	70
3.4.3	Committee model based estimators . . . . .	70
3.4.3.1	Motivation . . . . .	70
3.4.3.2	Structure of committee model . . . . .	72
3.4.3.3	Training process . . . . .	72
3.4.3.4	Training cases . . . . .	74
3.4.3.5	Simulated distortions in USCT images . . . . .	74
3.4.4	Evaluation of reference based estimators . . . . .	76
3.5	Achieving a reference for evaluation . . . . .	77
3.5.1	Original image based reference . . . . .	77
3.5.1.1	Analysis of original images . . . . .	77
3.5.1.2	Filtered original images . . . . .	77
3.5.1.3	Assumptions . . . . .	78
3.5.2	Simulated reference . . . . .	78
3.5.2.1	Imaged objects . . . . .	79
3.5.2.2	Design of an ideal reference . . . . .	83
3.5.2.3	Simulated USCT datasets . . . . .	86
3.5.2.4	Evaluation process . . . . .	88
<b>4</b>	<b>Results</b>	<b>90</b>
4.1	Evaluation of data compression by comparing A-scans . . . . .	90
4.1.1	Compression of synthetic A-scans without noise . . . . .	90
4.1.2	Compression of noisy A-scans . . . . .	92
4.2	Evaluation of data compression by comparing images . . . . .	98
4.2.1	Simulated datasets . . . . .	98
4.2.1.1	Compressed datasets . . . . .	98
4.2.1.2	Scores of standard estimators . . . . .	107
4.2.1.3	Scores of optical flow based estimator . . . . .	118
4.2.1.4	Scores of the committee model based estimator . . . . .	119
4.2.1.5	Filtered original images as reference . . . . .	120
4.2.1.6	Different mother wavelets . . . . .	123
4.2.2	Real datasets . . . . .	127
4.2.2.1	Imaged objects and compressed datasets . . . . .	127
4.2.2.2	Filtered original images as reference . . . . .	131
4.2.2.3	Designed ideal reference . . . . .	131
4.2.2.4	Scores with CMM . . . . .	132
4.3	Evaluation of data compression with human perception . . . . .	133

4.3.1	Simulated datasets . . . . .	134
4.3.2	Real datasets . . . . .	134
4.4	Validation of denoising ability . . . . .	135
4.4.1	Noisy datasets . . . . .	135
4.4.2	Compression of noisy datasets . . . . .	135
4.4.3	Scores of denoising datasets . . . . .	136

**5 Discussion and conclusion 146**

5.1	Discussion . . . . .	146
5.1.1	Multiple scattering and dispersion . . . . .	146
5.1.2	Image quality estimators . . . . .	147
5.1.2.1	No-reference estimators . . . . .	147
5.1.2.2	Standard reference based estimators . . . . .	147
5.1.2.3	New image quality estimators . . . . .	148
5.1.3	Comparison of results with different types of references . . . . .	149
5.1.3.1	Original image as reference . . . . .	149
5.1.3.2	Ideal reference . . . . .	150
5.1.3.3	Filtered original image as reference . . . . .	150
5.1.4	Lossless compression . . . . .	151
5.1.5	Lossy compression . . . . .	151
5.2	Conclusion . . . . .	154
5.2.1	Compression . . . . .	154
5.2.1.1	De-noising ability and computational complexity . . . . .	154
5.2.1.2	Property and performance . . . . .	155
5.2.2	Image quality estimators . . . . .	157
5.2.3	Acceptable data compression in USCT . . . . .	157

## List of abbreviation

USCT	Ultrasound computed tomography developed at KIT
SAFT	Synthetic aperture focussing technique
IKstd	Standard IK peak detection methods
IK	Modified IK algorithm
DWT	Discrete wavelet transform based compression
DCV	Spiking deconvolution
DCT	Discrete cosine transform based compression
MultiFractal	Multi-fractal transform based compression
WavePDT	Continuous wavelet based peak detection method
MTF	Modulation transfer function
PSNR	Peak signal to noise ratio
SSIM	Structure similarity measure
AMI	Average mutual information
NMI	Normalized mutual information
Homog	Homogeneity based measure
GVFMI	Gradient Vector Flow (GVF) and AMI
NormGrdt	Normalized gradient vector
GVF	Gradient Vector Flow
OFintenEtpy	Optical flow based estimator
CMM	Committee model based estimator
MVS	Mean vote score
RLE	Run length encoding
TOA	Time of arrival of ultrasound pulse

# Chapter 1

## Introduction

### 1.1 Background

Ultrasound computed tomography (USCT) is developed at KIT aiming at a new medical imaging system for early detection of breast cancer which is the most common cause of cancer death among women in Europe [1]. Compared with the commonly used modalities, such as breast self-exam, X-ray mammography, magnetic resonance imaging (MRI) and conventional ultrasound imaging, USCT is a low cost and non-invasive instrument with low speckle noise and high resolution for breast cancer diagnosis [2, 3, 4, 5].

An experimental result with a specially designed phantom represents the high resolution of images in USCT [6, 7]. This phantom is constructed with a plastic cylinder in which 15 nylon threads are mounted parallel to the axel of the cylinder. The diameter of each nylon thread is 0.1 mm. These nylon threads can be seen clearly in the reconstructed image in Fig. 1.1. Encouraged by the high resolution of this reconstructed image, a 3D USCT was developed. The used results are from a subset in 2D.

### 1.2 Motivation and aim

More than 20 GBytes of raw data are necessary in 3D USCT to reconstruct a 3D USCT image [8]. Such a large amount of data is costly to be stored, transported and processed. E.g. it takes about one week with one PC (Pentium 4, 3.2 GHz, 2.0 GB RAM) for reconstruction of a 3D image with a binning of  $225 \times 225 \times 392$ . The large amount of data limits the utilization of USCT.

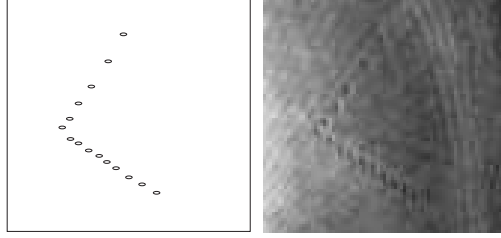


Figure 1.1: The scheme for the cross section of nylon threads which has a diameter of 0.1 mm, is represented with the black point on the left side of the image. The reconstructed image with the USCT system is shown on the right side.

According to the storage capacity and the reconstruction time, it is highly desirable to reduce the amount of data considerably. The ultrasound signal includes contents about tissues, noise and redundancies. The possible reduction rate is based on the content of tissues in the ultrasound signals.

A suitable method of data compression has to be found for reducing the amount of data. The compression method should be used for ultrasound signals in USCT with considerably reducing the amount of data without losing the information of imaging objects, i.e. only the irrelevant data should be removed. The second challenge is to find an estimator for the quality of images comparing the different methods and stages of data compression.

### **1.3 Contributions of the thesis**

Ultrasound signals instead of images were compressed in this work. Millions of ultrasound signals from the same dataset had to be compressed. The state-of-the-art and newly proposed compression methods were analyzed and implemented based on the characteristics of ultrasound signals in 3D USCT. A new evaluation scheme for comparison of compressed signals was proposed. The evaluation results were used to evaluate the compression methods. The estimators used in the evaluation scheme were discussed and analyzed.

The definition of the data compression and an overview of the state-of-the-art data compression methods were given in section 2.1. The USCT setup was introduced in section 2.2 in which the reconstruction method and the characteristics of reconstructed images were

explained.

A software system was designed to support the development of data compression methods. This system made the implementation and evaluation of data compression independent of the formats of datasets which were changed with the version of USCT instruments. In this system the implemented compression methods, parameters and estimators in the evaluation scheme were replaced flexibly by the users to optimize data compression in USCT.

A new lossless data compression was developed and compared with the state-of-the-art lossless data compression methods. The distributions of least and most significant bits of datasets were analyzed. The property of this distribution was utilized to design a cascade bit-wise run length method.

Lossy compression methods were recommended because they resulted in a higher compression ratio relative to lossless methods. The parameters of discrete wavelet transform, multi-fractal transform, continuous wavelet transform, discrete cosine transform and spiking deconvolution based methods were adapted for the data in USCT and were tested with a large range of compression ratios. In addition, a peak detection method and its modified version were implemented for data compression to preserve more useful information at a high compression ratio.

The ultrasound signals in USCT were analyzed in section 2.3. Based on this analysis the newly developed lossless compression method was explained in section 2.4. The parameter optimization of state-of-the-art lossy compression methods to USCT datasets were described in section 2.5.

Noise as irrelevant component of ultrasound signals was reduced during data compression. The computational complexity of different compression methods was analyzed and compared. The computational complexity and the denoising ability of the adapted lossy compression methods were discussed in section 2.6.

Evaluation methods for the compressed signals instead of images were reviewed. A comparison of reconstructed images instead of compressed signals was used to evaluate compression methods of ultrasound signals. The basic ideas of image quality based assessment method for data compression were proposed in section 3.1.

Additionally, the difficulties and the hypotheses of designing this assessment system were explained at the end of this section.

The state-of-the-art and newly designed image quality estimators for scoring image quality were analyzed. As objective image quality estimators non-reference and reference based estimators were researched. The performance of non-reference and reference based estimators was discussed by comparison with the subjective image quality estimator.

Firstly, non-reference estimators for evaluation of the image quality were considered to avoid designing a reference image. The theoretical and experimental analyses were carried out to find a suitable non-reference method.

Secondly, reference based image quality estimators were analyzed in this work. The original image of USCT achieved with the uncompressed datasets was reconstructed and filtered as reference image for evaluation of compressed datasets.

An ideal reference image was achieved with simulated datasets of 3D USCT for implementation of reference based image quality estimators. The imaged objects in the ideal reference images were designed with a-priori defined positions and acoustic properties. These simulated datasets were also used to analyze the compression methods as well as the imaging properties of whole USCT system.

Two reference based image quality estimators were newly designed to overcome the disadvantages of state-of-the-art image quality estimators. The first designed image estimator was the optical flow based estimator. This estimator was tested in the evaluation system of image quality. The limitations of this estimator were discussed; The second designed estimator was the committee model based estimator. The advantages of different state-of-the-art image quality scores were combined to construct a generalized committee and implemented for USCT.

An overview of the state-of-the-art subjective and objective image quality estimators was given in section 3.2. The disadvantages of no-reference image quality estimators were analyzed in section 3.3. The selected and newly designed reference based estimators for comparison of the compression methods were introduced in section 3.4. The reference images were designed in section 3.5.

Finally, a discrete wavelet based data compression method was suggested which is based on the experimental results with simulated and real datasets. The experimental results for simulated and real USCT datasets were described in chapter 4. These results combined with the methods introduced in this thesis were summarized in chapter 5.

## Chapter 2

# Search for suitable compression algorithms

### 2.1 Signal compression in literature

#### 2.1.1 Definition

In this thesis data compression is used to reduce data amounts without loss of relevant contents. The procedure of data compression is a transfer of the information into another description format with less storage and considerable lower load by data transmission [9]. The consequence of data compression is removing the redundancy or the irrelevant information in the data [10]. The irrelevant and interesting contents are given by users according to the characteristics of data and to the concrete implementation of data compression.

The definition of compression ratio (CR) used in this work is the ratio between the amount of data before and after compression [11].

$$CR = \frac{\text{Amount of input data}}{\text{Amount of output data}}. \quad (2.1)$$

#### 2.1.2 State-of-the-art

After the first data compression method developed by Samuel Morse in the 1830s for transmitting information with short code-words in telegraphy, many compression algorithms were developed during the past hundred years [12, 13].

Compression methods are classified into lossless and lossy com-

pression. Compression is defined as lossless if the whole data can be reproduced after decompression, whereas lossy compression eliminates some parts of information in the data permanently [14, 15].

The lossless compression methods are commonly used for text compression to retrieve the complete information from the compressed dataset. Lossy compressions are mostly employed for visual or audio data tolerating some level of quality degradation.

Run Length Encoding (RLE) is the simplest lossless compression method for reduction of the redundancy. One of the most commonly used lossless compressions is the Lempel-Ziv-Welch (LZW) method. The data are analyzed based on the probability of the content. A table is constructed for replacing the repeated content of data by a code. This table is pre-generated and dynamically updated by changing the length of the code for a high compression ratio [16].

The theoretical optimal compression ratio of lossless methods is calculated with the entropy of datasets  $H$  which is defined as follows:

$$H = - \sum_{i=1}^m p_i \log_2 p_i \quad [bits/symbol] \quad (2.2)$$

where  $p_i$  is the probability for the appearance of the  $i^{th}$  symbol.  $m$  is the number of possible symbols in the whole dataset [17]. In case  $L$  bits are used to save each sample of the dataset, the theoretical highest compression ratio  $CR_h$  is calculated as follows [18]:

$$CR_h = \frac{L}{H} \quad (2.3)$$

The advantage of a lossless method is the perfect recovery of the original data. However, the lossless methods have a low compression ratio. The compression ratio of lossless compression is usually smaller than 3. The low compression ratio limits the application of lossless compression methods [19, 20].

In order to reach a high compression ratio, lossy compression is developed. The state-of-the-art standard for lossy data compression of images is JPEG2000 which is based on a wavelet transform. The JPEG2000 is an improved version of the standard JPEG using the discrete cosine transform. The images compressed with JPEG2000 are proved to have a higher compression ratio and a lower quality

degradation than with JPEG [21, 22]. The most commonly used standard for video data is MPEG [23] which employs JPEG to compress a frame in video and utilizes prediction between neighboring frames to achieve a higher compression ratio than JPEG.

Lossy compression methods are based on the assumption that there are irrelevant or redundant contents in data. The irrelevant contents are expected to be removed and the rest contents are stored with the most compact data format. The compression ratios of the lossy methods depend upon the ratio of removed contents and the compact data format.

In case irrelevant content in the data is reduced during the data compression, the quality of the compressed data may be better than the original data [24]. Therefore it is important to remove the irrelevant content during lossy compression. The irrelevant contents of the data can be removed in the time/space domain directly, e.g. by a peak detection method, or in the frequency domain after a transformation, e.g. by discrete cosine transform based data compression. The state-of-the-art transformation used for data compression is the wavelet transform which can be used to represent the information of data in both time/space and frequency domains [25, 26]. In order to utilize the available characteristics of data, e.g. the pulse shape information in a signal, the selected mother wavelet is expected to have similar characteristics as the pulse shape. Another method to use the information of the pulse shape is deconvolution based compression, whose performance is influenced strongly by pulse deformation and noise in datasets [27].

The new theory of compressive sampling [28] is based on the assumption that the information in a signal can be represented by undersampled datasets. But to apply this theory to data compression suitable sensing waveforms have to be found.

There are no standard compression methods specially designed for ultrasound data which are employed widely for different applications with different data characteristics [29]. The state-of-the-art data compression methods are reviewed to find a suitable data compression method for USCT. Based on the properties of these compression methods, some of them will be selected and adapted for USCT based on the characteristics of ultrasound signals.

A further question is at which stage compression should be applied

to USCT. USCT data include measured data and reconstructed images. The measured data consist of ultrasound signals termed as A-scans. Compression methods are used for A-scans instead of reconstructed images, because the amount of measured data is larger than that of reconstructed images depending on the chosen resolution of images.

## 2.2 Characteristics of 3D USCT

### 2.2.1 Experimental setup

The Karlsruhe USCT setup is designed to image human breasts by ultrasound signals which are emitted and received by ultrasound transducers and propagated through breast tissues. The schematic drawing of the imaging process with the USCT setup is shown in Fig. 2.1. One breast of a patient is immersed into a rotatable cylindrical container which is filled with water as the coupling medium with a diameter of 18.3 cm and a height of 15 cm.

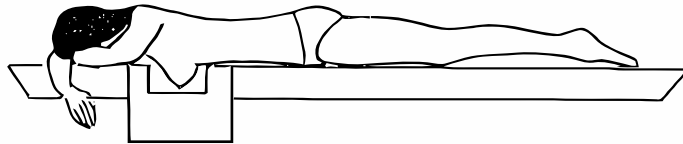


Figure 2.1: Schematic drawing of imaging with USCT.

The ultrasound signals are emitted and received by 48 transducer arrays which are mounted on the wall of the container and grouped into three horizontal layers with 16 arrays per layer. Each transducer array includes 8 emitting and 32 receiving transducers (see Fig. 2.2). The cylindric container is rotated to 6 positions with 3.75 degree per rotation step. The rotation of the cylinder results in more positions of transducers, thus to increase the number of ultrasound signals and the image quality.

### 2.2.2 Data acquisition

The transducers emit ultrasound pulses one by one with a time difference of  $600 \mu s$ . One pulse is emitted and all of the receivers start to acquire the ultrasound signals, so-called A-scans, simultaneously. Thus the number of received A-scans is the combination

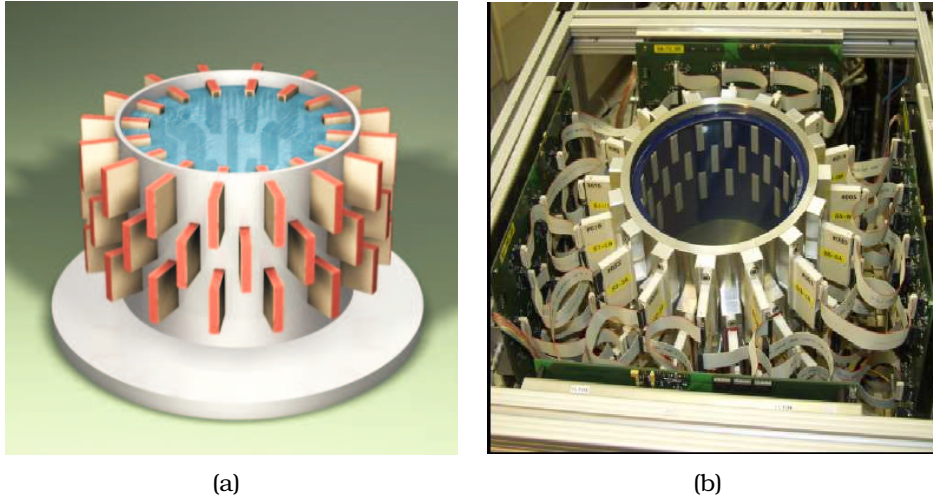


Figure 2.2: Schematic drawing (a) and real device (b) for 3D USCT.

of possible emitter and receiver positions, i.e. 3.5 Million. Each A-scan is saved with 6000 Bytes, therefore one dataset has a size of 21 GBytes.

The received A-scans are denoised with an analog filter and sampled with a frequency of 10 MHz. Each sample of the A-scans is registered with a width of 12 bits. 192 channels are digitized and transferred word-wise to a PC. In order to reduce noise, each A-scan is measured  $n$  times and the averaged A-scan is saved [30].

### 2.2.3 Image reconstruction

The original data in the PC is reconstructed to a 3D image with the method of synthetic aperture focusing technique (SAFT). A scheme of the reconstruction method is represented in Fig. 2.3. The circle stands for a cross section of the rotatable cylindrical container. The blue area is the water. Each sample of the reflected pulses in A-scans is projected to an ellipsoid in the reconstructed image. These ellipsoids are accumulated to construct one 3D image. The red ellipse with the solid line corresponds to the cross section of the reconstructed ellipsoid in the 3D USCT image. The ellipsoids of the same A-scan have the same foci which are the positions of corresponding emitter and receiver. The yellow blocks at the boundary of the circle represent emitters and receivers. The geometrical parameters of the ellipsoid are calculated with the time position of the sample multiplied by the speed of ultrasound of the propagation

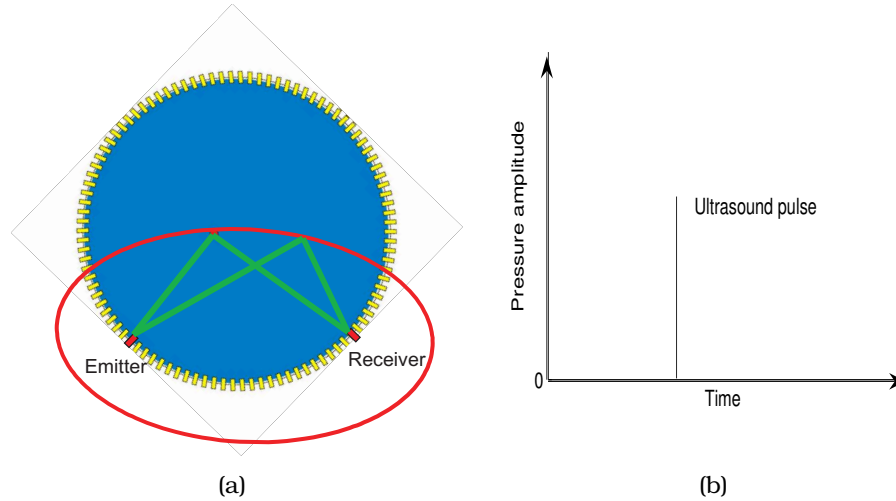


Figure 2.3: Scheme for image reconstruction ellipsoid (red) and information of corresponding ultrasound pulse. Horizontal and vertical axes stand for time and pressure amplitude, respectively.

medium and the position of the involved emitter and receiver. The green lines are the propagation paths of the ultrasound pulse reflected by two points on the ellipse. The gray value of each pixel on the ellipsoids corresponds to the pressure amplitude of the sample in the A-scans.

The image reconstructed with the SAFT method has low speckle noise because the scattered ultrasound signals from many different directions are considered. US imaging is coherent imaging by the use of interfering signals. The interference of scattered ultrasound signals results in speckle noise [31, 32, 33]. Speckle noise is considered as a negative impact for ultrasound images. Lots of research work has been done to remove speckle noise by utilizing its deterministic and multiplicative characteristics [34, 35].

In USCT images speckle noise is reduced significantly. USCT has the characteristics of coherent imaging. I.e. the media used to transfer signals contain many sub-resolution scatters [36]. However the speckle noise is invisible in the original images, due to a large amount of non-coherent overlapping ellipsoids resulting from different combined transducers [37]. Technical expression is spacial compounding [37]. The speckle noise in images reconstructed with compressed datasets may emerge due to the reduced number of ellipsoids, i.e. A-scans.

The image is reconstructed with a PC. The time used to reconstruct a 3D image depends on the characteristics of the used PC, the resolution of reconstructed images and the number of applied A-scans per image part. The image with a high resolution needs about a week using the 2006 version of the reconstruction method.

### **Characteristics and limitations of the reconstruction method**

The image reconstruction methods are based on the following assumptions:

1. **Sound speed assumption:** The basic assumption of the reconstruction method SAFT is that the ultrasound wave propagates through the breast with a constant speed. However the breast consists of media with various acoustic properties which results in an inhomogeneous sound speed distribution. Without individual correction of the speed of sound the imaged objects may not be precisely reconstructed, thus the quality of reconstructed images is influenced. The resulting images become blurred or show unforeseen positions of imaged objects. In order to overcome these shortcomings, the transmission pulse in A-scans is used to measure the ultrasound speed distribution in media and include the measured values into the analysis. The information about the ultrasound speed is now used to improve the quality of reconstructed images [38].
2. **Overlapping ellipsoids:** According to the reconstruction method SAFT, each sample of A-scans is used to draw an ellipsoid in the reconstructed image. I.e. for each combination of emitter and receiver positions one point of imaged objects is reconstructed as an ellipsoid. Only one point on this ellipsoid is relevant for the image of the object. By overlapping ellipsoids from different combinations of emitter and receiver positions the contrast of imaged objects increases; the irrelevant points of ellipsoids are going to be the background of reconstructed images. With increasing number of ellipsoids or measuring points the background is getting smaller and the contrast of the USCT images increases.

## **2.3 Analysis of ultrasound signals in USCT**

### **2.3.1 Introduction**

The center frequency of the used ultrasound wave is larger than the highest frequency of human hearing which is 20,000 Hz [39]. USCT uses an ultrasound pulse with a center frequency of approximately 2.3 MHz and the used transducer has a resonance frequency of 2.7 MHz. The advantages of ultrasound are low cost and non-invasiveness [40].

Ultrasound is widely used in medicine to image the internal organs of bodies with reflected ultrasound waves from the boundaries between tissues [41]. Besides the diagnosis of early breast cancer in USCT, the aims of using ultrasound as a medical imaging modality include observation of the condition and the behavior of fetus, locating tumors and the observation of human organs. Conventional ultrasound uses a focused wave front, however the ultrasound transducer in USCT has an open aperture for post beam forming [7].

In the following both simulated and real ultrasound signals are analyzed. Simulated signals are achieved based on the code Wave3000 which belongs to the software for simulation of the ultrasound signals in USCT [42]. These simulated ultrasound signals are used for studying compression methods. Real ultrasound signals are employed to understand the acoustic phenomena in USCT experiments.

### **2.3.2 Wave equation in tissue**

An ultrasound wave propagates mechanical energy through media, thus the wave equation is based on a mechanical model [43]. In this work the wave equations are used as the mathematical tools to describe the variation of ultrasound signals in USCT. The simulation of the ultrasound wave propagation in 3D USCT is based on these equations.

In the elastic mechanical model the media, i.e. breast tissues, are modeled as many ideal points with small mass, i.e. small volume elements of breast tissue, termed as “particles”. These particles vibrate near its equilibrium position by a displacement  $u$ . In case of wave propagation through the breast, these particles are displaced

and thus have a strain relative to their displacement  $u$ . According to Hooke's law, the strain of particle is linearly proportional to the stress on the particles. The stress is related to the displacement  $u$  by Newton's Second Law of Motion. Finally, the displacement is used to describe the spatial variation of particles with time by wave equation. The displacement of one dimensional wave equation is represented with the scalar field  $u$  and then the achieved one dimensional wave equation is a hyperbolic partial differential equation:

$$\frac{\partial^2 u}{\partial t^2} = c^2 \nabla^2 u, \quad (2.4)$$

where  $t$  is time and  $\nabla^2$  is the Laplace-operator.

In equation 2.4  $c$  is a constant and depends on the properties of the breast. The physical meaning of  $c$  is the speed of the ultrasound propagation in the media [39], i.e. between neighboring particles.  $c$  is also called group velocity.

In the above discussion, the acoustic properties of the breast are represented with a parameter  $c$  by assuming the breast tissues are isotropic. The constant  $c$  depends on two independent elastic constants, i.e. Lamé constants  $\delta$  and  $\mu$ , and the mass density  $\rho$  of the breast tissues. The relationship between them is:

$$\frac{1}{c^2} = \frac{\rho}{\delta + 2 \cdot \mu}, \quad (2.5)$$

where  $\delta$  is the 1<sup>st</sup> Lamé constant and  $\mu$  is the 2<sup>nd</sup> Lamé constant (also called rigidity modulus). If the properties of the breast tissues are considered as anisotropic, 36 elastic stiffness constants are necessary to represent the spatial variation of the particles in the wave equation 2.4 [44]. To simplify the analysis process of ultrasound signals in this work an isotropic model is employed.

Three dimensional elastic wave equation was used for simulation of wave propagation in medium in software Wave3000 [45]. The displacement in three dimensional equation is represented with the vector field  $\mathbf{u}$ . In the equation 2.4 the breast tissues are assumed to be lossless, whereas the real breast tissue in USCT is lossy and attenuates a part of ultrasound energy during the wave propagation. This attenuated energy is transformed into heat [46]. In order to show the attenuation properties of the breast tissues, a visco-elastic instead of elastic mechanical model is used to construct the wave equation. With the viscosity of the tissues the wave equation

is rewritten to

$$\rho \frac{\partial^2 \mathbf{u}}{\partial t^2} = (\mu + \eta \frac{\partial}{\partial t}) \nabla^2 \mathbf{u} + (\delta + \mu + \phi \frac{\partial}{\partial t} + \frac{1}{3} \eta \frac{\partial}{\partial t}) \nabla (\nabla \cdot \mathbf{u}), \quad (2.6)$$

where  $\phi$  and  $\eta$  are bulk and shear viscosity modulus and  $\nabla^2$  is the vector Laplace-operator.  $\nabla$  and  $\nabla \cdot$  stand for the gradient and divergence operators, respectively [45].

The equation 2.6 is then solved with the finite difference method. The solutions are used to simulate the variation of ultrasound signals in breast tissues. To solve this wave equation needs lots of computing time. The strength of scattered ultrasound pulses is unobvious to be observed in this equation. Therefore a model for A-scans has to be designed for analysis of scattered ultrasound pulses.

### 2.3.3 Model for A-scans

Each A-scan in USCT is obtained for a certain combination of ultrasound transducers. It is not easy to quantify the differences between different A-scans with a mathematic method. A simplified method for analysis of the ultrasound pulses in A-scans is to construct a model instead of solving a wave equation [47].

#### 2.3.3.1 Coded excitation

Coded excitation is a designed pulse shape of emitted ultrasound pulses. The center frequency and the band-width of the coded excitation in USCT are limited by the properties of the transducer and of breast tissue. Emitted pulses with high frequency content and wide band-width are strongly absorbed by the tissue, i.e. much energy will be damped during propagation [46]. Low frequency and narrow band-width result in a low resolution of USCT images. The selection of coded excitation is a trade-off between the image resolution and the acoustic attenuation of ultrasound waves.

The envelope of the used coded excitation is Gaussian with a center frequency of 2.3 MHz. The band-width is approx. 2 MHz. The coded excitation is simulated and plotted in Fig. 2.4 with a sampling frequency of 50 MHz. In the following complete simulations of the process are used. As emitter pulse shape a coded excitation is

shown in Fig. 2.4 to construct a model of an A-scan.

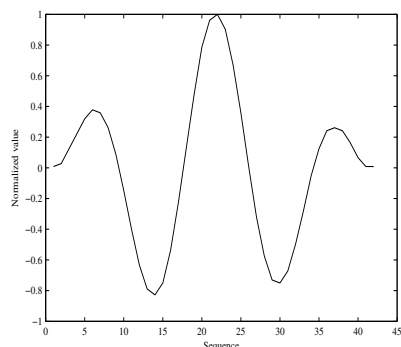


Figure 2.4: Coded excitation for a real dataset with a sampling frequency of 50 MHz and a center frequency of 2.3 MHz.

### 2.3.3.2 Construction of model

An A-scan records the time development at the receiver position. The length of an A-scan is  $300 \mu s$  which is decided by the sound speed and size of the USCT instrument. Not only the ultrasound pulse transfers directly from the emitter position to the receiver position, termed as the transmission pulse, but also the reflected pulses by different objects in USCT, called reflected pulses, are recorded in the A-scan. In case more reflected pulses reach the receiver position at the same time, these pulses are superimposed.

Fig. 2.5 shows a part of two real A-scans with the transmission and the reflected pulses. Both A-scans are recorded with the same emitter transducer but with different receivers. The system response characterized by the transmission signal is not identical to the coded excitation due to the frequency dependent attenuation of ultrasound waves and angular characteristics of transducers. The reflected pulses are superimposed with parts of the transmission pulses.

The reflected pulses in A-scans represent the scattered ultrasonic pulses arising from the boundaries between different tissues of the breast, e.g. between cancer and glandular tissue. The amplitude of scattered ultrasound pulse depends on the acoustic impedance difference between these tissues [29]. The positions of scattered

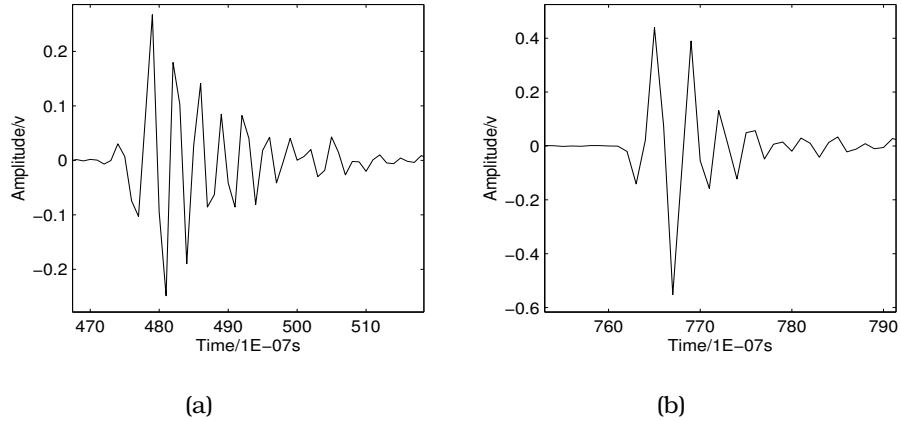


Figure 2.5: The transmission pulses from two real A-scans. These two A-scans are recorded with the same emitter and different receivers.

ultrasound pulses in the A-scans depend on the positions, where these boundaries occur.

Based on the above analysis a simplified model is constructed to simulate an A-scan, which is a superposition of many ultrasound pulses  $P_k$  with different amplitudes and time delays  $\tau$ :

$$P_k(t) = A_k \cdot \hat{f}_k(t) \otimes \delta(t - \tau_k) \quad (2.7)$$

where  $k$  is the index of the ultrasound pulses in an A-scan and  $t$  stands for time.  $A_k$  and  $\hat{f}_k(t)$  are the corresponding amplitude and pulse shape function, respectively.  $\delta(t - \tau_k)$  denotes the time delay function at the time of arrival  $\tau_k$  (TOA).

The measured pulse shape described by equation (2.7) is strongly correlated to the applied coded excitation  $f$  (in section 2.3.3.1). The difference between the recorded ultrasound pulse  $\hat{f}$  and coded excitation  $f$  is the pulse deformation. One of the most important reasons for the pulse deformation is the acoustic attenuation in tissues. Other reasons include angular dependent characteristics of the impulse response for emitters and receivers, refraction and diffraction.

An A-scan consists usually not only of transmitted and reflected

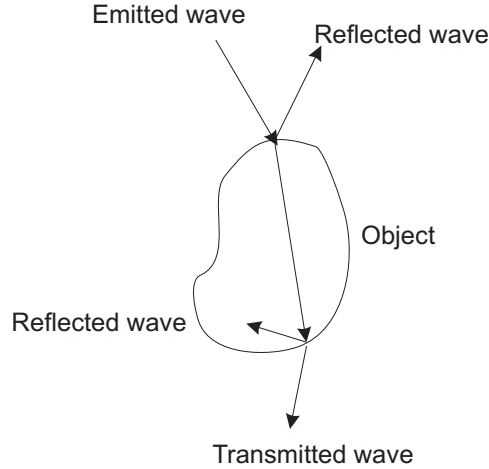


Figure 2.6: Scheme for the multiple scattering of an ultrasound wave within an object.

pulses but also of stationary noise  $n$ :

$$S(t) = \sum_{k=1}^N P_k(t) + n(t), \quad (2.8)$$

where  $N$  is the number of the ultrasound pulses. The noise  $n$  arises from different sources, e.g. environment, electronic devices, etc..

### 2.3.4 Multiple scattering

It is important to analyze the reflected pulses in USCT, because these pulses represent the positions and acoustic properties of different tissues within the breast. It is assumed that the objects are homogeneous and have a certain thickness. The ultrasound waves are partly reflected on the boundary of objects as shown in Fig. 2.6 due to a different sound impedance of the coupling medium and the object [48, 49]. Another part is refracted into the object. The deflected wave is then reflected and deflected again as it encounters the inner surface of the object. I.e. parts of the ultrasound wave are reflected back and forth within the object by the inner and outer surfaces of the object and encounter more reflection processes. This phenomena is called multiple scattering. Multiple scattering is used specially to describe the process that an ultrasound signal are reflected by more objects one by one before reaching receivers.

In order to analyze the multiple scattering in USCT, B-scans of ultrasound waves are measured. The B-scan is a 2D image comprised of a set of parallel straight lines each of which corresponds to one A-scan. These A-scans are measured with one emitter and a set of receivers on the same height in the USCT. The gray values of pixels on the B-scans represent the amplitudes of corresponding samples in A-scans. the Y-axis of B-scans represents the sequence of samples in A-scans; The X-axis displays the sequence of receiver positions for corresponding A-scans [50].

Three simple phantoms are employed to analyze the effect of multiple scattering. The first phantom is a metal rod with a diameter of 1.5 mm. The other two phantoms have the same shape as the first phantom, but with the material PVC and diameters of 4 mm and 8 mm, respectively. For the measurement these phantoms are located perpendicularly to the sensors in the center of the transducer layer. The sampling rate was 10 MHz and 100 receivers with equal distance to each other are used.

The measured B-scans are plotted in Fig. 2.7. In the B-scan of the empty vessel (only filled with water) (Fig. 2.7(a)) the line with a shape of parabola represents the transmitted pulses. The parabola shape is due to the different distances between the emitter and receiver positions. The quasi-horizontal line in Fig. 2.7(b) consists of the reflected pulses from the metal rod. Since the USCT setup is circularly symmetric and the metal rod is placed near to the center of the cylinder container, the lengths of the path from the emitter position through the metal rod to receiver position are almost identical. Thus the reflected ultrasound pulses by the metal rod construct a quasi-horizontal line.

The positions of the additional quasi-horizontal lines in Fig. 2.7(c) and Fig. 2.7(d) correspond to the reflected ultrasound pulses. Diameters of the PVC rods, the speed of ultrasound and the sampling frequency are used to calculate the position of transmitted and reflected ultrasound pulses. The length of the path that the reflected pulse propagates is the distance between the surface of PVC rod and ultrasound transducers and adding several times of the diameter of PVC rod. These additional quasi-horizontal lines show the multiple scattering in USCT.

Compared to the metal rod the PVC rods have a relative large diameter and a lower sound speed, thus the different orders of multiple

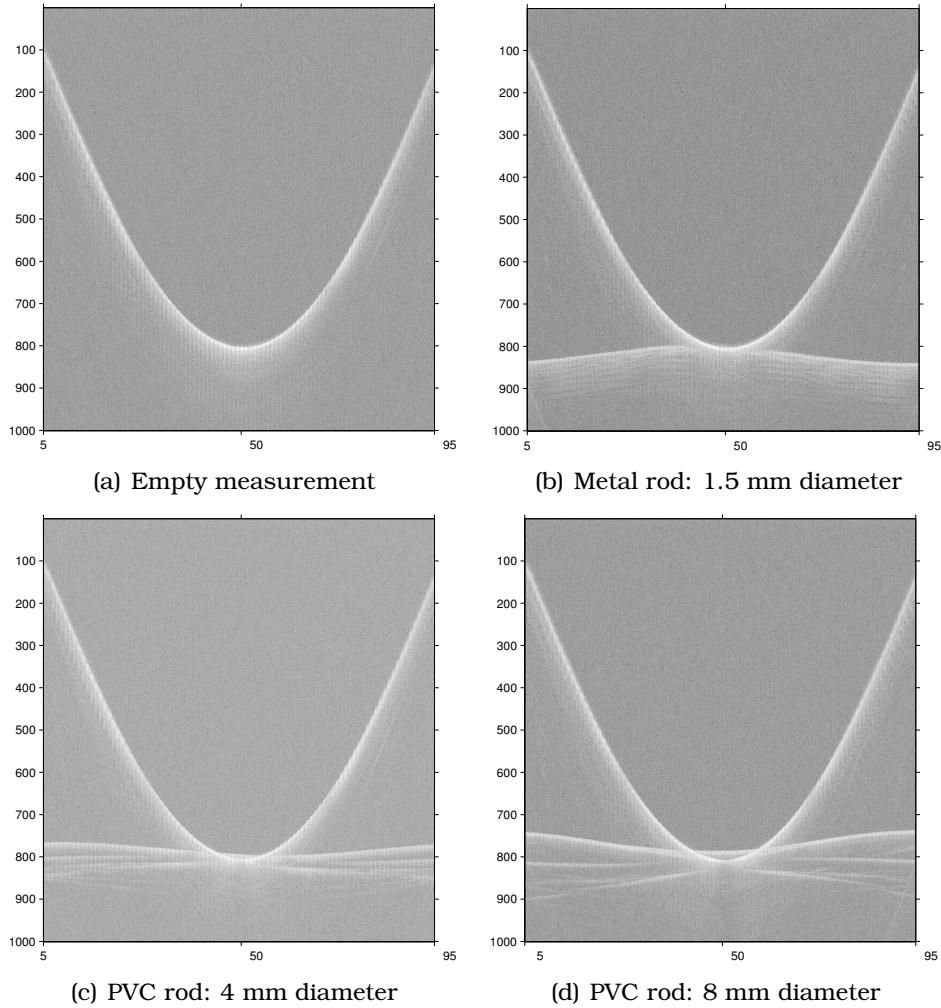


Figure 2.7: B-scans for empty measurement with transmission pulses in Fig. 2.7(a); for a metal rod with reflected pulses in Fig. 2.7(b); for PVC rods with multiple scattering in Fig. 2.7(c) and Fig. 2.7(d). X- and Y-axis stand for the receiver position and the sample number of A-scans, respectively. The gray values of pixels represent the amplitudes of corresponding samples in A-scans.

scattering are distinguished. For the metal rod the multiple scattering is not resolved in the achieved B-scan.

The multiple scattering shown in the above experiments is not considered in USCT, because the reflection factor of breast is much smaller than that of PVC and metal. The reflection factors are calculated with the ultrasound impedances, which are 1.42 MRayls and 1.63 MRayls for fat and muscle [41] as well as 11.2 MRayls and 45.7 MRayls for PVC and steel [51], respectively.

### 2.3.5 Attenuation and dispersion

Transmission in A-scans is strongly influenced by the absorption when transmitted signals propagate in the breast tissue. The scattered pulse may lose a part of energy during passing through the absorbed media. The loss of energy in the media is termed as damping [46].

The influence of damping on A-scans is modeled with attenuation and dispersion. The attenuation describes the geometrical decrease and physical attenuation of the ultrasound amplitude in the breast tissue with increasing distance to the emitter position. The dispersion designates the dependency of the propagation speed on the frequency. Both attenuation and dispersion are frequency dependent, i.e. each frequency component of ultrasound pulses has individual attenuation and dispersion factors.

The mathematical description of damping with attenuation and dispersion may be expressed with a power law dependent on frequency [52]. The system response for the damping properties of tissues  $H(f)$  is described as follows:

$$H(f) = e^{(-\alpha(f)-i\beta(f))d}, \quad (2.9)$$

where  $d$  is the distance between emitter and receiver positions,  $\alpha(f)$  is the attenuation factor which is a function of frequency.  $\beta(f)$  is the propagation factor of the media at the frequency  $f$  [53]. The function of the attenuation factor  $\alpha(f)$  is defined as:

$$\alpha(f) = \alpha_1 |f|^y, \quad (2.10)$$

where  $\alpha_1$  and  $y$  are attenuation constants and depend on attenuation property of the involved tissues [54]. The propagation factor

$\beta(f)$  is correlated to the phase variation of each frequency component [55]:

$$\beta(f) = 2\pi f/c_0 + \beta_E(f). \quad (2.11)$$

Where  $c_0$  is the sound speed at the center frequency of a pulse.  $\beta_E$  is the dispersion factor which is calculated with the KramersKronig relation [46]. If the  $y$  is an even integer or non integer,

$$\beta_E(f) = \alpha_1 \tan(\pi y/2) f |f|^{y-1}, \quad (2.12)$$

and if  $y$  is an odd integer [46]

$$\beta_E(f) = -(2/\pi)\alpha_1 f^y \ln |f|. \quad (2.13)$$

With the available attenuation constants of breast tissues and the parameters of ultrasound pulses, the damping is calculated with above functions, thus the decreasing amplitude and the shape deformation of the received ultrasound pulses are simulated for USCT [49].

The used parameter values for equation 2.12 are  $y = 1.67$ ,  $c_0 = 1500$  m/s,  $\alpha_1 = 0.81\text{dB}/(\text{cm MHz})$  taken from the experiential results in [54].

## 2.4 New lossless compressions

The state-of-the-art lossless methods were tested and achieved the low compression ratios for A-scans. New methods have to be found for increasing the compression ratio. The design of new lossless methods is based on the characteristics of A-scans.

### 2.4.1 Compression based on neighboring A-scans

The basic idea of this lossless compression is to reduce the redundancy in similar A-scans. The relationship between these A-scans are analyzed and expected to be used for a high compression ratio.

The A-scans obtained by the same emitting transducer and received by adjacent receivers in USCT are called neighboring A-scans. The neighboring A-scans have high similarity since the corresponding ultrasound waves propagate along similar paths.

The amplitude differences between neighboring A-scans are calculated and saved. Neighboring A-scans differ only by small amplitude values and the noise. If the neighboring pulses have an identical pulse shape, the amplitude differences between these neighboring pulses are given by their time difference. The basic shape of the transmission pulse in USCT is a periodic sine function of 2.3 MHz with a Gaussian envelope. In case the time difference is smaller than one sixth of the sine period, i.e.  $0.07 \mu s$ , the dynamic range of the neighboring pulses is smaller than the dynamic range of the individual original A-scan.

One emitter position S1 and two pairs of receiver positions R1-R2 and R3-R4 are used to get two couples of neighboring A-scans in Fig. 2.8. The couple of receiver positions R1-R2 stands for the case which has the largest time differences of neighboring receivers in USCT, whereas the positions R3-R4 have the smallest time difference.

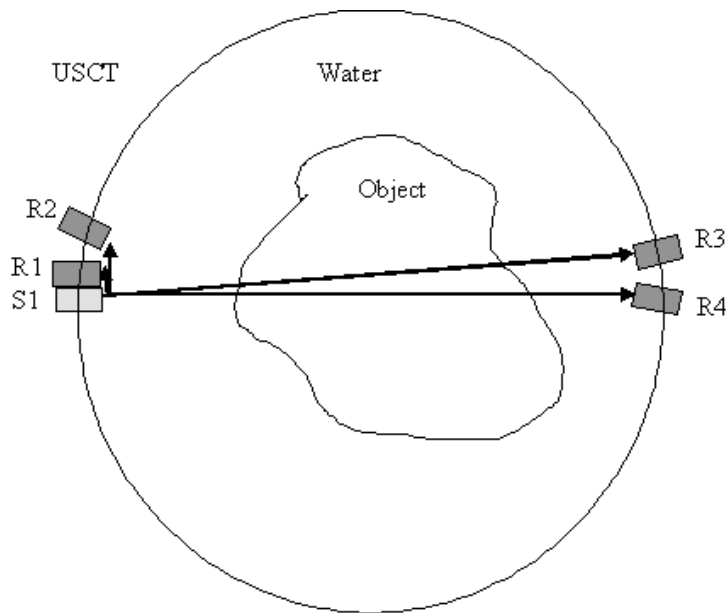


Figure 2.8: Scheme for demonstrating neighboring A-scans in the same horizontal layer of USCT. S1 stands for an emitter position; R1, R2, R3 and R4 for four extreme receiver positions.

The wave propagation paths for the receiver positions R1 and R2 are  $\|S1R1\|$  and  $\|S1R2\|$  respectively. The time difference of neighboring pulses is the length difference of the propagation paths divided by

the sound speed:  $(\|S1R1\| - \|S1R2\|) / \text{sound speed}$ . In the current version of 3D USCT setup there are 96 receivers at each receiver layer. The arc length between neighboring receivers is  $2\pi/96 \approx 0.065$  radians. The diameter of the cylindrical vessel is 183 mm. The sound speed is 1500 m/s. Thus the time difference is  $4 \mu s$ . For the receiver position R3 and R4, the lengths of the wave propagation paths  $\|S1R3\|$  and  $\|S1R4\|$  are equal, thus the time difference of the neighboring pulses is zero.

The relationship between  $\|S1R1\|$  and  $\|S1R2\|$  is very different from that between  $\|S1R3\|$  and  $\|S1R4\|$ . They are used to calculate the possible range of the time difference of neighboring pulses. Based on the above analysis the possible range is between zero and  $4 \mu s$ . This range is significantly larger than the expected time difference, i.e.  $0.07 \mu s$ . I.e. the dynamic range of the amplitude differences for neighboring A-scans may be as large as the dynamic ranges of the A-scans. Therefore the amplitude differences between neighboring A-scan are not suitable for lossless compression of USCT datasets. Additionally noise plays only a minimum role for this argument.

#### 2.4.2 Compression based on neighboring samples

In order to reduce the dynamic range of the amplitude in A-scans, the differences between neighboring samples in the same A-scan are analyzed. In case the variance of these differences is smaller than that of the A-scan, these differences are saved with fewer bits than A-scan, thus to compress the amount of the whole datasets.

The distance between two neighboring samples within the same A-scan can be represented by the phase distance of two neighboring samples on this A-scan. For simplicity a pulse with unit amplitude and the shape of the periodic sine function is employed.

The center frequency of ultrasound pulses in USCT is approx. 2.3 MHz. The sampling frequency of A-scans is 10 MHz. An antialiasing filter confines the experimental spectrum to frequencies below 4 MHz (3 dB). Assuming that the sine function is  $\sin(2\pi f)t$ , where  $f$  is center frequency,  $t$  is the time. the time difference between two neighboring samples corresponds to the phase difference  $\frac{1}{10000000(Hz)} * 2300000(Hz) * 2 * \pi = 0.46\pi$ .

The trigonometric function for the difference of two sin functions is

as follows:

$$\sin(\theta) - \sin(\phi) = 2 \cos\left(\frac{\theta + \phi}{2}\right) \sin\left(\frac{\theta - \phi}{2}\right) \quad (2.14)$$

Putting the sine function  $\sin(2\pi f)t$  and the phase difference  $0.46\pi$  into the function 2.14 thus:

$$\sin(2\pi ft) - \sin(2\pi ft - 0.46\pi) = 2 \cos(2\pi ft - 0.23\pi) \sin(0.23\pi) \quad (2.15)$$

$$\approx 1.3 \cos(2\pi ft - 0.23\pi). \quad (2.16)$$

The distance between neighboring samples can be represented by the function in 2.15 which has an amplitude of 1.3. The amplitude of the original pulse is unit, thus the differences of neighboring samples have a larger variance as the original amplitude of A-scans ( $1.3 > 1$ ). Therefore the difference of neighboring samples can not be used to reduce the dynamic range of A-scans and is unfeasible for lossless compression of USCT datasets.

### 2.4.3 Cascading bitwise run length encoding

The histograms of the sample amplitudes in A-scans show that 90% of the data has a small dynamic range. The over several A-scans averaged data has 16 bits. The values of most samples may be saved with the eight least significant bits of the 16 bits. Based on this analysis of A-scans, a bitwise lossless compression method is designed.

If successive samples of an A-scan have the same small dynamic range of amplitudes, the data amount for saving these samples may be reduced. The reason is that only a few bits are necessary for these amplitudes. In order to find these bits, each sample of A-scan is represented in a binary form. The least and the most significant bits of the samples are separated to utilize the bitwise relationship between successive samples of A-scans. The successive samples with a small dynamic range of amplitudes result in a repetition of values in some significant bits. E.g. if these amplitudes have small values, there is a repetition of 0 in the most significant bits. This repetition has a redundancy which can be compressed with run length encoding (RLE).

For example  $m$  successive samples of an A-scan are described with  $s_1; s_2; \dots; s_m$ . The  $n$ -th sample is represented with 16 bits as  $b_{n-1}, b_{n-2}, \dots, b_{n-16}$  shown in Table 2.1. The bit-stream for the above example is:  $b_{1-1}, b_{2-1}, \dots, b_{n-1}, \dots, b_{m-1}, b_{1-2}, b_{2-2}, \dots, b_{n-2}, \dots$



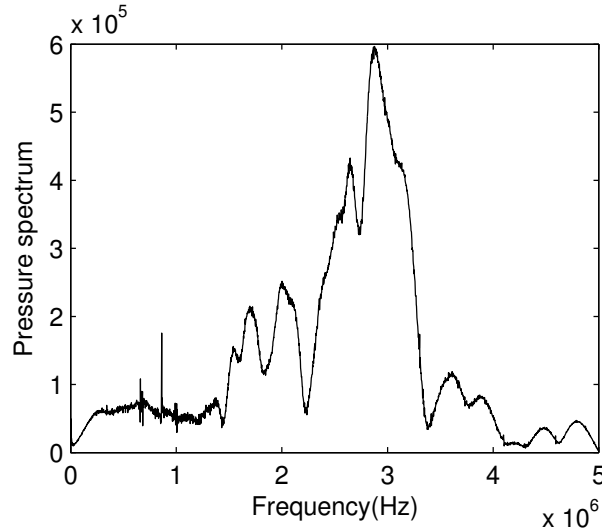


Figure 2.9: Fourier transform of an A-scan.

#### 2.4.4 Lossless compression in frequency domain

The ultrasound transducers used in USCT have a high sensitivity to signals in the frequency range between 1.5 and 4 MHz. However the data of USCT are used to keep the information of signals in the frequency range between 0 and 5 MHz. A method to reduce the amount of data is to remove the content of data in the range between 0 and 1.5 MHz as well as between 4 and 5 MHz. As an example the Fourier transform of an A-scan is shown in Fig. 2.9. The useful contents of the A-scan are in the range of 1.5 to 4 MHz.

Since useful contents of data are not lost, this method is called frequency domain based lossless compression. Based on characteristics of used ultrasound transducers in USCT and above analysis the compression ratio for the frequency domain based lossless compression is 2.

The assumption of this method is that the useful contents of data is concentrated in a certain range of frequencies. This assumption is valid due to the measured sensitivity of the transducers in USCT.

#### 2.4.5 Validation of adjacent A-scans and samples

For validation real A-scans are selected from datasets which are measured with the USCT. The selection of A-scans is based on the

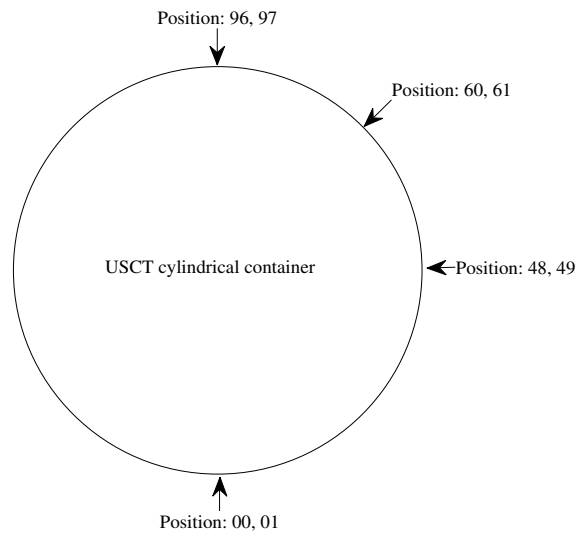


Figure 2.10: Used relative positions of emitters and receivers in the cylindrical USCT container.

position of the emitter and receiver ultrasound transducers. The selected A-scans are analyzed to understand the characteristics of USCT datasets.

For this purpose, the amplitudes of A-scans are normalized to the dynamic range of  $[-65535, +65535]$ . These A-scans are measured with one emitter and different receivers which are located on the same horizontal layer of the USCT cylindrical container. In the 3D USCT setup the indexes of emitter and receiver layers are 8 and 16, respectively. The selected neighboring A-scans are emitted at the position 00 and received at the positions 00, 01; 48, 49; 60, 61; 96, 97, as shown in Fig. 2.10.

The standard deviation of the amplitude for each selected A-scan is calculated to get the fluctuation of the original A-scan as shown in column 2 of Table 2.2. Additionally, the standard deviation of the difference between neighboring samples in the same A-scan as well as between neighboring A-scans are calculated as shown in column 3 and 4, respectively.

A-scan	Standard Deviation (Std) of Signal	Std of neighbouring samples	Std of neighbouring A-scan
A00	3588	5410	2718
A01	3360	5050	
A48	172	137	205
A49	155	155	
A60	170	140	185
A61	138	109	
A96	822	1080	363
A97	748	1040	

Table 2.2: Difference between neighbouring A-scans as well as between samples in one A-scan by comparing their standard deviations with that of measured A-scans.

The standard deviations of the differences between neighboring A-scans or samples in the same A-scan are not significant smaller than that of the original A-scans. These results are consistent with the theoretical analysis in section 2.4.1 and 2.4.2.

#### 2.4.6 Validation of bitwise run length encoding

Further experiments are carried out to evaluate the performance of the new lossless compression method introduced in section 2.4.3. The selected A-scans in section 2.4.5 are used in this experiment.

The entropy of original A-scans is calculated to represent the information in the A-scans. The theoretical optimal compression ratios are based on this entropy, see 2.1.2. The commonly used compression software WinZip Version 14.0 uses the state-of-the-art lossless compression methods, e.g. LZW [56]. WinZip has a better performance than standard RLE method and it is used in this work to be compared with the cascading bitwise RLE. The original A-scans are compressed with WinZip V14.0. The achieved compression ratios are compared in Table 2.3 to demonstrate the performance of the cascading bitwise RLE.

The compression ratios by cascading bitwise RLE yield 80 % of the theoretical optimal compression ratios and are better than the compression ratios achieved with WinZip V14.0.

In Table 2.4 are the optimal lengths of the words for saving the

A-scan name	Information entropy of original A-scan	Theoretical optimal compression ratio	Compression ratio with cascading bitwise RLE	WinZip V14.0
A00	8.81	1.82	1.53	1.31
A01	8.90	1.80	1.52	1.31
A48	9.16	1.75	1.60	1.30
A49	8.91	1.80	1.66	1.32
A60	9.19	1.74	1.60	1.30
A61	8.94	1.79	1.66	1.33
A96	9.37	1.71	1.53	1.28
A97	9.07	1.76	1.60	1.31

Table 2.3: Comparison of the theoretical optimal compression ratios of real A-scans and the obtained compression ratios with cascading bitwise RLE and WinZip.

run length of the componential bit-stream-blocks in this experiment. The sequence of the componential bit-stream-blocks is from the most to the least significant bits.

In order to evaluate the correctness of the implemented method, the compressed A-scans are decompressed and compared to the original A-scans. Since the compression method is lossless, the decompressed A-scans were identical to the original A-scans as expected.

## 2.5 Lossy compression methods

To overcome the low compression ratios of lossless compression, lossy compressions are considered in the following. Irrelevant content in the datasets may be removed by lossy compression; therefore it is important to separate the irrelevant and relevant parts in the datasets.

The preprocessing of lossy compression is to separate the information of ultrasound pulses from other information of A-scans. After that the separated information is encoded in a compact form by using a lossless compression method, e.g. RLE [57]. In order to reconstruct images with the original data format of A-scans, the compressed datasets have to be decompressed with the inverse process, i.e. the decoding and the post processing as shown in Fig 2.11.

Sequence of componential bit-stream-blocks	A00	A01	A48	A49	A60	A61	A96	A97
1	10	10	12	12	12	12	12	12
2	10	10	12	12	12	12	12	12
3	10	10	12	12	12	12	12	12
4	9	9	12	12	12	12	10	10
5	9	9	12	12	12	12	10	10
6	8	9	12	10	12	12	10	10
7	8	8	10	10	10	12	8	10
8	6	5	4	6	4	5	3	5
9	1	1	1	1	1	1	1	1
10	1	1	1	1	1	1	1	1
11	1	1	1	1	1	1	1	1
12	1	1	1	1	1	1	1	1
13	1	1	1	1	1	1	1	1
14	1	1	1	1	1	1	1	1
15	1	1	1	1	1	1	1	1
16	1	1	1	1	1	1	1	1

Table 2.4: Optimal word length for each componential bit-stream-block in the A-scan which is compressed with the cascading bitwise RLE. The sequence of the componential bit-stream-blocks is from the most to the least significant bits.

Based on the characteristics of preprocessing, the selected lossy compression methods for USCT are classified into three domains, i.e. time, frequency and time-frequency domains. In time domain A-scans are compressed by threshold, peak detection and spiking deconvolution methods. The ultrasound pulses are separated from noise without transform. The discrete cosine transform is used to analyze A-scans in frequency domain. The methods used to transform A-scans into both time and frequency domains are discrete wavelet transform, multi-fractal transform and continuous wavelet transform which can be optimized by selection of suitable mother wavelets. The performances of the implemented compression methods are compared.

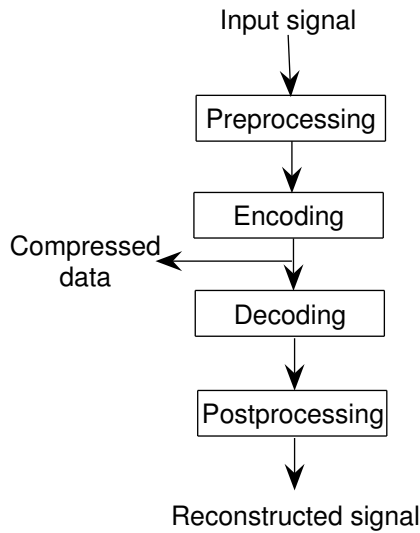


Figure 2.11: Compression algorithm.

### 2.5.1 Time domain based methods

The variation of the amplitudes with time in A-scans is considered to get the ultrasound pulses. The values of the amplitude for a single sample as well as the relationship between neighboring samples in A-scans are used to select the compression parameters.

#### 2.5.1.1 Threshold

The simplest method of data compression is rejecting all data below a threshold value and set these values to zero [58]. The basic idea is that ultrasound pulses have higher amplitudes than the noise.

The achieved compression ratio for the A-scan is decided by the threshold value. If the amplitudes of ultrasound pulses are not significantly larger than the noise, the choice of a suitable threshold value becomes difficult.

Different threshold values are tested to achieve an optimal compression ratio for USCT datasets, since the optimal threshold value is

unknown. The input A-scans are normalized to get a unified threshold value for different A-scans in a dataset. The optimal threshold value  $k \cdot \sigma$  is searched step by step with a step length  $\sigma$ , where  $k$  stands for the number of steps. The preprocessed datasets are then encoded by RLE to get compressed datasets at different compression ratios. The threshold value relative to the maximum amplitude of each A-scan is used instead of the signal to noise ratio, since the signal to noise ratio for each A-scan is difficult to be achieved in USCT.

### **2.5.1.2 IK peak detection**

The standard IK peak detection method (IKstd) was developed for pipeline inspection with ultrasound signals in industry [59]. A given threshold value is used to remove the influence of the noise. Then the local neighborhood of sample amplitudes is considered [60].

The properties of ultrasound pulses are strongly influenced by the use of coded excitation, whose envelope has a similar shape as a Gauss function. The position of the peak sample in the ultrasound pulse is related to the neighboring samples which have lower amplitude values.

The  $I$  and  $K$  values are used to represent the number of used samples before and after the peak sample within an ultrasound pulse. If the values of  $I$  and  $K$  are too small, noise might be selected. In case the amplitude of a sample is larger than the threshold for  $I$  samples before and  $K$  samples after the peak, the time position and the amplitude of this sample is saved. Otherwise the amplitude of this sample is saved as zero. The  $I$  and  $K$  values in this work are adapted to the shape of the implemented ultrasound pulses. A pulse length of 3 or 4 samples was chosen. In this condition,  $I = 1$  and  $K = 2$  give the best detection and reconstruction results. If two pulses are very near to each other, the pulse with the lower amplitude might be lost for large values of  $I$  and  $K$ .

The IKstd is implemented in hardware easily and achieves a high computation speed due to its low computational complexity. If the amplitudes of reflected pulses are lower than the noise level, these pulses can not be detected by IKstd. Due to the unknown properties of noise in USCT, the performance of IKstd has to be validated with different threshold values at experimental datasets.

### **2.5.1.3 Modified IK algorithm**

The modified IK algorithm (IK) is a newly designed lossy compression method in this work. The motivation is to increase the performance of the standard IK peak detection method which uses the fixed values of  $I$  and  $K$ . The optimal  $I$  and  $K$  values should be selected based on the relationship between the peak and the neighboring samples which vary due to the pulse deformation.

In the IK method the deformation of the ultrasound pulses is considered. The values of  $I$  and  $K$  in a range between one sample and the width of the deformed pulse are tested. The compressed datasets are reconstructed to images. The optimal values of  $I$  and  $K$  are selected based on the quality of these reconstructed images.

The performance of IK is evaluated by comparing with the other compression methods used in this work. The images are reconstructed with the datasets which are compressed with IK and the other compression methods. The quality of these reconstructed images is scored to compare the different compression methods.

### **2.5.1.4 Spiking deconvolution**

Ultrasound pulses might be located very near to each other in an A-scan. These pulses overlap partly and makes the detection of the ultrasound pulses by comparison to sample amplitudes difficult. The deconvolution method is implemented to extract each single pulse by using the information of coded excitation.

The basic idea of spiking deconvolution (DCV) is to convolute the A-scan with a deconvolution filter. In the convoluted A-scan the ultrasound pulse is replaced by the time stamp plus amplitude of this pulse. The deconvolution filter is achieved by calculating the inverse of the coded excitation function [27].

After the convolution process with a fixed threshold the samples with larger amplitude than others are selected. The selected samples are saved to represent the information of ultrasound pulses, thus a reduced amount of data is saved.

It is assumed in DCV that the ultrasound pulses in an A-scan have an identical or similar pulse shape as the coded excitation function. The DCV has the advantages to separate the ultrasound pulses which are located very near to each other. If the pulses have a deformation due to the absorption of breast tissues, the performance of this method is reduced. In the experiments with USCT datasets, the threshold values are adapted for an optimal compression performance of DCV.

## **2.5.2 Frequency domain based methods**

In order to utilize the properties of A-scans in frequency domain for data compression, A-scans are transformed into frequency domain or analyzed by discrete cosine transform. First the range from 0MHz to 1.5MHz and from 4MHz to 5 MHz were neglected, since the transducer has no sensitivity in these ranges. In the range from 1.5MHz to 4MHz there are various patterns depending on the type of object and the A-scan, therefore there is no further handle for compression in the frequency range. We do not expect any large compression ratios beyond what is given by frequency cuts(see section 2.4.4). The A-scans in the frequency domain are quantized by a threshold and are transformed back into the time domain.

In frequency domain the information of ultrasound pulses is expected to be represented with a higher magnitude than other informations. Thus the other informations are removed with a threshold to achieve a high compression ratio.

### **2.5.2.1 Discrete cosine transform**

The discrete cosine transform based compression method (DCT) using the real part of the Fourier transform has the advantage of representing the information in a compact form. Due to the even symmetry of the cosine function the continuity on the boundary of the original signal is remained by DCT [61], the rate of convergence of frequency spectrum increases, thus the signal can be represented in the frequency domain in a more compacter form [62].

The performance of DCT is influenced by the frequency distribution of ultrasound pulses in A-scan. The pulse deformation results in reduced values of coefficients which cannot be kept during data

compression. Therefore some useful information of the deformed pulses may be lost after data compression. E.g. the information about the time position of pulses cannot be detected precisely after the decompression.

### 2.5.3 Time and frequency domain based methods

#### 2.5.3.1 Discrete wavelet transform

The discrete wavelet transform is used for compression of A-scans due to its time-frequency representation of information in datasets [24]. A-scans are represented with wavelet coefficients after pre-processing using discrete wavelet transform [63]. The basic idea of using discrete wavelet transform based compression (DWT) for A-scans is their shape-similarity to the pulse shape of coded excitation. By this fact it can be expected, that the number of wavelet-coefficients may be small against the number of samples. The wavelet-coefficients are saved instead of samples of A-scans and the resulting compression may be high.

A-scans are convoluted with a family of basis functions, i.e. mother and father wavelets, to achieve the wavelet coefficients. The father wavelet also called scaling function can be derived from the mother wavelet. The mother and the father wavelets are orthogonal functions. The time information of the ultrasound pulses corresponds to the time position of the convoluted basis functions. In order to get the frequency information, the basis functions are convoluted in different scales with the A-scans. The original A-scans can be reconstructed perfectly with the uncompressed wavelet coefficients using the inverse discrete wavelet transform [25, 26].

It is not easy to find a basis function that can be used as the mother wavelet. The simplest mother wavelet is Haar, whose definition is shown with following function:

$$W_{\text{Haar}}(x) = \begin{cases} 1 & 0 \leq x < 1/2, \\ -1 & 1/2 < x \leq 1, \\ 0 & \text{otherwise.} \end{cases}$$

The standard mother wavelets [64] for DWT are collected to construct the wavelet filter bank. The contents of the filter bank are the coefficients of mother and father wavelets. The selection of the

standard mother wavelets influences the performances of the discrete wavelet transform in data compression.

With DWT the wavelet coefficients are achieved with the selected mother wavelets at a large range of scales. The achieved wavelet coefficients are quantized and saved as compressed datasets for USCT. The performance of different standard mother wavelets are tested experimentally.

### **2.5.3.2 Multi-fractal analysis**

A-scans are considered to have the fractal features, since the noise in ultrasound signal may show singular behavior. I.e. some points of signal in time cannot be approximated with a Taylor series using a finite number of terms [65]. The fractals in A-scans are analyzed with the DWT method, since the properties of fractals are related to the wavelet coefficients [66]. The method introduced in [67] uses the multifractal analysis by processing wavelet coefficients to reduce noise in signals. This method (called MultiFractal in this work) is used to reduce the noise in A-scans and increase the performance of data compression in USCT.

The main process of the MultiFractal method used in this work is as follows: In the first step the wavelet coefficients are registered with DWT to represent the A-scans. Then these wavelet coefficients are damped with factors which are power law related to the corresponding frequencies of the wavelet coefficients. High frequency components are reduced strongly. Finally the processed wavelet coefficients are quantized and compressed.

The wavelet coefficients corresponding to the high frequencies are considered to have more information about noise. Thus these wavelet coefficients are decreased more strongly.

The damping factor can be selected by users and has a large value for the original dataset with a high noise level. The performance of MultiFractal with the selected damping factor has to be evaluated with USCT datasets in experiments due to the unknown characteristics of noise.

### 2.5.3.3 Continuous wavelet transform

The continuous wavelet (CWT) is used mostly for research of signal properties instead of implementation of data compression. The local characteristics of signals are represented with the achieved coefficients. In this work CWT is combined with a statistic peak detection method [68] and used for the compression of USCT datasets (WavePDT). The name WavePDT method is an abbreviation of the continuous wavelet based peak detection method.

The wavelet coefficients  $F_w$  for a function  $f(x)$  with a mother wavelet  $W$  are calculated as follows:

$$F_w(a, b) = \frac{1}{\sqrt{a}} \int_{-\infty}^{\infty} f(x) W^* \left( \frac{t-b}{a} \right) dx$$

where  $*$  stands for the operation of complex conjugate.  $a$  and  $b$  are scale and translational parameters respectively.

In the WavePDT method the A-scans are represented with the wavelet coefficients by using the CWT. The mother wavelet used in CWT is the Morlet mother wavelet defined in [69]. Wavelet coefficients of real experimental signals are measured to construct a decision tree. This decision tree is based on the values of wavelet coefficients of the available ultrasound pulse. The wavelet coefficients of A-scans, which corresponds to an ultrasound pulse in decision tree, are selected. The selected wavelet coefficients represent the information of the ultrasound pulses in A-scans.

The information included in the selected wavelet coefficients is represented by the time-of-arrival, center frequency, phase, bandwidth and amplitude of detected ultrasound pulses [69]. These parameters are saved as the compressed data for A-scans.

CWT in WavePDT method uses mother wavelets which are designed under different conditions as for the discrete wavelet transform. The generally used mother wavelets for CWT are Morlet, Meyer and Mexican Hat [64]. The statistic peak detection method in WavePDT method uses an iteration process, until every ultrasound pulse in A-scans is detected. Details can be found in [68].

The WavePDT method uses the advantages of CWT and a peak detection method with a decision tree to represent the information in A-scans. The number of wavelet coefficients is smaller than the number of samples to achieve a high compression ratio. However

the iteration process results in a high computational complexity for implementation of these compression methods.

#### **2.5.4 Comparison of different compression methods**

A brief comparison of the compression methods used in this work ordered by their compression process is given in Table 2.5. The encoding method, e.g. RLE, is implemented for Threshold, DCV, DCT, DWT and MultiFractal method, since there are successively zeros after quantization with a threshold.

Based on preprocessing the used compression methods are classified into transform necessary or unnecessary methods. The transform based compression methods have the advantage to represent the information of reflected pulses with only a small amount of data. In order to get the original data format, the inverse transform has to be implemented during the decompression methods. The transform and inverse transform processes increase the computational complexity of compression methods. Some compression methods as threshold, IKstd and IK do not have any complete inverse transform.

Based on the selection of compression parameters the used compression methods are classified into pulse shape dependent or independent compression methods. For the pulse shape dependent methods the information of coded excitation is considered during the selection of parameters. Pulse shape based compression is based on the assumption that the measured ultrasound pulses in A-scans are similar to the emitted pulse of coded excitation. In case that the pulses are strongly deformed, the performance of pulse shape based compression decreases significantly.

Threshold and DCT methods are the pulse shape independent compression methods, because the pulse shape of coded excitation is not considered during the compression process. The DWT, MultiFractal and WavePDT by selection of the mother wavelets as well as the DCV by design of the deconvolution filter are based on the shape of coded excitation. For IK and IKstd the  $I$  and  $K$  values are based on not only the shape but also the sample frequency of coded excitation.

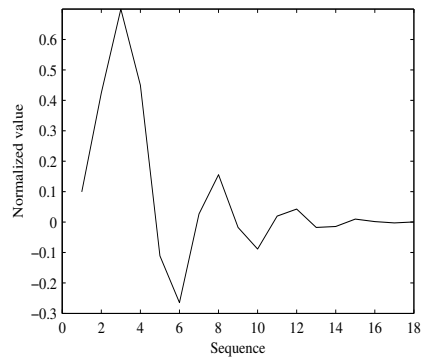
The DWT and MultiFractal compression methods use the standard

Compression methods	RLE necessary (Yes/No)	Transform necessary (Yes/No)	Pulse shape dependent (Yes/No)
Threshold	Yes	No	No
IKstd	No	No	Yes
IK	No	No	Yes
DCV	Yes	Yes	Yes
DCT	Yes	Yes	No
DWT	Yes	Yes	Yes
MultiFractal	Yes	Yes	Yes
WavePDT	No	Yes	Yes

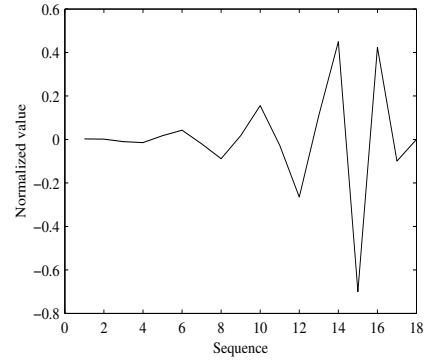
Table 2.5: Comparison of state-of-the-art compression methods.

Haar mother wavelet, the simplest standard mother wavelet. Other used standard mother wavelets include Symmlet, Daubechies, Beylkin, Coiflet and Vaidyanathan mother wavelets.

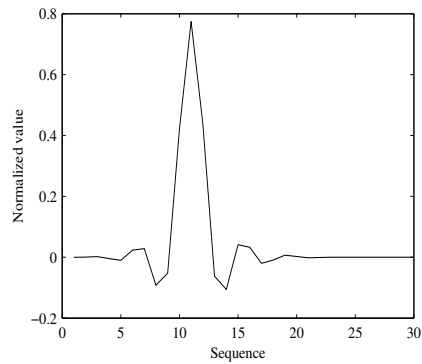
The standard mother wavelets are implemented and compared for USCT datasets to achieve an optimal performance of data compression [70]. The pulse shape of these mother wavelets are shown in Fig. 2.12, Fig. 2.13 and Fig. 2.14.



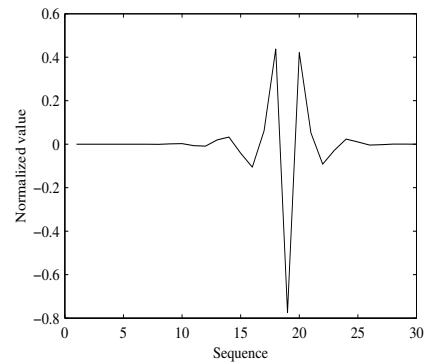
(a)



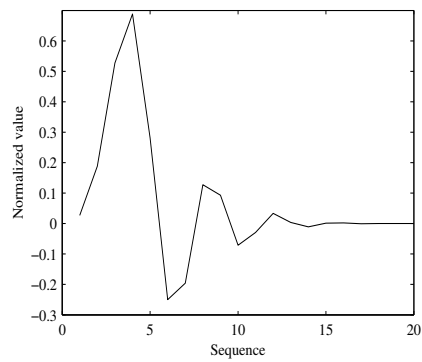
(b)



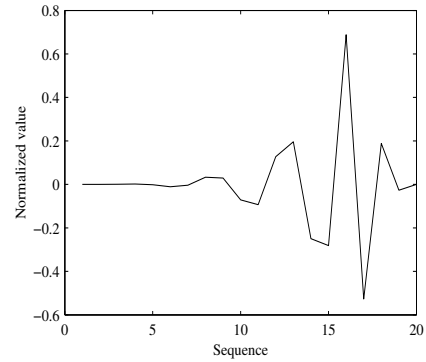
(c)



(d)

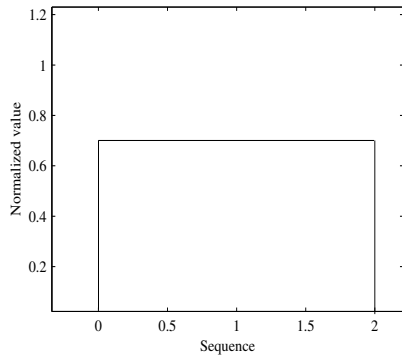


(e)

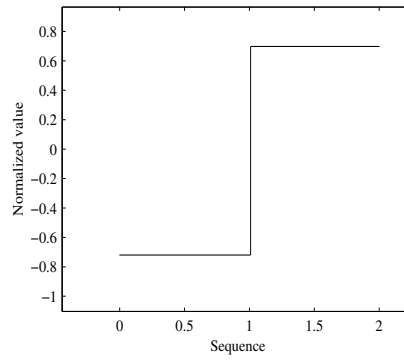


(f)

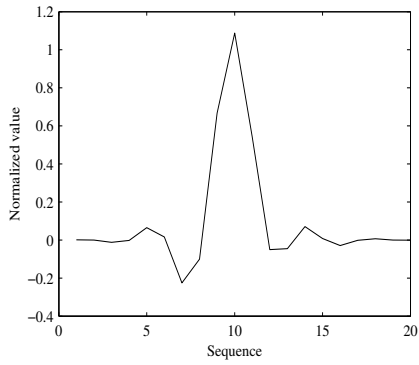
Figure 2.12: Tested wavelets: Beylkin (a, b), Coiflet 5-tap (c, d), Daubechies 20-tap (e, f) corresponding father (a, c, e) and mother (b, d, f) wavelet.



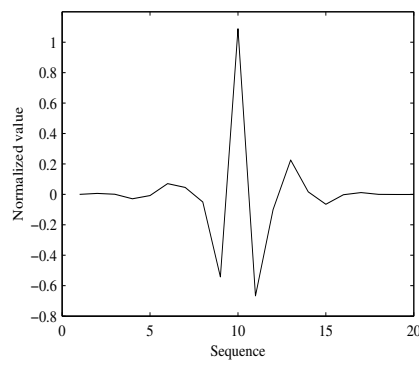
(a)



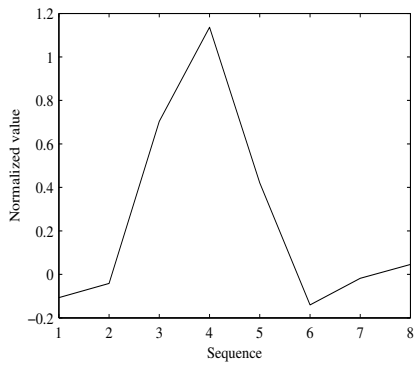
(b)



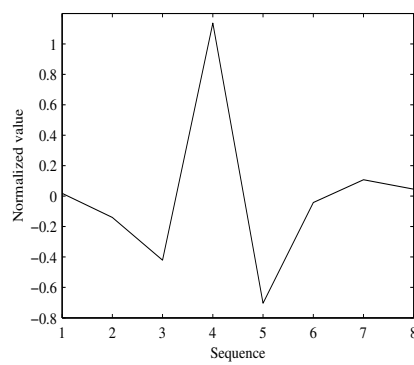
(c)



(d)



(e)



(f)

Figure 2.13: Tested wavelets: Haar (a, b), Symmlet 4-tap (c, d), Symmlet 10-tap (e, f) corresponding father (a, c, e) and mother (b, d, f) wavelet.

The mother wavelets are convoluted with the A-scans for detection of ultrasound pulses, therefore the similarity between the mother wavelets and the pulse shapes influences the performance of the discrete wavelet transform. The standard mother wavelets and their similarity to coded excitation in USCT are listed in table 2.6 [10].

The flexible selection of the standard mother wavelets makes it possible to optimize the performance of data compression with DWT. If the ultrasound pulses have an identical shape as the mother wavelet, the corresponding wavelet coefficients have large values. The mother wavelet with similar pulse shape as coded excitation is expected to have a high performance of data compression. The mother wavelet Symmlet 10-tap is used in experiments for USCT datasets, since it has a similar shape as the coded excitation.

## **2.6 Properties of adapted lossy compression**

### **2.6.1 Computational complexity**

#### **2.6.1.1 Theoretical analysis**

The computing time of the data compression depends not only on the amount of the raw data but also on the computational complexity of the compression methods. In case that the speed of the data compression process is slower than that of the data acquisition process, the received data have to be buffered. In order to reduce the time costs, the computational complexity of the data compression process is discussed.

The computing time of different compression methods are compared for the same dataset. This computing time includes the time for compression and decompression. The computational complexities of compression and decompression depends on the used computer and characteristics of compression methods.

The computational complexity of implemented compression methods is shown in Table 2.7. The number of necessary arithmetic operations is calculated as a function of data length. ' $O$ ' denotes the order of the function and ' $N$ ' is the length of A-scans in USCT, i.e. the sample number.

Main operations include multiplying, adding and comparison oper-

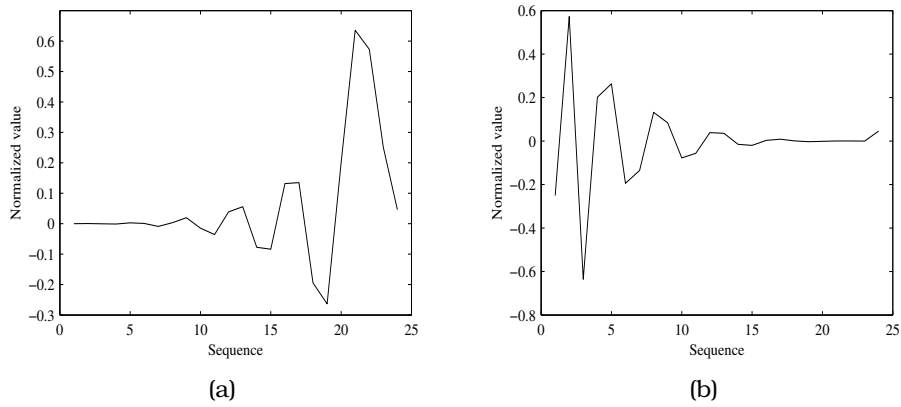


Figure 2.14: Tested wavelets: Vaidyanathan corresponding father (a) and mother (b) wavelet.

Name	Number of coefficient	Similarity to coded excitation
Haar	2	Low
Symmlet 4-tap	8	Low
Symmlet 10-tap	20	High
Daubechies 20-tap	20	High
Coiflet 5-tap	30	High
Beylkin	18	Middle
Vaidyanathan	24	Middle

Table 2.6: Comparison of standard mother wavelets.

ations that use most of the computing time. IKstd method needs  $3 \times N$  comparison operations. The number of operation depends on the selected  $I = 1$  and  $K = 2$  values. The Length of the deconvolution filter  $FL$  in the DCV compression method influences the number of needed operations. The computation complexity of DCV is a function of order  $N$ .

The operation of DCT corresponds to the discrete Fourier transform (DFT). For DFT each frequency component involves  $N$  operations. To compute all  $N$  values of the DFT requires  $N^2$  operations. The fast Fourier transform utilizing the symmetry and periodicity properties of the DFT, the number of operations is reduced to  $N \log_2 N$  [71]. Compared to other compression methods in Table 2.5 DCT does not consider the shape of coded excitation. Therefore the computational complexity of DCT will be not discussed further.

For DWT  $2^n$  operations are necessary for convolution of the A-scan with the smallest scale of the mother wavelet, if the length of an A-scan is  $N = 2^n$ . For increasing scales, the number of operations are  $2^{(n-1)}, 2^{(n-2)}, \dots, 2^1$ . Thus, the total number of operations is  $\sum_{i=1}^{n-1} 2^i = \sum_{i=0}^{n-1} 2^i - 1 = \frac{1-2^n}{1-2} - 1 = 2^n - 2 = N - 2$ . Thus the DWT of  $N$  data items is performed with  $N - 2$  operations and its complexity is  $O(N)$ [24].

The computational complexity of the WavePDT method is based on the CWT. Each wavelet coefficient needs  $N$  operations for the convolution process. For  $N$  wavelet coefficients the operation number of CWT is  $N^2$ . Besides the operations for CWT, the iteration process in WavePDT method spends lots of operations for an optimal selection of wavelet coefficients. The computing time increases significantly due to this iteration process.

### 2.6.1.2 Computing time

The capacity of the computer used in this work is Pentium(R) 4 CPU 3.2GHz with 2.0 GB RAM and 1024 KBytes cache. The compression methods are designed and implemented with the signal processing toolboxes of Matlab software. The function to measure the computing time is the PROFILE function in Matlab.

The computing time for each compression method shown in Table 2.7 means the time range from loading an A-scan to saving the

Method	Main operation (time)	Computational complexity	Computing time (second/A-Scan)
IKstd	$3N$	$O(N)$	0.08
IK	$(i + k) * N$	$O(N)$	0.08
DCV	$N * FL$	$O(N)$	$\approx 0$
DWT	$N - 2$	$O(N)$	0.016
WavePDT	$> N^2$	$> O(N^2)$	4.500
MultiFractal	$2(N + 1) + N$	$O(N)$	0.016
Threshold	$N$	$O(N)$	$\approx 0$

Table 2.7: Computational complexity of compression methods. (FL: Length of the deconvolution filter.)

compressed A-scan into the memory with available compression parameters. For this compression a simulated A-scan with the length  $N = 1355$  samples is used. Each sample is saved with two bytes. The computing time is calculated with one A-scan because it does not depend on the content of an A-scan.

The computing speed for IKstd is slower than expected due to the low performance of the software implementation. The used values for  $I$  and  $K$  in IKstd method are 1 and 2, respectively. The computing time of the IK method is slightly different from IKstd due to the changed  $I$  and  $K$  values.

The theoretical analysis  $O(\log N) < O(N) < O(N^2)$  and the experimental results show that DWT and DCV have lower computational complexity than WavePDT. DWT uses the mother wavelet Symmlet 20. It is assumed that for these methods the optimal implementation was chosen.

## **2.6.2 Denoising ability of compression methods**

The denoising ability of the selected compression methods was tested. To get an unambiguous quality check, simulated noise for the test of the denoising ability of the compression methods is used. These noisy datasets are compressed with different compression methods. The quality of the compression methods is compared.

### **2.6.2.1 Simulation of noisy datasets**

The simulated noisy datasets are made to be similar to experimental datasets in USCT after preprocessing (see section 2.2.2). The noise is simulated by a distribution of white noise with a given amplitude. This noise is added to the simulated datasets of USCT to create the noisy datasets.

The noisy datasets are filtered before the compression process. The frequency response of the used 8th order low- and 4th order high pass Bessel filter is plotted in fig 2.15 and fig 2.16 . The filter has similar properties as the analog anti-aliasing filter used in USCT.

A Bessel filter has almost constant group delay across the entire band-pass [72], thus can preserve the shape of the filtered pulses. The cut-off frequencies of the low- and high pass Bessel filters are 1.4 MHz and 3.6 MHz, respectively.

### **2.6.2.2 Compression of noisy datasets**

The filtered noisy datasets are compressed with the selected compression methods for USCT. The compression ratios vary corresponding to the selected quantization parameters. At low compression ratios, only the noise is expected to be reduced during the data compression. But the important information of ultrasound pulses in A-scans may be removed together with the noise if unsuitable compression parameters are selected.

To evaluate the denoising ability of implemented compression methods, the images are reconstructed with these compressed datasets. The quality of these reconstructed images is compared.

The optimal compression ratio which depends on a threshold value,

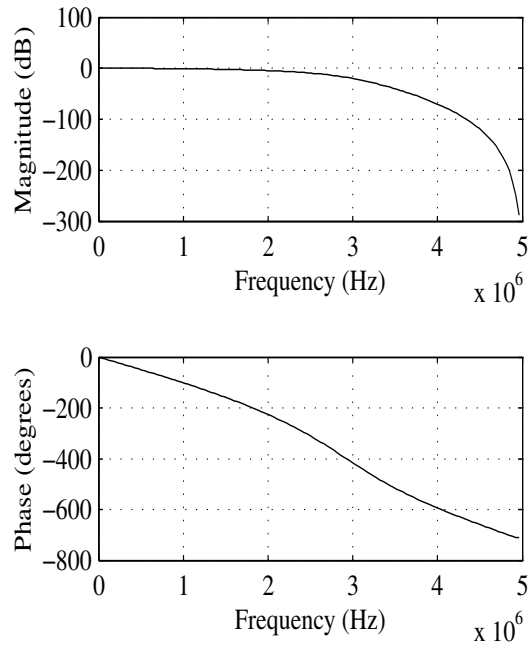


Figure 2.15: Frequency response of designed 8th order Bessel low pass filter.

is also influenced by the noise grade in the datasets. In order to find the optimal threshold value for each dataset, the quality of the compressed datasets for different compression ratios are compared.

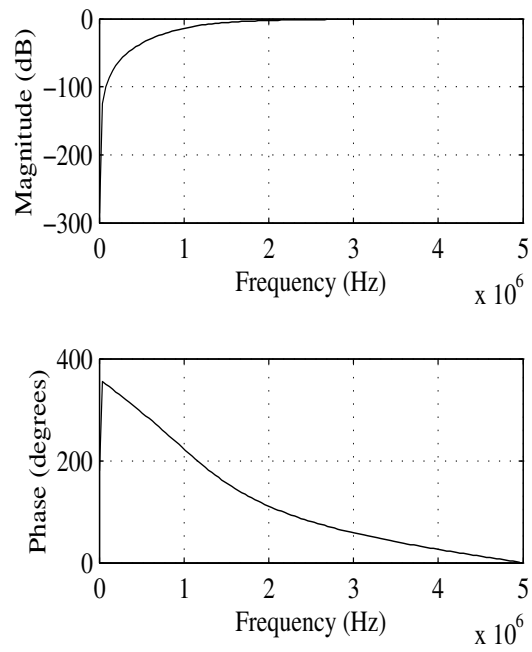


Figure 2.16: Frequency response of designed 4th order Bessel high pass filter.

## Chapter 3

# Evaluation of signal compression methods

### 3.1 Introduction

Although hundreds of data compression methods exist, an unsolved problem is how to measure the effect of these compression methods on the quality of datasets for the end user [73], e.g. radiologists. A reasonable scoring system has to be developed to select a suitable compression method for USCT.

Parts of the contents in the A-scans are removed during the lossy compression process. I.e. the decompressed A-scans are not identical to the original signals. Contents in the removed parts of A-scans are lost. Furthermore, the contents in the remaining parts of A-scans may be changed during compression. In either case the quality of A-scans may be changed by the variation of useful or useless contents.

The first challenge for evaluation of compressed A-scans is to find a reference. In order to construct a reasonable reference for A-scans, it is important to understand the useful contents in A-scans. As discussed in section 2.3, the ultrasound pulses include the information for reconstructed objects in USCT images. The ultrasound pulses include not only the information about the amplitude and time of arrival (TOA) of ultrasound pulses which is relevant for image reconstruction, but also the information of the pulse shape, the pulse deformation, multiple scattering, etc. which is expected to be partly removed during data compression. Due to the complex process of acoustic propagation in breast tissue, these contents of

ultrasound pulses cannot be distinguished clearly from each other [49]. The inseparable information in ultrasound pulses of A-scans makes it hard to construct a reference based on the useful content of original A-scans. In addition, the noise in original A-scans is irrelevant for imaged objects and make the job of separation of useful contents more complicated. Therefore, it is hard to construct a reference on the useful content of original image.

The second challenge is to evaluate the relative variations of useful to useless contents in compressed A-scans. The optimal compression method maintains useful contents and decreases irrelevances of ultrasound signals. If the useful contents are removed during lossy compression, the images reconstructed with the compressed signals have a decreased quality. Otherwise if the irrelevances are reduced by a suitable compression method, the quality of an image increases and might be of even higher image quality than the image reconstructed with original signals. Furthermore the image quality will improve with increasing compression ratio. The image quality of compressed datasets varies with an unexpected tendency, when the useful and useless contents are reduced by compression simultaneously. The unknown relative variation of useful to useless contents makes it difficult to evaluate the compressed A-scans.

The third challenge comes from the large amount of A-scans in USCT datasets. It is very time-consuming to evaluate the 3.5 Million compressed A-scans within one dataset.

Based on above discussion the A-scan is insufficient to be used directly in the evaluation methodology for evaluation of the compression artifacts in A-scans which may be only identified in the reconstructed image. Since USCT is an imaging system, an image quality based evaluation method is proposed. I.e. the quality of reconstructed images which can be used to represent the compression artifacts in A-scans, is estimated.

### **3.1.1 An image quality based evaluation method**

**Hypotheses** The design of an image quality based evaluation system for compressed signals in USCT is based on following hypotheses:

1. There is redundancy in A-scans, therefore the lossy compression methods may be used. Removing these irrelevances in A-scans with lossy data compression methods may improve

the quality of reconstructed image.

2. The images instead of A-scans are interesting for USCT projects. The content of a whole USCT dataset is transferred to the final user only in the form of the reconstructed images. The evaluation of compressed datasets is equivalent to evaluate the quality of the reconstructed images.
3. A sufficient stage of preprocessing is necessary for a good reconstruction. Especially a filter on the data between 1.5 to 4 MHz and a shift of the data in the Fourier space to 0 to 2.5 MHz gives alone a reduction of data by a factor 2 and reduces noise and artifacts.

**Assumptions** According to the characteristics of an USCT system, following assumptions are necessary for the design of an image quality based evaluation method.

1. The contours instead of the whole areas of the imaged tissues are represented in images. The shape, position and contrast of imaged tissues are shown because this work concentrates on tomography of scattering waves. Transmission pulses of A-scans are also kept in compressed A-scans to achieve a velocity map of ultrasound for optimization of reconstructed images.
2. The reconstruction algorithm and parameters are fixed for the images of compressed datasets using different methods and at different compression ratios. The reason is that the quality of the reconstructed image is influenced not only by the contents of A-scans but also by the reconstruction method. During the course of this work for data compression the reconstruction method has very much improved, but to have comparable compression quality it was necessary to fix the reconstruction method in the early stage of this work.
3. The information about the emitted ultrasound pulses, i.e. coded excitation, is available.

### **3.1.2 Influences of signal compression on reconstructed images**

The quality of reconstructed images with compressed A-scans is influenced by the compression in A-scans. This influence has to

be analyzed to understand the proposed evaluation system in this work.

**Terminologies** Some terminologies for the relationship between reconstructed images and compressed A-scans are often used in the following chapter of this thesis, therefore they have to be explained first. The figure 3.1 shows the terminologies: original image, image of compressed dataset, ideal reconstructed image and ideal reference, and their relationship.

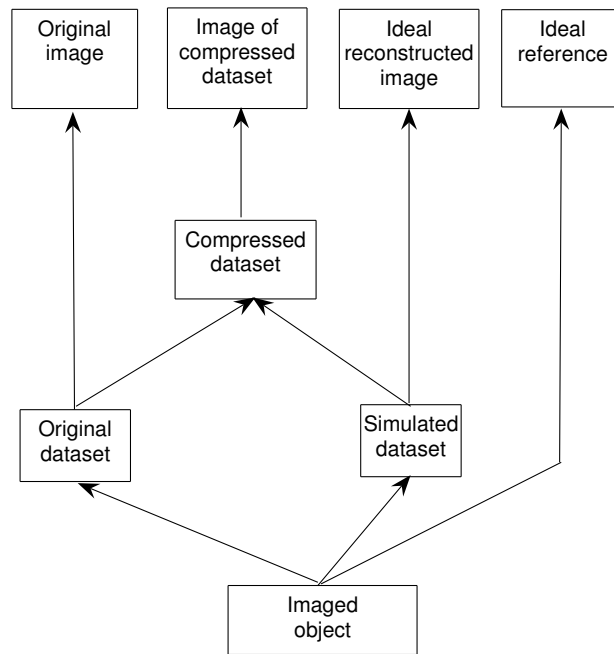


Figure 3.1: Used terminologies in this thesis.

The image of compressed dataset refers to the images reconstructed with compressed datasets using lossy compression methods at different compression ratios.

The image reconstructed with uncompressed real or simulated dataset is called “original image”. The real A-scans are measured with the ultrasound transducers and filtered with an analog filter before saving in PC.

The A-scan which consists of ultrasound pulses without the irrelevant part is termed as “ideal A-scan”. The image reconstructed with the ideal A-scans is named as “ideal reconstructed image”. The ideal reconstructed image is the theoretical best image which can be achieved by USCT. The aperture of transducers, the center frequency and bandwidth of the coded excitation and the reconstruction method decide on the quality of the ideal reconstructed images. The quality of the ideal reconstructed image is not perfect because of the characteristics of the reconstruction algorithms and parameters. The degradation of the ideal reconstructed image due to these reasons are termed as “reconstruction artifacts” or “system noise”.

The perfect image which has merely the information of imaged objects is termed as “ideal reference”. The contents of the ideal reference are the ground truth of imaged objects. In USCT images the ground truth is the echogenicity [74, 75] of objects, since the reflectivity, i.e. the first order deviation of sound impedance, of the objects are imaged qualitatively. The ideal reference image includes the object contours and has no background noise.

**Analysis** The image quality of compressed datasets is influenced by A-scan properties, compression methods, limited number of A-scans and characteristics of reconstruction method.

Based on the analysis in section 2.3, real A-scans are influenced by following sources:

1. Electronic and environment noises.
2. Digitizing noise during quantization of sample amplitudes.
3. Reflected ultrasound pulses by the wall of cylindrical container in USCT setup.
4. Multiple scattering.

5. Time position of the ultrasound pulse which is affected by the sound speed in media.

Compression may change the contents of A-scans. E.g. the noise is expected to be partly removed. If the implemented compression methods are improperly selected for keeping the useful content and removing the irrelevances in A-scans, the quality of image is decreasing with the order of compression; the compression methods are usually optimized on certain properties of A-scans, e.g. shape of ultrasound pulse. However the ultrasound pulses in A-scans may have various deformations, thus performances of the compression methods change with these deformations. The deformation of ultrasound pulses and the effect of compression on A-scans cannot be predicted (see section 2.3.5).

Characteristics of the reconstruction method results in the reconstruction artifacts in USCT images as discussed in section 2.2.3. Ideal reference of USCT image which is defined in above terminologies, is designed to show the image contents independent of reconstruction methods. The contents of an ideal reference of an USCT image are affected merely by the useful information of A-scans, i.e. amplitude and time of arrival of ultrasound pulses. Compared to the ideal reference the additional contents of images are the reconstruction artifacts which are reconstructed with the amplitude and TOA of ultrasound pulses. The reconstruction artifacts may increase with the compression order. E.g. the background noise of the images reconstructed with the compressed datasets may increase due to the reduced number of overlapping ellipsoids during image reconstruction.

### **3.1.3 Requirements and difficulties**

Objective instead of subjective results are necessary for evaluation of USCT images. The evaluation results should be reproducible. These results of image quality evaluations should not be dependent on subjective decision. The objective evaluations are used for comparing the image quality of compressed datasets.

The second requirement is the high consistency with human perception. The final users of USCT images are experts in diagnosis, who analyze the symptoms of patients using the useful contents in the USCT images. The useful contents are the imaged objects. The quality of objects represented in images is scored with the evalua-

tion method. These scores of evaluated images should be similar to the perceived results by the experts.

The third requirement is to represent properly the variation of image quality due to compression artifacts, since the purpose of developing an image quality estimator is to determine the optimal compression algorithm for 3D USCT. The images of compressed datasets with the high quality are expected to have relatively high scores.

**Difficulties** An image quality based evaluation method for assessment of signal compression is based on assessing image quality of compressed datasets. There are generally two difficulties for selection of the method for the suitable image quality assessment: the definition of a suitable reference image and of an efficient image quality estimator.

The quasi original image reconstructed from an uncompressed dataset cannot be used as the reference image. The original A-scans contain not only the information for image reconstruction, i.e. amplitude and time of arrival (TOA) of ultrasound pulses [69], but also irrelevances, e.g. noises. Therefore, the contents of the image reconstructed with these original A-scans include not only the imaged objects but also irrelevances which affect evaluating the image of compressed datasets. Due to the reduction of distortions in the ultrasound signals the images reconstructed with compressed datasets may have even higher image quality than the images reconstructed with uncompressed data. With a low quality image as reference, the evaluation results of compression methods might not give proper evaluation results.

Design of a reference image is difficult. The precise positions of imaged tissues in breasts are difficult to be measured. The acoustic properties of these tissues are usually unknown. Therefore the design of a reference image based on geometry and acoustic properties of breast is not feasible.

Based on above discussion about a suitable reference image it is better to have the ground truth of imaged objects, i.e. ideal reference, from a simulation. Another possibility is to design the ground truth by human experts. This is always the method of choice in clinical solutions where it is not possible to get the ground truth with objective measurements.

The objective image quality estimators are often defined based on the distribution of pixel values in images [21]. E.g. such estimators are often based on the differences of gray values in images. The image quality estimators in USCT are expected to be efficient for the breast images.

The significant artifacts in images due to compression reduce the performance of the available image quality estimators. The imaged objects in images of compressed datasets may vanish with a high compression ratio. The great variation of image contents due to strong artifacts is difficult to be scored properly with the image quality estimators which are sensitive to a small distortion in images.

### **3.1.4 Summary**

The compressed datasets are scored to compare the performances of compression methods. The suitable compression method is then selected based on these scores. The image quality based evaluation method is capable of scoring not only the compression artifacts but also the different reconstruction methods. A suitable compression method is selected for a fixed reconstructed method. Additionally different reconstruction methods in USCT can be compared by reconstruction with an identical dataset. It is expected that an optimal image quality is achieved from different compression and reconstruction methods.

## **3.2 Image quality estimators in literature**

The state-of-the-art image quality estimators are reviewed to find a suitable one for evaluation of compression methods in USCT. The image quality estimators are classified into subjective and objective estimators. Within the objective estimators the estimators are classified into no-reference or reference based estimators according to the use of a reference.

### **3.2.1 Subjective estimators**

The subjective estimator uses the humans as observers. These estimators are mostly used for clinical evaluations of medical images.

The significant advantage of subjective estimators is the high consistency with the human perception.

Traditional subjective image quality evaluation for ultrasound images is the receiver operating characteristics curves method (ROC) based on psycho-visual studies [76, 77]. The ROC analysis provides tools to select optimal models for diagnostic decision making [78].

Mean vote score (MVS) is a commonly used subjective estimator for research of image processing. A number of observers view an image and score its quality. The mean value of these achieved scores is then used as mean vote score [79].

Subjective methods have disadvantages to be time consuming, adding workload for the physician, expensive [80], knowledge dependent, and often irreproducible. Thus objective estimators are developed for evaluation of image quality.

### **3.2.2 Objective estimators**

Objective image quality estimators evaluate the image quality with mathematical tools which are developed to get reproducible results. The objective estimators are implemented in recent years for the development of ultrasound imaging technologies [81].

The significant disadvantage of the state-of-the-art objective image quality estimators is their low consistency with human perception. These estimators are designed for special implementations of image processing aiming at an increased consistency with the human perception. The characteristics of the processed images are changed by noise and consequently the performance of the estimators decreases. Due to this non-robust behaviour the state-of-the-art estimators are not suitable for evaluation of images of the USCT.

A couple of concepts have been proposed particularly for evaluating the quality of the whole ultrasound imaging system. The computational observation [82], resolution integral [83] and contrast resolution [84] are proposed by using specific characteristics of ultrasound [83] or special phantoms [82, 84] for conventional diagnostic ultrasound scanners. The assumptions are that the acoustic properties and position of imaged objects are available, i.e. the exist of an objective reference image which is not the case in US imaging of

living objects.

The state-of-the-art objective estimators are classified into reference and no-reference based image quality estimators. No-reference estimators evaluate the image quality without the dependency on the reference image. No-reference estimators are based on Human Visual System (HVS) [85, 86]. The HVS was analyzed to construct a human vision model [87] in order to improve the consistency of objective estimators with the human perception. The parameters in the human vision model come from practical experiences corresponding to the psychophysical features of HVS [88]. Because of the difficulty to validate and generalize these experiential values and the limited understanding of the HVS, the human vision model is difficult to be implemented as an objective image quality estimator. Until now no-reference estimators have not been often used [80].

Reference based image quality estimators are widely implemented [88, 86, 89, 81]. The quality of images is scored by comparing the reference and distorted images. The comparison process is usually defined as a function of pixel values in reference and distorted images. It is hard to get a function which correlates the image distortions with the human perception. Therefore these scores often lead to evaluation results which are not consistent with the human perception [80, 90]. Peak-signal-to-noise-ratio (PSNR) and mean square error (MSE) are the commonly used reference based estimators.

The state-of-the-art reference based image quality estimators are usually sensitive to a certain type of distortions in images [80]. For example, the most commonly used estimator to calculate the difference between two images is the peak signal to noise ratio (PSNR) which is defined in [91]. PSNR is sensitive to the variation of contrast in distorted images. An other example is the average mutual information (AMI) which has the advantage to compare the distorted images with similar homogenous regions of tissues, i.e. similar gray value distributions [92]. But AMI is not suitable for evaluation of images with purely defined contours of objects or strongly blurred objects. Therefore AMI is used for experimental images with slight distortions and may give insufficient results with strong distortions in images.

The evaluation results [81, 90, 93, 94] show, that the performance of these estimators changes with the distortion types and the ob-

jects in the images. None of these estimators is satisfying at a confidence level of 95 % for arbitrarily distorted datasets [90, 93] or provide a performance which is strongly correlated with the human perception [94].

### 3.3 Assessment of no-reference image quality estimators

Due to the difficulties to achieve a suitable reference image for evaluating images of compressed datasets in USCT, in this work no-reference image quality estimators were evaluated at first. Three no-reference objective image quality estimators are tested with artificial images where four types of distortions are added.

#### 3.3.1 Selected no-reference estimators

- Global contrast: Various definition of image contrast were proposed to simulate the human perception for the image contrast [95, 96]. The difficulty is that the human perception is influenced by different factors, e.g. experiences, psychology, environment, etc. These factors are difficult to be simulated by a mathematical score of an image.

The widely used definition of global contrast is the dynamic range of pixel values in an image.

$$\text{Global contrast} = \text{Var}(X)$$

$$\text{Var}(X) = E[(X - \mu)^2] = E(X^2) - \mu^2$$

The mean of the pixel gray values in the image  $X$  is defined as  $\mu = E(X)$ . In order to test the performance of the global contrast, images with different types and grades of artificial distortions are scored with this no-reference estimator.

- Modulation transfer function (MTF) is used as a metric for image quality, lens performance, feasibility of sub- or all photographic system. It represents the transfer ability of an imaging system from an object to the image [97].

MTF is used to describe how the details of an images change with the spatial resolution. The detail of images is represented

with the difference between the maximum and the minimum gray values (contrast). The spatial resolution is calculated with the spatial frequency. MTF is usually plotted as a function of the spatial frequency for evaluation of the imaging system. MTF curve decreases if the details of the picture with increasing spatial resolution are getting smaller. The maximum value of MTF at the spatial frequency of 0 is normalized to 1 [98]. The MTF curve with a faster decreasing tendency represents a lower performance of the imaging system.

MTF can be calculated with the absolute value of the two dimensional Fourier transform of point spread function for an imaging system [99]. The difficulty to calculate MTF with this method is to design an object for testing arbitrary resolutions of the imaging system, e.g. the arbitrary small size of a point as an object [100].

The general method for measurement of MTF is based on the contrast of original and distorted images at a certain frequency [101]. The contrast here is defined as the difference between the maximum and the minimum gray values of an image. The MTF at the frequency  $f$  is defined as:

$$MTF(f) = \frac{\text{Contrast of distorted image at frequency } f}{\text{Contrast of original image at frequency } f}$$

In order to analyze the performance of MTF for image distortions, the values of MTF for different distortion grades are measured to achieve the MTF curve for the corresponding distortion type. The tendencies of these curves are compared with the human perception for these distortions.

- Entropy: The entropy of an image  $X$  is used to estimate the information content which is represented by the value of pixels in an image [18]. The entropy  $H(X)$  is defined as follows:

$$H(X) = - \sum_i P(a_i) \cdot \log_2 P(a_i)$$

where  $a_i$  is the  $i_{th}$  possible gray value of image  $X$  with a probability of  $P(a_i)$ .  $a_i$  is in the range from 0 to 255.

The entropy values of images with different distortions represent the variation of the image quality. The relationship be-

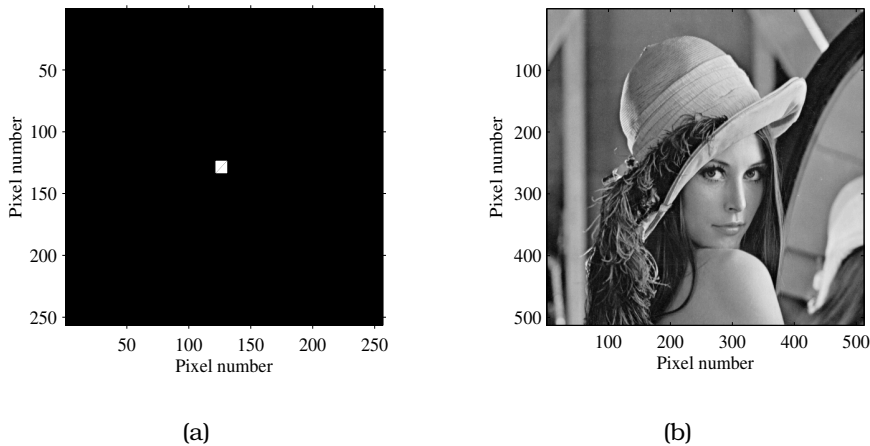


Figure 3.2: Artificial image with (a) a small point in the center (b) Lena. For this picture the size of the small point in the image (a) is larger than one pixel.

tween the calculated entropy values and designed distortion grades is analyzed to get the performance of the entropy as a no-reference estimator.

### 3.3.2 Artificial images and distortions

A couple of images are used to analyze the properties of no-reference estimators. These simulated images are designed with the structure of different complicacies. Two of them are shown as examples. In the center of the first artificial image there is only one pixel with a gray value of one, the gray values of other pixels are zero. The pixel in the center is used to simulate an ideal point. The size of this image is  $256 \times 256$ .

The second image called Lena is a commonly used example for image processing. This image has a relative complex structure in comparison to the first image. The size of this image is  $512 \times 512$  as shown in Fig. 3.2.

These artificial images are superimposed with general distortions in compressed ultrasound images [76]. Four types of these distortions as example are simulated at different grades. The basic ideas for design of these distortions are shown as follows:

- Offset changed: The offset means the average value of the pix-

els. Offset change of an image is simulated by adding a constant to each pixel value of the image. This distortion is used because pixels of the image may be changed during data compression.

- Blurred: The image is filtered with the Gaussian low-pass image filter. The distortion grades are changed by using various bandwidths.
- Noise: White noise with a normal distribution is added onto the image. The white noise is generated by random numbers. The variances of the random numbers are changed to vary the distortion grades.
- Quantization noise: The pixel values of images are quantized. The residues which are removed by rounding the pixel values represent the quantization noise. The grades of quantization noise are changed with the positions of rounded significant digits in the gray values of image pixels.

### **3.3.3 Analysis results**

The different distortion types are analyzed individually. Each distortion type is designed with linearly increasing grades. The distortion at a certain distortion grade is added into the artificial images to produce the distorted images. These distorted images are scored with the selected no-reference image quality estimators. The tendency of the achieved scores for each distortion type is observed and plotted as the function of the distortion grades.

The experimental results are plotted schematically in Fig. 3.3. These schematic plots are based on the quantitative analysis of the real results with many artificial images. The horizontal and vertical axes represent the increasing distortion grades and values of image scores, respectively. The lines show the tendency of the scores changed with the distortion grades.

The zigzag shape of the lines means that the performance of the estimator is unstable to various grades of the corresponding distortion type. These results show that none of the estimators is able to represent coherently the variation of distortion grades for all four distortion types.

The experimental results are consistent with the theoretical analysis. The calculated output of the estimators is based on the gray

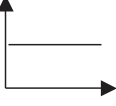
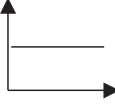
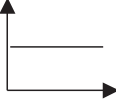
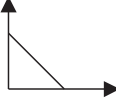
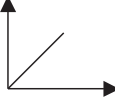
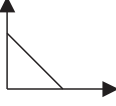
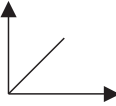
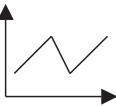
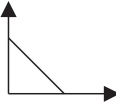
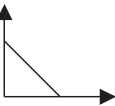
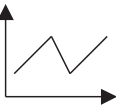
measure \ distortion	Global contrast	Entropy	MTF (sharpness)
Offset Changed			
Blurred (Gaussian low-pass)			
Noise (white noise normal distribution)			
Quantization noise			

Figure 3.3: Tendency of no-reference objective image quality changed with different types of distortion effects in artificial images. Horizontally the grade of distortion and vertically the change of score of the estimator is schematically shown.

value of each pixel in the image. The pixel values vary with the definition of distortion types and grade of distortion. By definition all three used estimators have a very different behaviour. Especially unsatisfactory is the different normalization and sensitivity of the estimators at small distortions. A similar behaviour of all estimators would be expected as reasonable limiting value for distortions approaching zero. None of these estimators may handle all of these distortions at the same time due to the Fig. 3.3.

### 3.4 Quality estimators with a reference

A reference is necessary for the reference based estimators. These image quality estimators are suggested for USCT to overcome the

shortcomings of the no-reference estimators discussed in section 3.3. The process to use the reference based estimators for evaluation of signal compression is shown in the flowchart of Fig. 3.4. The distorted image is the image reconstructed with the compressed and distorted A-scans. The difference between reference and distorted images are scored with the proposed estimators. The compression method with high values of scores has a good performance for signal compression in USCT. I.e. here the quality of compressed signals is defined by the quality of reconstructed images. The compressed A-scans are not compared directly due to the reasons discussed in section 3.1.

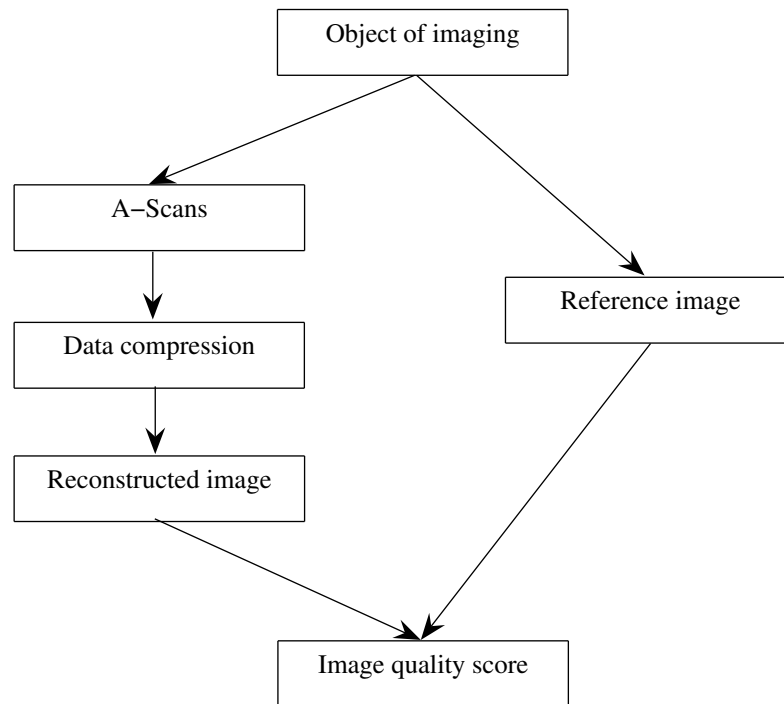


Figure 3.4: Basic process for evaluation of signal compression.

The standard reference based estimators are introduced at first. The advantages and disadvantages of these estimators are analyzed. New estimators are designed to improve the performance of these standard estimators. The evaluation method of estimators is ex-

plained at the end of this section.

### 3.4.1 Selected reference based estimators

There are lots of reference based estimators designed for evaluation of image quality. In this work seven standard reference based estimators are selected, since they are defined for representing different characteristics of image performances. For simplicity these estimators are tested with 2D images instead of 3D images. I.e. two axes are used to describe the positions of pixels.

Before the mathematical definitions of these estimators and the meaning of the symbols used in the definitions have to be explained.  $X$  stands for the reference image. The gray value of the pixel at the row  $i$  and the column  $j$  is represented with  $x(i, j)$ .  $Y$  is the distorted image which has to be scored with the estimators. The corresponding gray value for the pixel at the row  $i$  and the column  $j$  is  $y(i, j)$ . The indexes of the row and the column are at the range from 1 to  $m$  and from 1 to  $n$  respectively. Some variables used in the definitions of estimators are explained at first, i.e. mean values, variances, and covariance:

$$\bar{x} = \frac{1}{m \cdot n} \sum_{i=1}^m \sum_{j=1}^n x(i, j)$$

$$\bar{y} = \frac{1}{m \cdot n} \sum_{i=1}^m \sum_{j=1}^n y(i, j)$$

$$\sigma_x^2 = \frac{1}{m \cdot n - 1} \sum_{i=1}^m \sum_{j=1}^n (x(i, j) - \bar{x})^2$$

$$\sigma_y^2 = \frac{1}{m \cdot n - 1} \sum_{i=1}^m \sum_{j=1}^n (y(i, j) - \bar{y})^2$$

$$\sigma_{xy} = \frac{1}{m \cdot n - 1} \sum_{i=1}^m \sum_{j=1}^n (x(i, j) - \bar{x}) \cdot (y(i, j) - \bar{y})$$

Each pixel of the reference and distorted images are considered to score the relative changes between the distorted and the reference images. Thus the definitions of these estimators are based on the

gray values of the pixels. The mathematical definitions of these selected estimators are described by the following formulas.

1. **Peak signal to noise ratio (PSNR)** is the mostly used image quality estimator. The distance of gray values between two images is defined as the normalized mean square error with the maximum value of the reference image [24].

$$PSNR = 10 \log_{10} \frac{Maximum(X)}{MSE}$$

$$MSE = \frac{1}{m \cdot n} \sum_{i=1}^m \sum_{j=1}^n \|(x(i, j) - y(i, j))\|^2$$

2. **Structure similarity measure (SSIM)** is an estimator proposed for evaluating the structure variation of the imaged objects [85]. SSIM is proven to be efficient for scoring images compressed with JPEG or JPEG2000 [86]. The definition of the SSIM is a product of three simple estimators which are used to represent the variations of the luminance, contrast and structure in distorted images.

$$SSIM = \frac{\sigma_{xy}}{\sigma_x \sigma_y + c} \cdot \frac{2\bar{x}\bar{y}}{\bar{x}^2 + \bar{y}^2 + c} \cdot \frac{2\sigma_x \sigma_y}{\sigma_x^2 + \sigma_y^2 + c}$$

where  $c$  is a constant.

3. **Average mutual information (AMI)** is widely used for image registration [92, 102]. The entropies of pixel values in reference and distorted images are calculated to show the quality of distorted images.

$$AMI = H(X) + H(Y) - H(X, Y)$$

$$H(X) = - \sum_m P(x_m) \cdot \log_2 P(x_m)$$

$$H(Y) = - \sum_n P(y_n) \cdot \log_2 P(y_n)$$

$$H(X, Y) = - \sum_k P(C_k) \cdot \log_2 P(C_k)$$

$H(X)$  and  $H(Y)$  are the Shannon entropies of image  $X$  and  $Y$ , respectively.  $m$  and  $n$  are numbers of possible gray values in image  $X$  and  $Y$ , respectively.  $H(X, Y)$  is the Shannon entropy of the joint histogram, i.e. two-dimensional histogram of the gray level combinations occurring at same image positions. The gray values at the same pixel position of the reference and the distorted images make a pair of gray values. Each pair represents a gray level combination of two images and is denoted by  $C_k$ , where  $k$  is the index of this combination.  $P(C_k)$  describes the probability of  $C_k$  within all possible gray level combinations.

4. **Normalized mutual information (NMI)** is similar to AMI. The sum of the image entropies is normalized to the joint entropy  $H(X, Y)$ . The NMI is more sensitive to the variation of joint entropy than AMI [92].

$$NMI = \frac{H(X) + H(Y)}{H(X, Y)}$$

5. **Homogeneity based measure (Homog)** was designed to observe the variation of image homogeneity [103]. The images are filtered with the high pass image filter  $F = [-1 \ 2 \ -1]$  in horizontal, vertical and diagonal directions. The local homogeneity of images is calculated with filtered images by setting the gray values of the non-zero pixels to 1. The relative variations of the local homogeneity and the luminance between reference and distorted images are combined to defined the estimator Homog [103].

$$Homog = \frac{2F_x F_y}{F_x^2 + F_y^2} \cdot \frac{2\bar{x}\bar{y}}{\bar{x}^2 + \bar{y}^2}$$

where  $F_x$  and  $F_y$  are the filtered images  $X$  and  $Y$ .

6. **Gradient Vector Flow (GVF) and AMI (GVFMI)** combines the advantages of the GVF and the AMI methods [104]. GVF is defined as a field of an image. This field represents the influence of imaged objects on the image. The gradient of the edge map is calculated at first. Each pixel value of GVF corresponds to the spatial diffusibility of the calculated gradient field, so called Gradient Vector Flow (GVF) [105]. The average mutual information of GVF of the reference image is compared with the direct distorted image. The GVF is used to increase the influence areas of the imaged objects in the reference image.

$$GVFMI = AMI(GVF(X), Y)$$

7. **Normalized gradient vector (NormGrdt)** was proposed for registration of magnetic resonance images of the brain [106]. The gradient vectors ( $Gt_h, Gt_v$ ) at the same position (i,j) and horizontal (h) and vertical (v) directions of reference (X) and distorted images (Y) are calculated.  $t$  denotes the reference or the distorted image. The inner product between these vectors is calculated to deduce the angle between them. The cosine value of the angle at each pixel is combined to calculate the NormGrdt. A large value of the NormGrdt represents a significant difference between reference and distorted images.

$$Gt(i, j)_h = t(i, j) - t(i + 1, j)$$

$$Gt(i, j)_v = t(i, j) - t(i, j + 1)$$

$$|Gt(i, j)| = \sqrt{Gt^2(i, j)_h + Gt^2(i, j)_v}$$

$$Gx \cdot Gy = \frac{1}{m \cdot n} \sum_{i=1}^m \sum_{j=1}^n \frac{Gx(i, j)_h Gy(i, j)_h + Gx(i, j)_v Gy(i, j)_v}{|Gx(i, j)| \cdot |Gy(i, j)|}$$

$$NormGrdt = Gx \cdot Gy$$

A comparison of the sensitivity for selected reference based estimators is listed in Table 3.1. Each estimator is sensitive or insensitive to different features in the image. These estimators test only special features of the images.

### 3.4.2 An optical flow based estimator

#### 3.4.2.1 Optical flow

Optical flow was mostly used for pattern recognition, imaging processing, motion estimation, etc. The optical flow is a vector field used to represent the relative motion of the object between a sequence of images within a movie or due to the position changes of observers. Each vector corresponds to the relative variation of the gray values at the same pixel positions in the neighboring images [107].

Abbreviation	Sensitive	Insensitive
PSNR	Gray value changes	Structure changes
SSIM	Gray value and significant structure changes	Insignificant structure changes
AMI	Gray value changes	Significant structure changes
NMI	Gray value changes	Significant structure changes
Homog	Homogeneity changes	Various grades of blurs
GVFMI	Insignificant structure and gray value changes	Significant structure changes
NormGrdt	Structure changes	Gray value changes

Table 3.1: Sensitivity of used image quality estimators, for definitions of the abbreviations see section 3.4.1.

The optical flow is calculated based on the motion constraint equation [108]:

$$\nabla I \cdot \vec{n} = I_t$$

where  $\nabla I$  is a spatial intensity gradient of image  $I$ ,  $\vec{n}$  is optical flow.  $I_t$  is the partial differentiation of image intensity with respect to time. In this case  $I$  is the reference image  $X$  and  $I_t$  is the intensity difference between reference and distorted images  $\|X - Y\|$ . The unknown  $\vec{n}$  in motion constraint equation is solved by using a pair of additional partial differential equations proposed by Horn and Schunck [109]. These equations are built with the minimization of the brightness variation and smoothness difference between neighboring images. The finite difference method is used to get the iterative solution of these partial differential equations. The assumption of optical flow based methods is that the objects in neighboring images have a similar structure and the gray value of noise is small relative to the gray value of objects in images [110].

### 3.4.2.2 Design of estimator

The idea to score the image of compressed datasets with the optical flow based estimator is to calculate the included compression artifacts with a vector field. The differences between the reference and the image of compressed datasets are represented by an optical flow. Each vector component in the vector field stands for a relative variation of gray values from the reference to the image of compressed dataset at the same position.

Reference and image of compressed dataset → Optical flow image

The entropy of the vector magnitudes is calculated as the entropy of the optical flow. The inverse of this entropy value is used to represent the image score of compressed datasets and is named optical flow based estimator (OFintenEtpy).

$$\text{OFintenEtpy} = \frac{1}{\text{Entropy Magnitude Optical Flow}}$$

A large difference between the reference and the image of compressed dataset results in a large entropy of the optical flow from the reference to the image of compressed dataset. Thus it corresponds to a low image quality of the image, i.e. a low value of OFintenEtpy. The images with a high similarity to the reference image are scored with large values of OFintenEtpy.

### **3.4.2.3 Assessment of performance**

In order to calculate the performance of the OFintenEtpy, the reference and distorted images have to be designed. The images with different distortion grades are scored with the OFintenEtpy. The scores are analyzed based on the given grades of distortions.

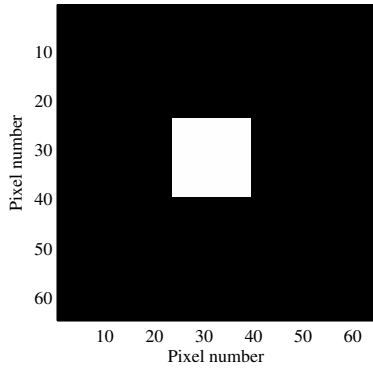
The reference image is designed in fig. 3.5(a). One of the distorted images as an example is shown in fig 3.5(b). The optical flow between the reference and the distorted image is shown in fig 3.5(c). Each arrow in the optical flow represents a vector of optical flow at the corresponding position.

The achieved optical flow is analyzed based on the characteristics of reference and distorted images. For example, the white block in distorted image has a smaller size than that in the reference image, therefore the vectors of the optical flow on the edge of the block shown in the fig. 3.5 point to the center of the image.

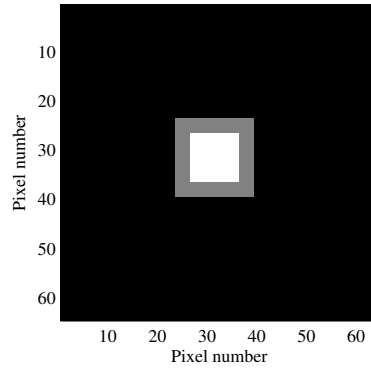
## **3.4.3 Committee model based estimators**

### **3.4.3.1 Motivation**

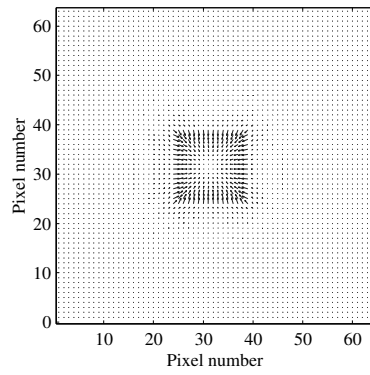
The basic idea to design a new image quality estimator is to combine the very different qualities of state-of-the-art estimators. It was shown in the chapter before that the presented different estimators



(a)



(b)



(c)

Figure 3.5: (a) Artificial image with a block shape object in the center as the reference image. (b) The distorted image. (c) The optical flow between reference and distorted images represented with a 2D image.

are sensitive to different qualities of the images. The images of compressed datasets are significantly different from the ideal reference which consists of merely the ground truth of imaged objects. To overcome the possible weakness of individual estimators a committee model is proposed. The committee model combines the estimators in section 3.4.1 to a new image quality estimator.

### **3.4.3.2 Structure of committee model**

A committee model is defined here as a method to improve estimates [111, 112, 113]. The committee model is regarded as a combination of several predictors to form a single and better predictor [114]. The predictors are termed as the members of the committee. The members of the committee in this research are selected image quality estimators described in section 3.4.1. A committee model combines the scores of these scores to arrive at an overall estimate of image quality which is supposed to have a better performance than any of them alone [115].

A generalized committee model is defined as a weighted combination of scores. I.e. some scores make better predictions than others [116] and get therefore a higher weight. The prediction error of the generalized committee model is not larger than that of the averaging committee which considers each score as equally important. In this work the generalized committee is used to construct the committee model based estimator (CMM).

### **3.4.3.3 Training process**

The goal of the training process is to achieve the weights of the estimators in CMM. The inputs are the expected scores defined by the observers and depend on the characteristics of the training cases. The responses are the achieved scores of the training case estimated with the different estimators. The differences between the inputs and the responses are called the errors. The weights of the estimators are calculated by minimizing the sum-of-squares of these errors [117, 118]. The sum of the achieved weights for each committee model is defined as one to avoid the zero solution of the weights [116].

The achieved weights are used to construct the CMM. The weighted

image scores of compressed datasets estimated by the estimators are summed up to construct the score of the CMM. Then the scores of CMM for different images of compressed datasets are compared to evaluate the compression artifacts in USCT.

The error  $\epsilon_{i,j}$  for a single estimator is defined as follows:

$$\mathbf{Estimator}_j(\mathbf{i}) = \mathbf{Score}(\mathbf{i}) + \epsilon_{i,j}. \quad (3.1)$$

where “**Score**” is the expected score by the observers for the training case with the index  $i$ . **Estimator** is the calculated score of an estimator with the index  $j$ .  $\epsilon$  stands for the error of estimate calculated by  $\mathbf{Estimator}_j(\mathbf{i}) - \mathbf{Score}(\mathbf{i})$ .

In case the averaging committee model is used the error is shown as follows:

$$\begin{aligned} \mathbf{Estimator}_{\text{averaging}}(\mathbf{i}) &= \frac{1}{\text{Number of all estimators}} \sum_j \mathbf{Estimator}_j(\mathbf{i}) \\ &= \mathbf{Score}(\mathbf{i}) + \epsilon_i. \end{aligned} \quad (3.2) \quad (3.3)$$

In order to minimize the error for the single estimator, the single estimator is optimized with the least squares method by adding the coefficients  $\alpha$  and  $\beta$ . The error for the least square solution satisfies the Gauss-Markov theorem. According to the Gauss-Markov assumptions, the expected value of the error is zero [119, 120, 121].

$$\mathbf{Estimator}_{\text{optimal},j}(\mathbf{i}) = \alpha_j(i) + \beta_j \mathbf{Estimator}_j(\mathbf{i}) = \mathbf{Score}(\mathbf{i}) + \epsilon_{i,j}. \quad (3.4)$$

For the generalized committee model the weights of the optimized estimators are calculated with the least squares method for a reduced error further [116].

$$\mathbf{Estimator}_{\text{optimal}}(\mathbf{i}) = \sum_j \mathbf{w}_j (\alpha_j(i) + \beta_j \mathbf{Estimator}_j(\mathbf{i})) = \mathbf{Score}(\mathbf{i}) + \epsilon_i. \quad (3.5)$$

where  $w$  is the weight of the estimators and

$$\sum_j \mathbf{w}_j = 1 \quad (3.6)$$

The number of training cases  $i$  corresponds to the product of the number of distortion types multiplied with the distortion grades. The **Score** of training cases are based on the distortion grades and normalized from one to ten in this work. The least squares method and the comparison of the different errors are implemented in Matlab [58].

#### **3.4.3.4 Training cases**

Training cases are used to learn the input-response of the committee model. Simulated distortions are used as training cases. The selected distortions added in the training cases are based on the empirical observations of degraded images caused by data compression.

For this purpose the original image is reconstructed with an uncompressed dataset, and the various simulated distortions are added to this original image. Each simulated distortion type and grade corresponds to a training case.

CMM is constructed based on differences between training cases. These differences vary with the simulated distortions. Thus CMM is designed for scoring distortion instead of the reconstruction artifact.

The reconstruction artifacts are considered as the constant components for the designed training cases. However the reconstruction artifacts vary with the implemented data compression type and size of compression. These variations of the reconstruction artifacts are neglected for images of compressed datasets in the range of small compression ratios if the reconstruction method is not changed.

#### **3.4.3.5 Simulated distortions in USCT images**

Various distortion types and grades are simulated for different artifacts in images of compressed datasets. The distortion type are selected based on the observation of image quality. The analysis of data compression on A-scans is helpful to find the distortion type but this analysis is not decisive, since the quantitative relationship between the A-scans and the reconstructed image is unknown. The distortion types are evaluated by the performance of the achieved committee model.

The following distortion types are achieved by comparison of the compressed and original images. Each type is simulated at 10 linear distributed grades with the image processing toolbox in MATLAB [58]. The recipes for design of these distortions in experiments are based on the following processes, functions and parameters.

- Quantization: In lossy compression, the amplitudes of the A-

scans are quantized with some threshold value. The quantized A-scans are used to reconstruct 3D images. The quantization error in signal may be transferred to the image of compressed dataset and degrades the quality of reconstructed images. E.g. if the quantization size equals the maximum value of the amplitude in A-scans, the gray values of all pixels in the image will be set to zero.

The quantization error is simulated with the following steps: save the gray values of the pixels in images with the double or float format; normalize the saved gray values to the range from 0 to 1; remove the fraction parts in the normalized values with the function `round` in Matlab.

- Uniform noise: The noise in images of compressed datasets are due to noise in the A-scan. The noise in A-scans was approximated by the white noise. This noise may be superimposed to the gray values of the image in USCT and yields the background noise.

The variation of the background noise due to the compression process is simulated in this work with uniformly distributed white noise. The gray values of images are normalized to the range from 0 to 1; the uniform noise is added to the normalized images. The uniform noise is created using the function `rand` in Matlab with the grades from  $-40$  dB to  $-20$  dB compared to the maximum gray value in the images.

- Decreased contrast: e.g. blurred or eroded images. The compression of A-scans decreases contrast between objects and background. The blurred image is used to simulate the reduced contrast of images. The image is blurred by filtering with a circular averaging filter. The eroded images are filtered using function `imerode` in Matlab.

The selection of the size of the filter is based on the image resolution in the experiments. Due to the theory of spatial resolution [122], the image resolution of USCT is affected by the used ultrasound pulse length and the aperture of ultrasound transducers. E.g. the spatial resolution of USCT is 0.1mm for some simulated datasets, the maximum size of the filter is set to 0.5mm.

- Deformation of the object: e.g. resized or dilated object. The contours of imaged objects represent the size of objects. An imprecise mapping of the information in ultrasound pulse, e.g. time of arrival, due to data compression may change the contour positions of reconstructed objects. The object with enlarged or diminished size is simulated as resized or dilated object in distorted images.

For resized object the pixel number of gray value corresponding to the object in images is changed by using function “imresize”. The size of the object is changed maximally by about 5% of the original size of the image to vary the grades of these distortions.

- Overlapping distortions: e.g. overlapping resized objects: more than one distortion type might occur at the same image with different impacts. E.g. to simulate the interaction of the resized object and the unchanged background noise in an image, the overlapping resized object is simulated. The resized objects for different resizing grades are added in each case to the original image.

#### **3.4.4 Evaluation of reference based estimators**

The basic strategy for the evaluation of proposed reference based image quality estimators is to compare the achieved scores of the distorted images. The influences of the compression ratios, the imaged objects and the selected reference images are considered. The comparison results are analyzed to achieve an estimator with a high performance for data compression in USCT.

The comparison of scores is carried out with different ranges of compression ratios. Low and high compression ratios are the range of smaller than 20 and of larger than 100, respectively. At high compression ratios the imaged objects become fuzzy or no longer recognizable. However the variation of image quality at low compression ratios is usually not significant. An estimator may have different performances at ranges of low and high compression ratios. In this work the estimator with a high performance at low compression ratios is selected. At the same time, for the estimators a suitable reference image has to be found as discussed in the next chapter.

## 3.5 Achieving a reference for evaluation

The reference images are achieved from the information of imaged objects. The difference between the reference image and images of compressed datasets is used to show the influences of data compression on the quality of image.

### 3.5.1 Original image based reference

#### 3.5.1.1 Analysis of original images

The advantage of using the original image as reference image is that the original image is simple to be achieved for USCT. In this work the original image is not used as the reference image for evaluating images of compressed datasets. The original image may have a lower image quality than an image of compressed dataset.

It is expected that the original image is pre-processed properly to improve its quality. The environment noise in A-scans and the system noise due to the reconstruction method are sources of noise in the original image. This noise has to be reduced in the original image.

#### 3.5.1.2 Filtered original images

The idea to filter original images for an improved image quality is to select an image processing method based on characteristics of original images. The background noise in the original images has to be reduced to improve the contrast of images. The imaged objects change due to the background noise. The change has to be considered during the design of the image processing methods.

To enhance the edge detection of objects in vertical and horizontal directions, Sobel-filters are used. The implemented Sobel operators

in experiments are:  $FY = \begin{bmatrix} 1 & 2 & 1 \\ 0 & 0 & 0 \\ -1 & -2 & -1 \end{bmatrix}$  and  $FX = \begin{bmatrix} 1 & 0 & -1 \\ 2 & 0 & -2 \\ 1 & 0 & -1 \end{bmatrix}$

The contours of the imaged objects are important areas in the USCT images. After the enhancement of the object edges, the quality of the original image is improved as there is no noise. The filtered original image is saved as the reference image for evaluating images of compressed datasets.

### **3.5.1.3 Assumptions**

In order to get a reasonable reference image, the design of the field of interest is based on the following assumptions about the original reconstructed images:

1. In the original image the tissues, i.e. the contours of the objects within the breast are on the right positions. These contours can be distinguished from background noise.
2. The structure of the object contours have significant different patterns than the background noise.
3. The gray values of the background noise have a random distribution in the original image.

### **3.5.2 Simulated reference**

A reference image with the ground truth, i.e. the ideal reference, is designed using a simulated dataset. The method to construct the imaged objects as ideal reference is based on the imaging characteristics of USCT, i.e. ultrasonic reflectivity tomography. The reflectivity of imaged objects depends on the acoustic properties of neighboring media.

The simulated datasets of A-scans are produced by an ultrasound simulation software Wave3000 [45] and then converted to the data format used in Matlab with a user friendly interface [123]. With the simulation software the 3D USCT setup is constructed. The achieved datasets are compressed and reconstructed to get the images. The images are compared to the ideal reference image.

The acoustic parameters and the position of objects are set precisely in Wave3000 to construct an ideal reference image. Additionally, the objects with complex acoustic properties which are difficult to be obtained by real designs are simulated. The wave propagation in the 3D USCT is simulated by solving the wave equation with finite difference methods in Wave3000 [124, 45].

There was a strong limitation in this simulation, i.e. the simulated 3D USCT setup is about 10 % of the real USCT setup due to the limitation of the computing time and memory size. In the future

also the size of the simulated objects is scaled down to 10 % of a real breast (approx. 10cm ). For example, the simulation processes take approx. ten days and 40 days on one PC (Pentium 4, 3.2 GHz, 2.0 GB RAM) for the dataset with the center frequency of the coded excitation of 1MHz and 3MHz, respectively.

### 3.5.2.1 Imaged objects

**Geometry information** The characteristics and the geometry information of imaged objects for simulated datasets are introduced as follows:

1. **bloodbone:** The imaged object is used to simulate the breast tissues with micro-calc deposits [125]. In this experiment, a simplified structure of the object is modeled consisting of a blood cylinder and a bone sphere. Blood and bone with similar acoustic properties as breast tissue and micro-calc are adopted for the simulation. The diameter of the cylinder is approximately ten millimeters and the diameter of the bone ball is 0.2 mm.
2. **6fatRand:** The tissue in a breast is usually not evenly distributed. In order to test the influence of this property on the images of USCT, randomly distributed fat balls with different acoustic properties are designed in the datasets 6fatRand.

The imaged object has a cross section of a cylinder with a diameter of ten millimeters. Within the cylinder are six types of randomly distributed fat balls with a diameter of 0.2 mm each. These fat balls have the acoustic properties which are designed within the range similar to real fat material: [-5%, +5%] of the impedance of fat, i.e. 1.33 MRayL to simulate the natural divergence of tissues [43].

3. **6fatRand1bn:** Here a bone sphere with a diameter of 0.2 mm is placed in the center of the cylinder with a diameter of ten millimeters. This cylinder is filled by randomly distributed fat balls. The properties of the fat balls are similar to the simulated object 6fatRand.
4. **6fatXian:** The simulated object consists of six coaxial cylinders with increasing diameters and equal thickness. The maximum diameter is ten millimeters. Each cylinder is filled with one

type of fat balls in the object 6fatRand. In each cylinder the fat balls are homogeneous. The acoustic impedances of the fat vary with the different cylinders. The acoustic impedance increases linearly from inside to outside of the cylinders.

**Acoustic properties** The design of the simulated objects is based on the acoustic properties of real breasts. The breast tissues consist mainly of water, blood, fat, gland tissue, etc. Cancer has a smaller elastic modulus than gland tissue. The early stage of breast cancer is considered to be related to micro-calc in breast tissues, which is known to be calcium hydroxyapatite [126, 127]. Calcium is the most important material in bone tissue. Thus the calcium hydroxyapatite is simulated with the material bone in this work.

The parameters for acoustic properties of real breast tissues which consist of the materials water, blood, breast, fat, and bone, are listed in Table 3.2 [43].

Material	Temperature ° C	Attenuation (dB cm <sup>-1</sup> ) 1 MHz / 3 MHz
Water	30	1.7E-3 / 1.49E-2
Blood	37	9.07E-2 / 8.16E-1
Breast	37	2.25E-1 / 2.02
Fat,tissue	37	7.5E-1 / 6.75
Bone,skull human,infant	37	6.1 / 17

Table 3.2: Parameters of acoustic properties [43].

In order to simulate real breast tissue, the parameters in equation 2.6 for the materials bone, blood and water used in dataset bloodbone are listed in Table 3.3. The acoustic properties of water are influenced by the temperature. For dataset bloodbone the water temperature is 30° C.

The corresponding parameters for datasets 6fatRand, 6fatRand1bn and 6fatXian are listed in Table 3.4 and Table 3.5. Six types of fat balls are used in these three simulated datasets with different geometry distributions.

Parameter	Bone, skull human, infant cortical	Blood whole fresh	Water 30 ° C
$\rho$ (kg m <sup>-3</sup> )	1850	1055	1000
$\mu$ (Mpa)	3127	0	0
$\delta$ (MPa)	9306	2634	2280
$\eta$ (Pa*s)	37	2.0000E-1	2.300E-3
$\phi$ (Pa*s)	1E-1	1E-3	1.2420E-4
VL (m/s)	2901	1580	1510
$\alpha$ (dB/cm)	1.8777	1.1027E-1	1.5891E-3
$d(\alpha)/df$ (dB/cm/MHz)	3.7567	2.2067E-1	3.1800E-3
Wave length (mm) at 1 MHz	2.900	1.5801	1.5100

Table 3.3: Parameters in equation 2.6 for simulated dataset blood-bone. VL is the group velocity.

Parameter	Water 23 ° C	Fat balls type 1	Fat balls type 2	Fat balls type 3
$\rho$ (kg m <sup>-3</sup> )	1000	920	920	920
$\mu$ (Mpa)	0	0	0	0
$\delta$ (MPa)	2191	1738	1795	1861
$\eta$ (Pa*s)	2.5E-3	7E-2	7E-1	7E-1
$\phi$ (Pa*s)	1E-6	3.3E-1	3.3E-1	3.3E-1
$VL$ (m/s)	1480.2	1374.5	1396.8	1422.6
$\alpha$ (dB/cm)	1.76E-3	9.09E-1	8.66E-1	8.20E-1
$d(\alpha)/df$ (dB/cm/MHz)	3.50E-3	1.82	1.73	1.64
Wave length (mm) at 1 MHz	1.48	1.37	1.40	1.42

Table 3.4: Parameters in equation 2.6 for simulated datasets 6fatRand, 6fatRand1bn and 6fatXian. VL is the group velocity.

Parameter	Fat balls type 4	Fat balls type 5	Fat balls type 6	Bone, skull human, infant cortical
$\rho$ (kg m <sup>-3</sup> )	920	920	920	1850
$\mu$ (Mpa)	0	0	0	3127
$\delta$ (MPa)	1925	1990	2055	9306
$\eta$ (Pa*s)	7E-1	7E-1	7E-1	37
$\phi$ (Pa*s)	3.3E-1	3.3E-1	3.3E-1	1.0E-1
$VL$ (m/s)	1446.5	1470.7	1494.6	2901
$\alpha$ (dB/cm)	7.799E-1	7.420E-1	7.070E-1	1.8777
$d(\alpha)/df$ (dB/cm/MHz)	1.56067	1.4847	1.4150	3.7567
Wave length (mm) at 1 MHz	1.45	1.47	1.49	2.90

Table 3.5: Parameters in equation 2.6 for simulated datasets 6fatRand, 6fatRand1bn and 6fatXian. VL is the group velocity.

### 3.5.2.2 Design of an ideal reference

The design of an ideal reference for simulated datasets is based on the geometry and acoustic properties of the imaged objects. The constructed reference images have an identical resolution as the reconstructed images in order to compare the reference and reconstructed images pixel by pixel. With the geometry information of the object, the contours of objects in reference images are drawn by the Bresenham algorithm [128]. The gray values of these contours are derived from the reflectivity coefficient of objects, the first order derivative of the acoustic impedances of media. The achieved gray values of object contours are then normalized in the reference image.

The reference images and their profiles for the simulated datasets bloodbone, 6fatRand, 6fatRand1bn and 6fatXian are plotted in Fig. 3.6, Fig. 3.7, Fig. 3.8 and Fig. 3.9, respectively.

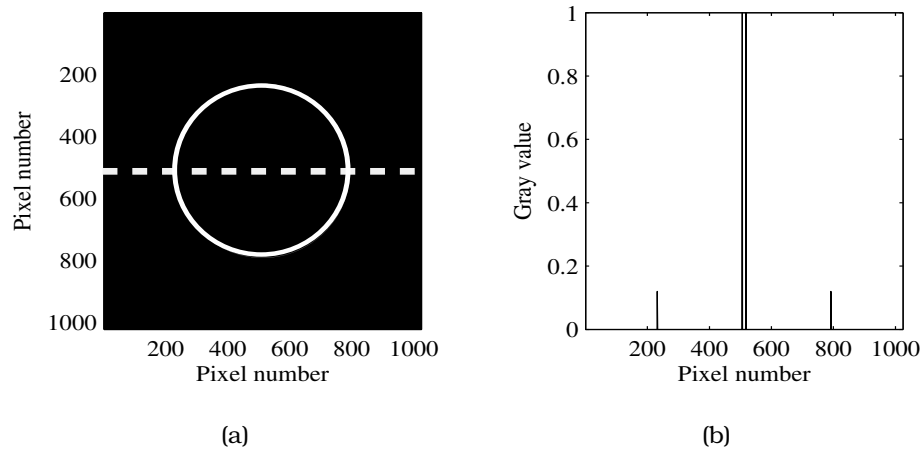


Figure 3.6: Simulated dataset bloodbone, (a) reference image, (b) profile of reference image at position shown with the dashed line. For demonstration the border of the blood cylinder is enhanced in the reference image.

In the Fig. 3.6 the contour of the blood cylinder with a circular shape is visible. The peak in the center of the profile image corresponds to the bone sphere which has a high gray value in the reference image due to the significantly higher acoustic impedance than that of the blood cylinder. The gray values in the reference image are normalized with the maximum value.

In the dataset 6fatRand the random distribution of the fat balls can be seen in the profile image Fig. 3.7. The border between the fat and water areas is imaged with high gray values due to high impedance differences between them.

In the reference image for dataset 6fatRand1bn the gray values of the fat balls are significantly smaller than the values of the bone sphere due to the high acoustic impedance of the bone, see Fig. 3.8. The high contrast of the reference image is shown in the profile image.

In the reference image for the dataset 6fatXian in Fig. 3.9(a) the gray values of the borders between different fat areas are identical. The identical gray values are due to the linear increasing acoustic impedances of the fat materials. The gray value of the border be-

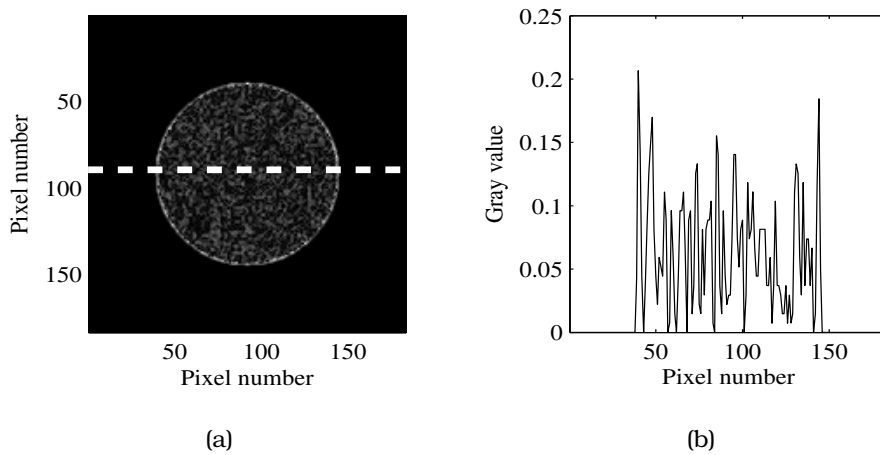


Figure 3.7: Simulated dataset 6fatRand, (a) reference image, (b) profile of reference image at position shown with the dashed line.

tween the water and fat areas is higher than that between the fat areas, see Fig. 3.9(b).

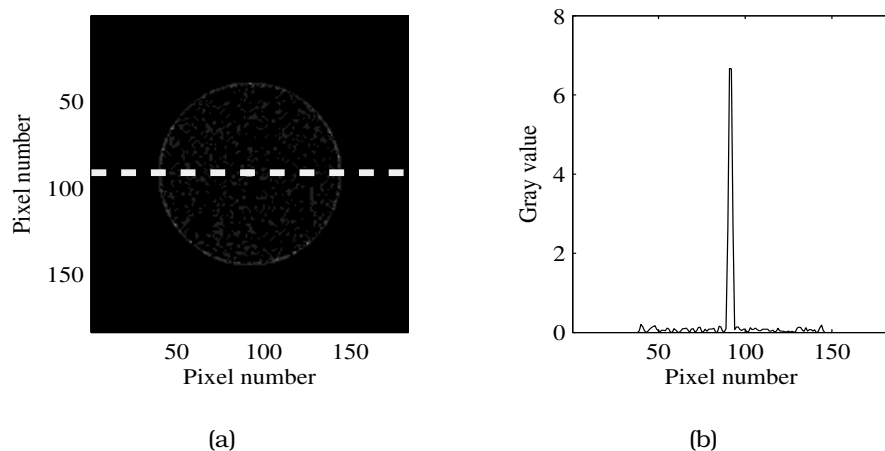


Figure 3.8: Simulated dataset 6fatRand1bn, (a) reference image, (b) profile of reference image at position shown with the dashed line.

### 3.5.2.3 Simulated USCT datasets

**Coded excitation** The pulse shape and the center frequency of the coded excitation for simulated datasets replicate the chosen value in the real 3D USCT setup. The center frequency and bandwidth are 3 MHz and 2 MHz, respectively. The shape of used coded excitation is plotted in fig. 3.10 with a sampling frequency of 50 MHz.

**Simulation process** The computing time for simulation of one dataset of used 3D USCT setup depends on the size of imaged objects, the difference between acoustic impedances of the different materials, the center frequency of the coded excitation and the number of A-scans. If the imaged object is modeled with a large number of grids, the computing time increases for solving the wave equations with the finite difference method in Wave3000, considerably [124].

**Image reconstruction** The simulated datasets of A-scans are used to reconstruct the images. The parameters for reconstruction of images are listed in Table 3.6. The dataset bloodbone uses a coded excitation with a smaller center frequency (1 MHz) than that of other datasets (3 MHz) to save the time of simulation process. The time of the simulation process for the dataset bloodbone is about one week

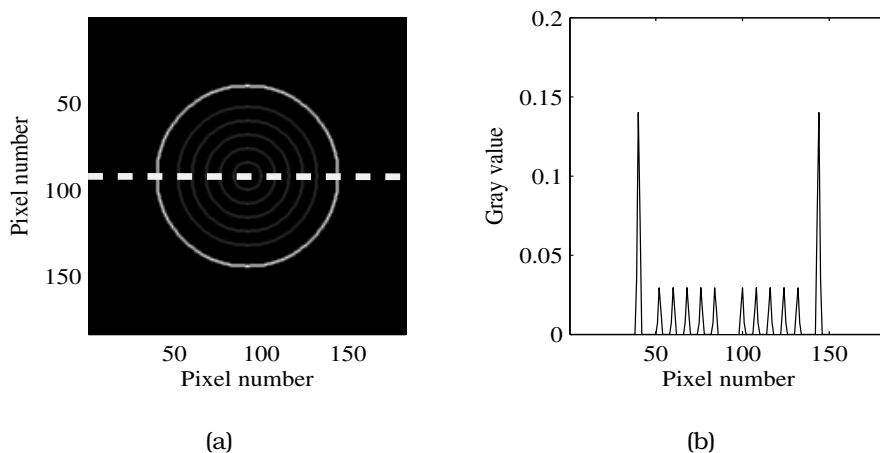


Figure 3.9: Simulated dataset 6fatXian, (a) reference image, (b) profile of reference image at position shown with the dashed line.

and for other datasets is about 40 days.

Dataset name	Image size (mm)	Number of pixels per edge	Emitter/receiver layer	Center frequency (MHz)
bloodbone	18	1024	1/2	1
6fatRand	18	183	1/2	3
6fatRand1bn	18	183	1/2	3
6fatXian	18	183	1/2	3

Table 3.6: Parameters for reconstruction of simulated datasets.

The reconstructed images with the simulated datasets bloodbone, 6fatRand, 6fatRand1bn, 6fatXian are plotted in Fig. 3.11(a), Fig. 3.11(b), Fig. 3.11(c) and Fig. 3.11(d), respectively. In the reconstructed image for dataset bloodbone in Fig. 3.11(a) the bone sphere and the blood cylinder are surrounded by high light circles due to their high sound impedance relative to that of water. The randomly distributed fat balls have higher contrast in Fig. 3.11(b) for dataset 6fatRand than in Fig. 3.11(c) for dataset 6fatRand1bn. The coaxial circles in Fig. 3.11(d) are corresponding to the six coaxial cylinders in dataset 6fatXian.

The maxima of gray values in the reconstructed images are very

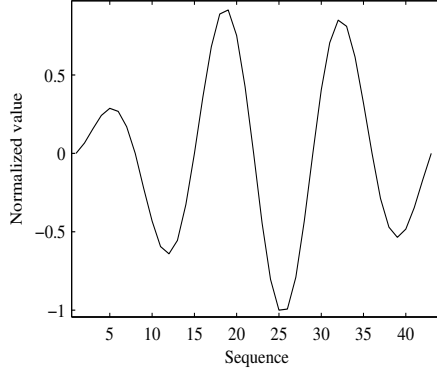
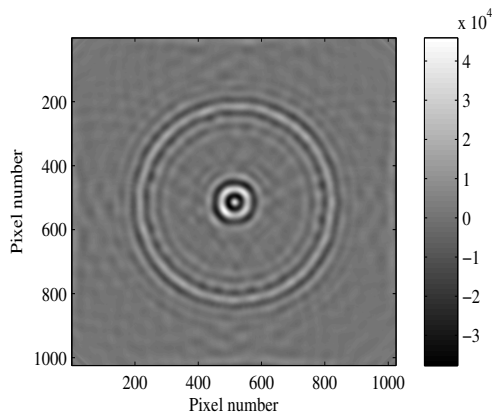


Figure 3.10: Coded excitation for simulated datasets with sampling frequency of 50 MHz and the center frequency of 3 MHz. The Gaussian envelope of the coded excitation has a bandwidth of 2 MHz.

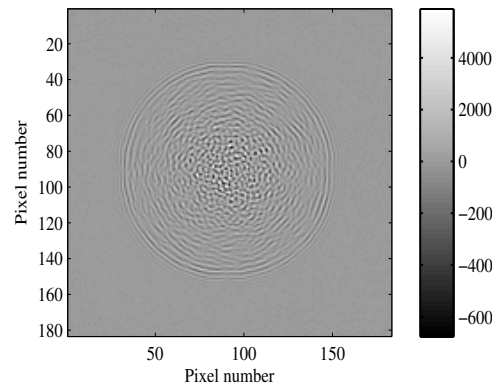
different. The amplitude of scattered ultrasound pulses, which is related to the gray value of images, is decided by the difference of acoustic impedance within imaged objects. The difference of acoustic impedance between bone and blood is much larger than that between fat and water, thus the corresponding gray values are very different in the reconstructed images.

#### **3.5.2.4 Evaluation process**

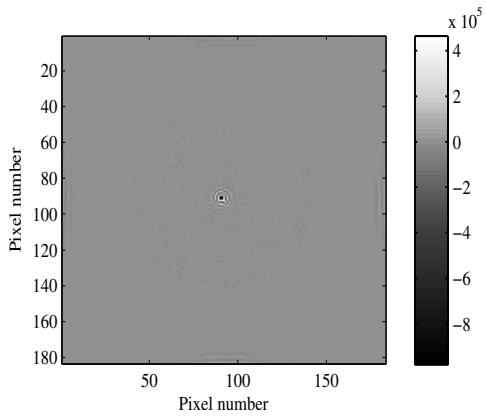
The design of the object geometry can be validated directly by using the visualization program in Wave3000. The different acoustic properties of materials in the designed objects are represented with different colors correspondingly. The positions of the areas with the same color are used to evaluate the geometry of the objects.



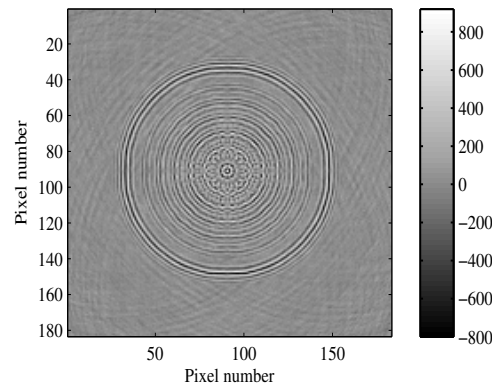
(a)



(b)



(c)



(d)

Figure 3.11: Reconstructed image for simulated dataset bloodbone [a], 6fatRand [b], 6fatRand1bn [c] and 6fatXian [d].

# Chapter 4

## Results

In parallel to the sequence of previous chapters the experimental results are shown in this chapter step by step. The properties of A-scans are analyzed in chapter 2, therefore the compression results for A-scans are evaluated at first. Then the results for image quality based evaluation methods are explained with objective and subjective scores. Finally these dataset based results are used to show the denoising ability of compression methods.

### 4.1 Evaluation of data compression by comparing A-scans

A-scans with or without noise are tested in experiments. The original and the compressed A-scans are compared by PSNR, which has the advantage to show the sample difference of A-scans.

#### 4.1.1 Compression of synthetic A-scans without noise

The adapted lossy compression methods (in section 2.5) are evaluated with the synthetic A-scan without noise (see Fig. 4.1). This synthetic A-scans are based on the model of A-scans introduced in section 2.3.3 and used as the reference, i.e. original A-scan, for evaluation of compressed A-scans. The A-scan consists of only one ultrasound pulse, which has a similar shape as the coded excitation. The ultrasound pulse extends to three wavelengths with a Gaussian envelope. The center and sampling frequency of the ultrasound pulse are 3 MHz and 10 MHz, respectively. Its bandwidth is 2 MHz.

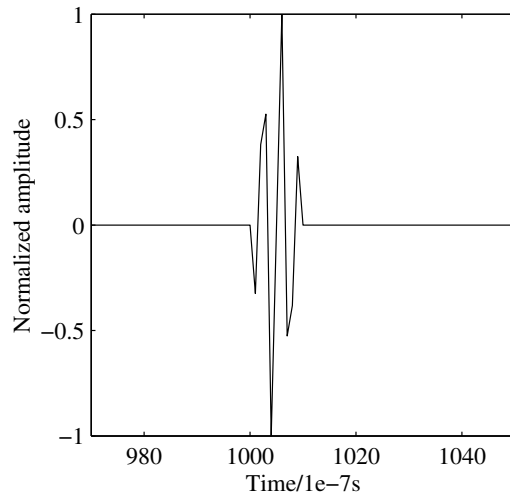


Figure 4.1: Artificial reference signal.

With changed values of threshold the achieved compression ratios for each A-scan are calculated. The compressed A-scans are compared with original A-scans.

The PSNR values are calculated to score compressed A-scans with different compression methods at different compression ratios. These scores are plotted as dots in Fig. 4.2. The reason to use an A-scan without noise is to test the influence of compression on the pulse shape of ultrasound signals. The value of threshold is relative to the maximum value of the ultrasound pulse and increasing linearly. The compression ratios increase monotonously but not linearly with the increasing threshold values.

The main tendency of PSNR for compression methods Threshold, MultiFractal and DWT is decreasing due to the increasing difference between the original and the compressed A-scans.

In Fig. 4.2 it can be observed that a different number of dots has been calculated for different compression methods. For the result of IKstd in Fig. 4.2(f) only one compression ratio, i.e. the maximum compression ratio, is achieved with used parameters of IKstd. There are many samples with zero value in the original A-scan. Only few

samples are detected with IKstd, therefore a high compression ratio is achieved.

For spiking deconvolution the A-scan convoluted with a deconvolution filter has its maximum at the beginning of the ultrasound pulse. At the compression ratio 500 only this maximum survive the convolution. This maximum is convoluted with coded excitation to create the decompressed A-scan. Therefore the decompressed A-scan at a compression ratio 500 has a similar pulse shape as the original ultrasound pulse and the value of PSNR is significant larger than that of other methods.

The dashed line in Fig. 4.2(e) for IK is not connected between the compression ratio 819 and the maximum compression ratio. The reason is that the PSNR has the infinite large value for the decompressed A-scan with the compression ratio between this range. This case happens when the decompressed A-scan is identical to the original A-scan.

#### **4.1.2 Compression of noisy A-scans**

The noise in original USCT A-scans has been reduced by an analog and averaging filter, as discussed in section 2.2.2. The realistic range of noise in an A-scan depends on the experimental environment and the used USCT setup. As example a real dataset with the A-scans from emitter position 0 and receiver positions 72, 73, 84, 85, 96, 97, 108, 109, 120, 121 are used to test the noise level. The samples before the transmission signal in A-scans are considered to be related to noise. The noise level is defined as the derivation of these sample values. Results for these selected A-scans show that the realistic values of noise level are smaller than 200 if the maximum value of samples in datasets is 65535 (16 bits), i.e. the noise level is maller than 0.3 %.

In a real dataset the signal to noise ratio (SNR) is defined as a constant for all A-scans. The maxima of different A-scans may be different in a dataset. Therefore the relative values between SNR to the maxima of different A-scans vary significantly in a dataset, i.e. the relationship between noise and the maximum of ultrasound pulse varies with the selected A-scan. This relationship may influence the performance of compression methods. Thus the noise level is simulated with a large range of grades for validating the denoising ability

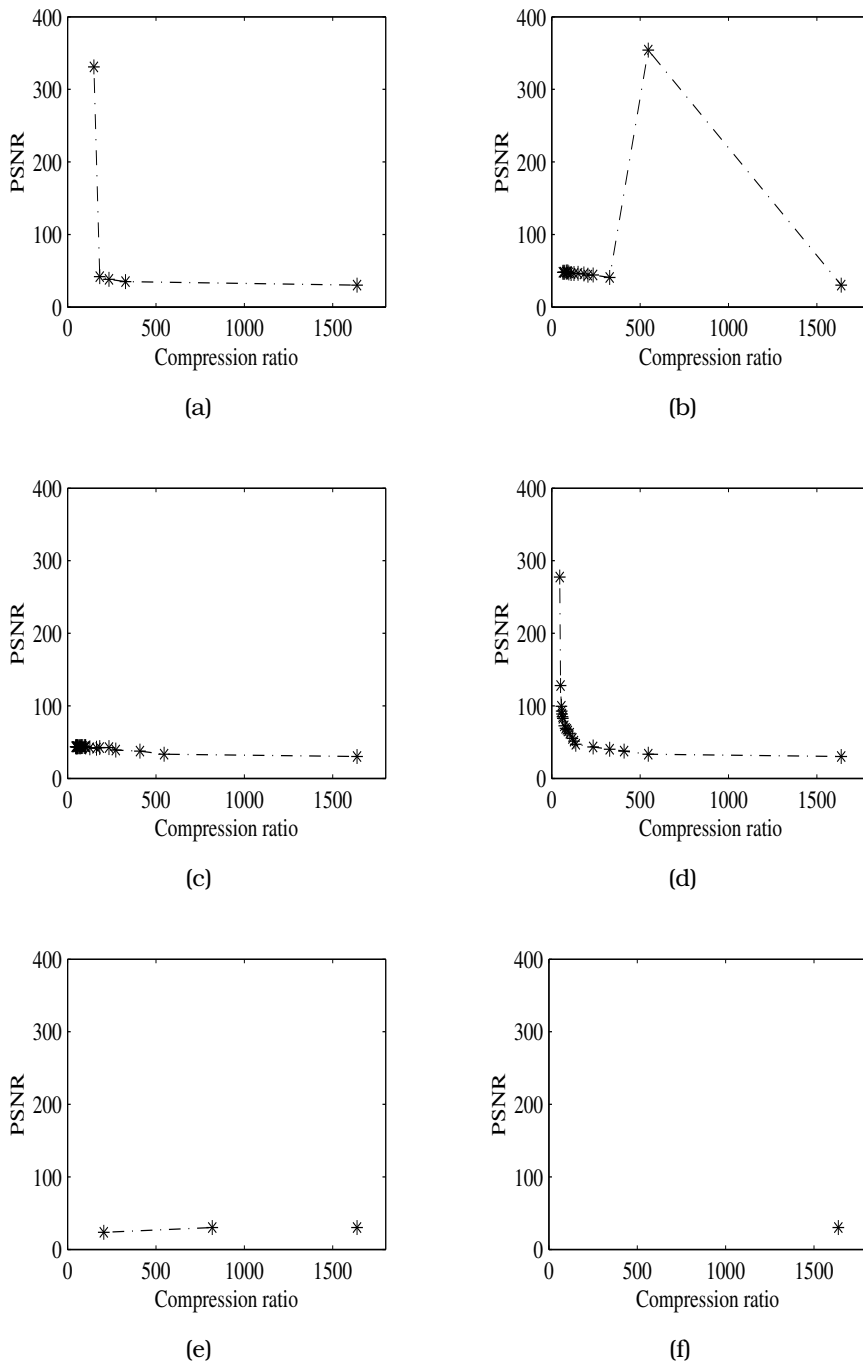


Figure 4.2: Evaluation of compression methods with PSNR (a) Threshold, (b) DCV, (c) MultiFractal, (d) DWT, (e) IK and (f) IKstd for synthetic A-scans without noise.

of compression methods.

The original A-scan in Fig. 4.3(a) is added with noise at different grades to make the noisy A-scans. The original A-scan is identical to the synthetic A-scan in Fig. 4.1. The noisy A-scans in Fig. 4.3(b), Fig. 4.3(c) and Fig. 4.3(d) are created by adding normal distributed random numbers as noise with standard deviations of -34 dB, -20 dB and -14 dB of the maximum value of the reference A-scan.

These noisy A-scans are filtered and then compressed to analyze the denoising ability of the compression method relative to that of a filter. The designed filter is a band pass 6th order Butterworth filter. The significant advantage of Butterworth filter is the maximally flat magnitude response in the pass band [129, 130].

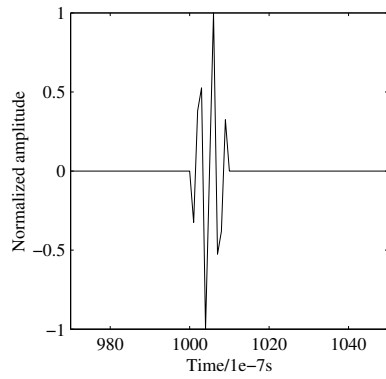
The frequency response of the implemented Butterworth filter is shown in Fig. 4.4. The phase and frequency relationship is not linear. Therefore the pulse shape may be changed after being processed with this filter.

The compression results with the noisy A-scans are scored with the PSNR. The scores are shown as an example in Fig. 4.5 for Fig. 4.3(c).

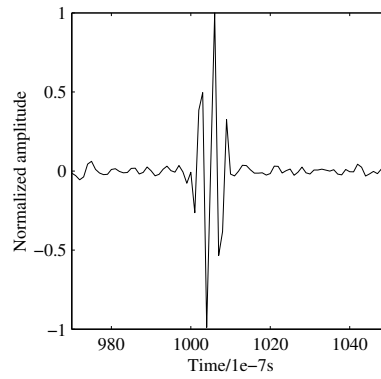
The denoising abilities of these compression methods are analyzed with achieved PSNR values. The increasing tendency can be seen in Fig. 4.5(d) at small compression ratios. For comparison Fig. 4.2(d) has only decreasing values of PSNR. Similar results can be found in Fig. 4.2(a) and 4.5(a). At small compression ratios the noise is reduced with increasing threshold values and PSNR increases with reduced noise.

With further increasing threshold not only the noise but also parts of the ultrasound signal are removed. Therefore the decrease of PSNR can be seen at compression ratios larger than 500.

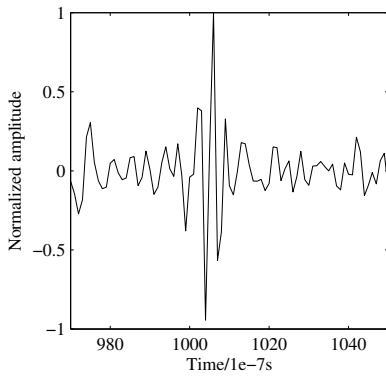
The maximum of PSNR at the compression ratio 500 is similar to the noiseless case in Fig. 4.2(b) due to the simple structure of designed A-scan which has only one ultrasound pulse. At this compression ratio the information of the ultrasound pulse is kept in the compressed A-scan and the noise is reduced mostly.



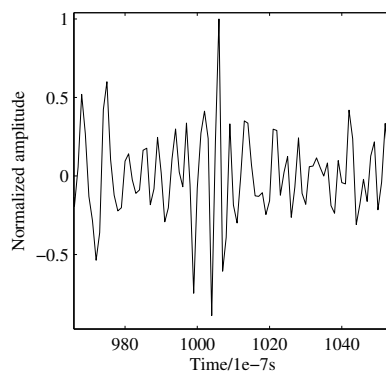
(a)



(b)



(c)



(d)

Figure 4.3: Artificial reference signal (a) and noisy signals which are designed by adding the normally distributed random noise with standard deviations (b) -34 dB, (c) -20 dB and (d) -14 dB of the maximum value of the reference A-scan.

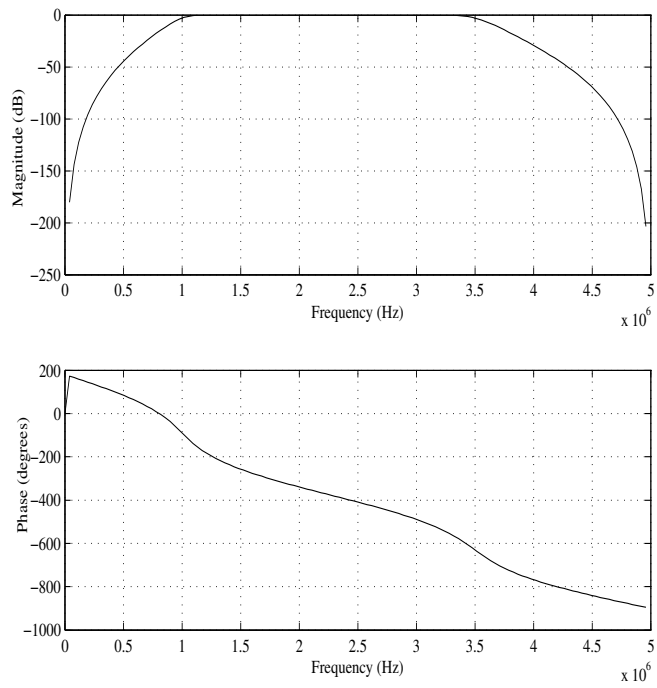


Figure 4.4: The magnitude and phase dependently on frequency of used filter for synthetic A-scans.

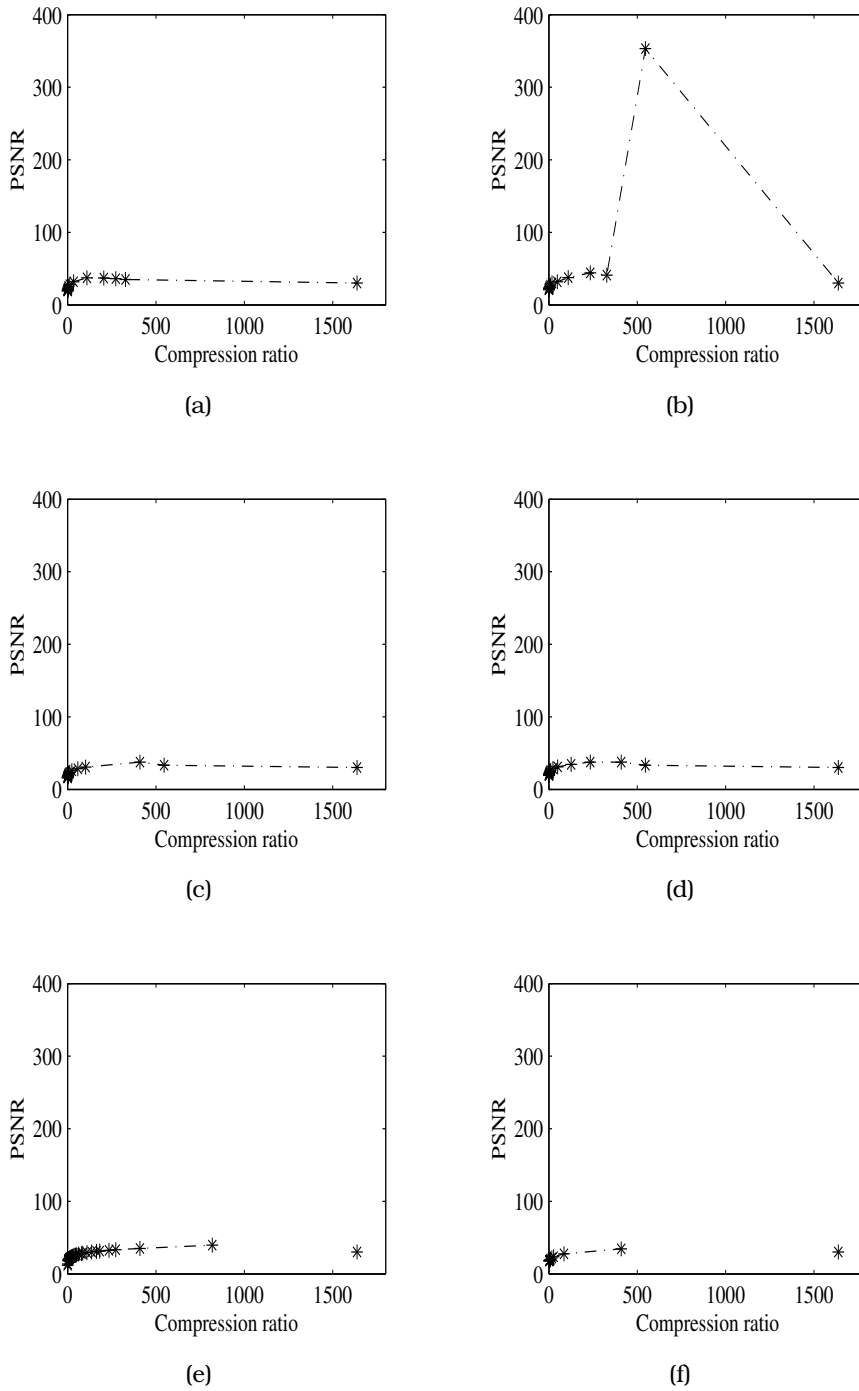


Figure 4.5: Evaluation of compression methods with PSNR(a) Threshold, (b) DCV, (c) MultiFractal, (d) DWT, (e) IK and (f) IKstd for synthetic A-scans adding the normally distributed random noise with standard deviation  $-20$  dB of the maximum value of the reference A-scan.

## **4.2 Evaluation of data compression by comparing images**

Comparison of images is the approach which human perception or doctors would perform, therefore now the comparison of simulated or real imaged datasets with their compressed counterparts is performed to give a visual impression of the effect of data compression. Furthermore It is shown how the selected estimators interpret the compression.

### **4.2.1 Simulated datasets**

The design of the simulated datasets was introduced in section 3.5.2.3. The designed ideal reference images with the available information of the imaged objects are employed to evaluate the compressed datasets with the standard estimators introduced in section 3.4.1, the optical flow based estimator in section 3.4.2 and CMM in section 3.4.3. At the end of this section, the images of compressed datasets are scored with the original image as reference.

#### **4.2.1.1 Compressed datasets**

The adapted lossy compression methods introduced in section 2.5 are applied to the simulated datasets. The compression ratio for a dataset is the mean value of compression ratios for all A-scans belonging to the dataset. With the changed values of the corresponding parameter, e.g. threshold value, compression ratios can be adjusted.

For each dataset more than 20 linear distributed values of the threshold values are selected at the range from 0 to 100 % of the maximum possible value of the A-scans. Thus the dataset is compressed at 20 different compression ratios with an increasing tendency. The compressed datasets are reconstructed.

The image for simulated dataset bloodbone compressed at the compression ratios 10, 20 and 60 are displayed in Fig. 4.6-4.12. At low compression ratios ( $< 20$ ) the images with DWT, IK, IKstd and MultiFractal show clearer contours of the imaged objects than that with Threshold, DCV and DCT.

All compression results in Fig. 4.8 show low image quality in contrast to the other compression methods. DCV shows in comparison to all other used compression methods a low image quality. That gets still more pronounce if the comparison of the image quality at the same compression ratio 10 is carried out as to be seen in Fig. 4.13 for dataset 6fatRand.

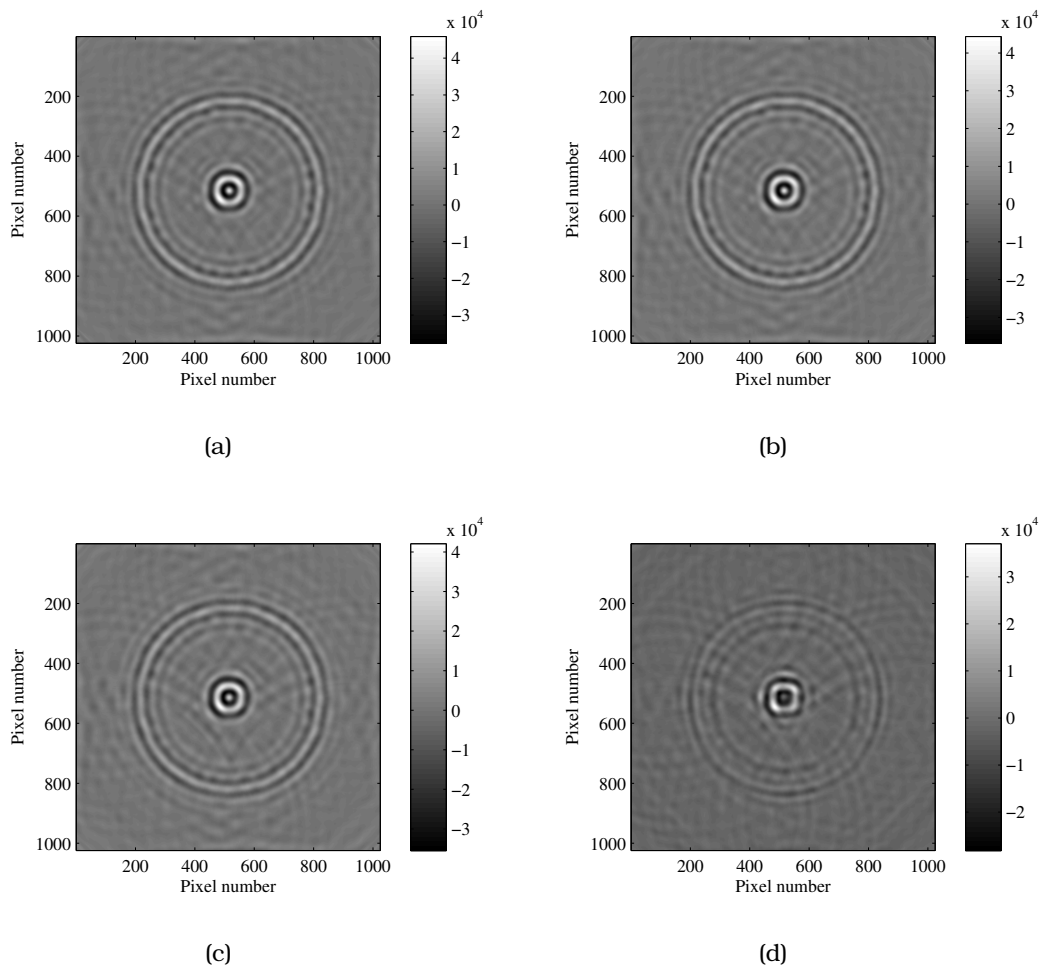
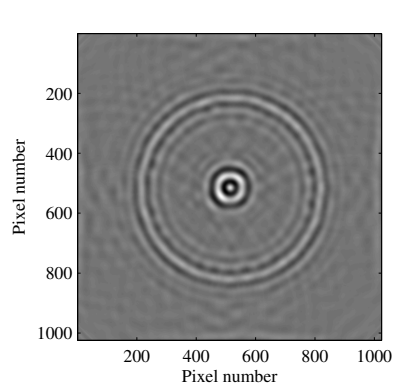
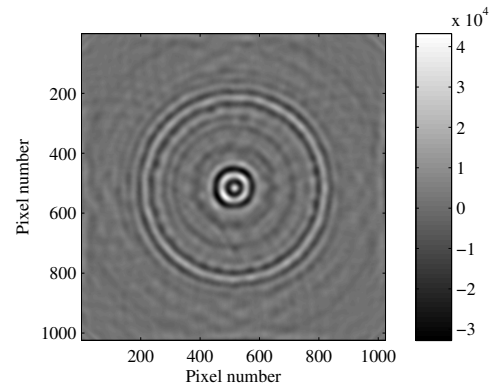


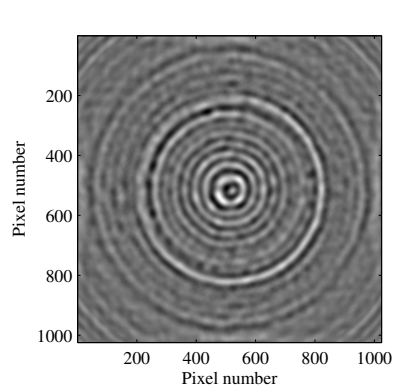
Figure 4.6: Original image for simulated dataset bloodbone (a) and the same slice of image for compression with DWT at the compression ratios of (b) 10, (c) 20, and (d) 60.



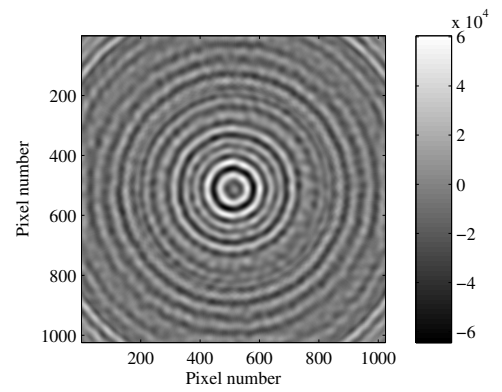
(a)



(b)



(c)



(d)

Figure 4.7: Original image for simulated dataset bloodbone (a) and the same slice of image for compression with DCT at the compression ratios of (b) 10, (c) 20, and (d) 60.

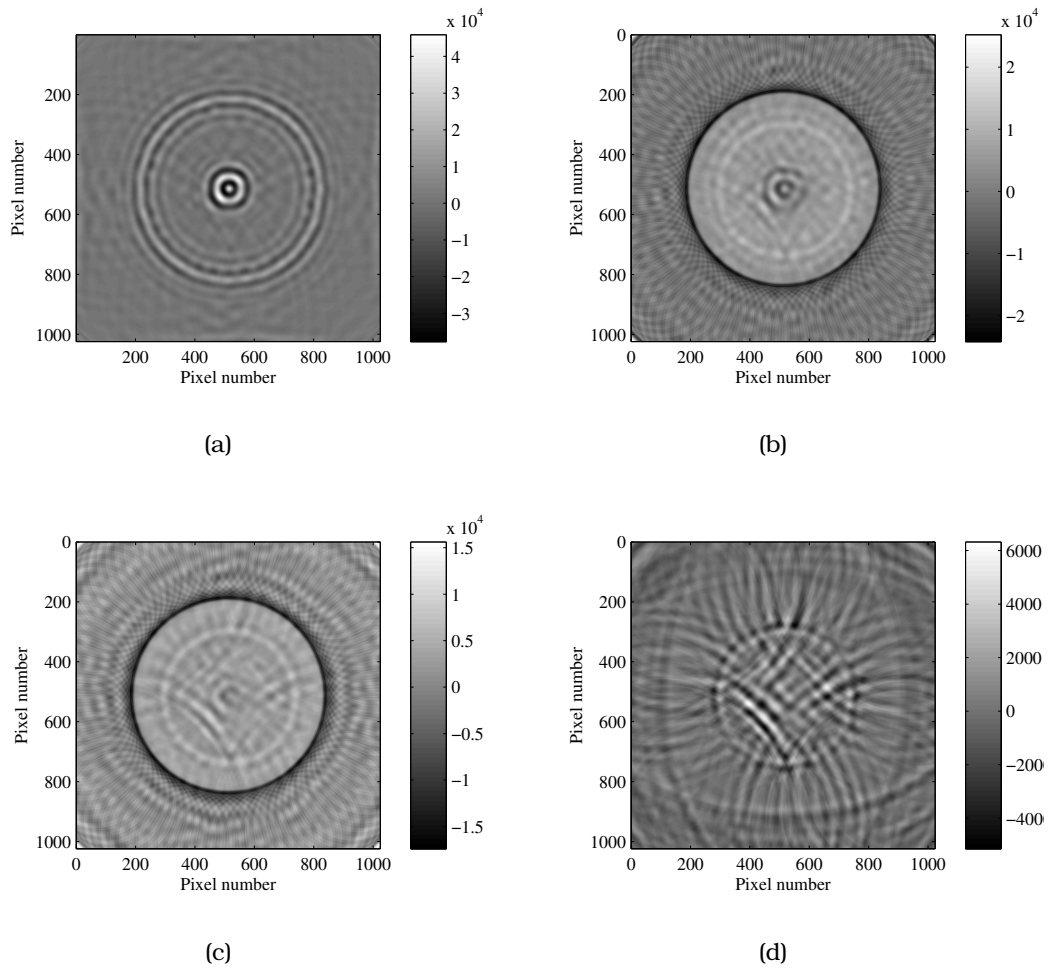
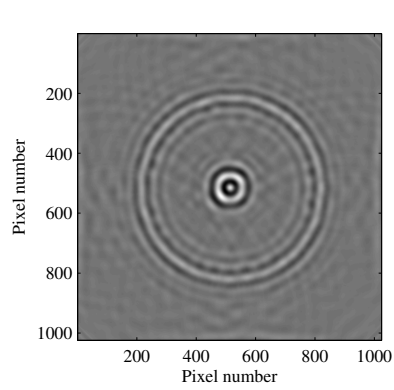
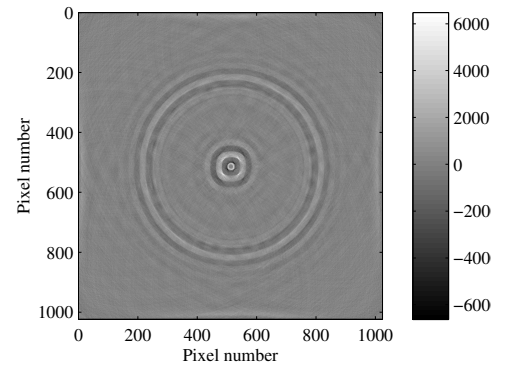


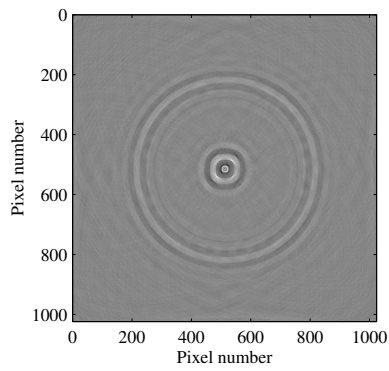
Figure 4.8: Original image for simulated dataset bloodbone (a) and the same slice of image for compression with DCV at the compression ratios of (b) 10, (c) 20, and (d) 60.



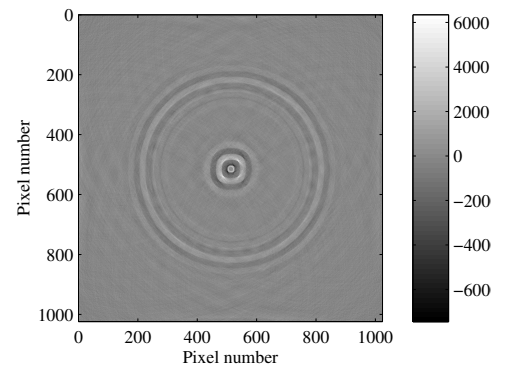
(a)



(b)



(c)



(d)

Figure 4.9: Original image for simulated dataset bloodbone (a) and the same slice of image for compression with IK at the compression ratios of (b) 10, (c) 20, and (d) 60.

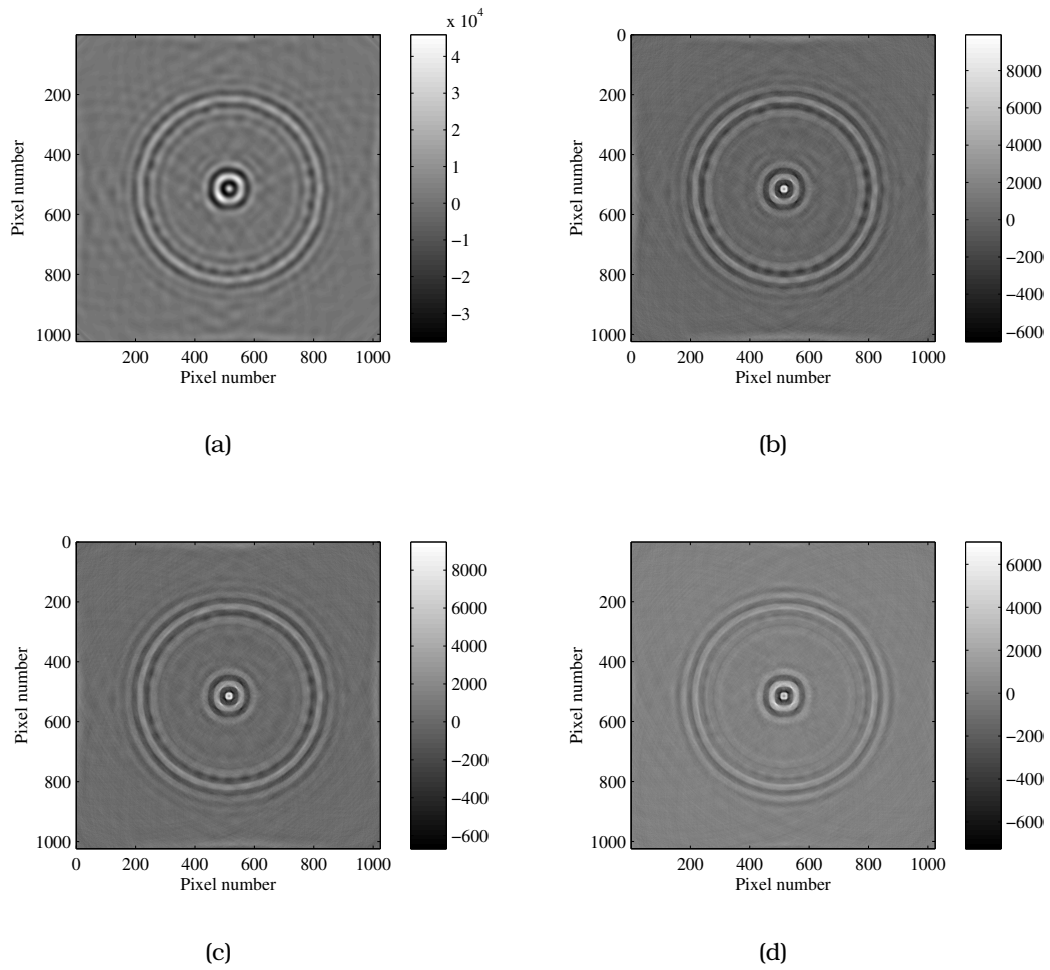


Figure 4.10: Original image for simulated dataset bloodbone (a) and the same slice of image for compression with IKstd at the compression ratios of (b) 10, (c) 20, and (d) 60.

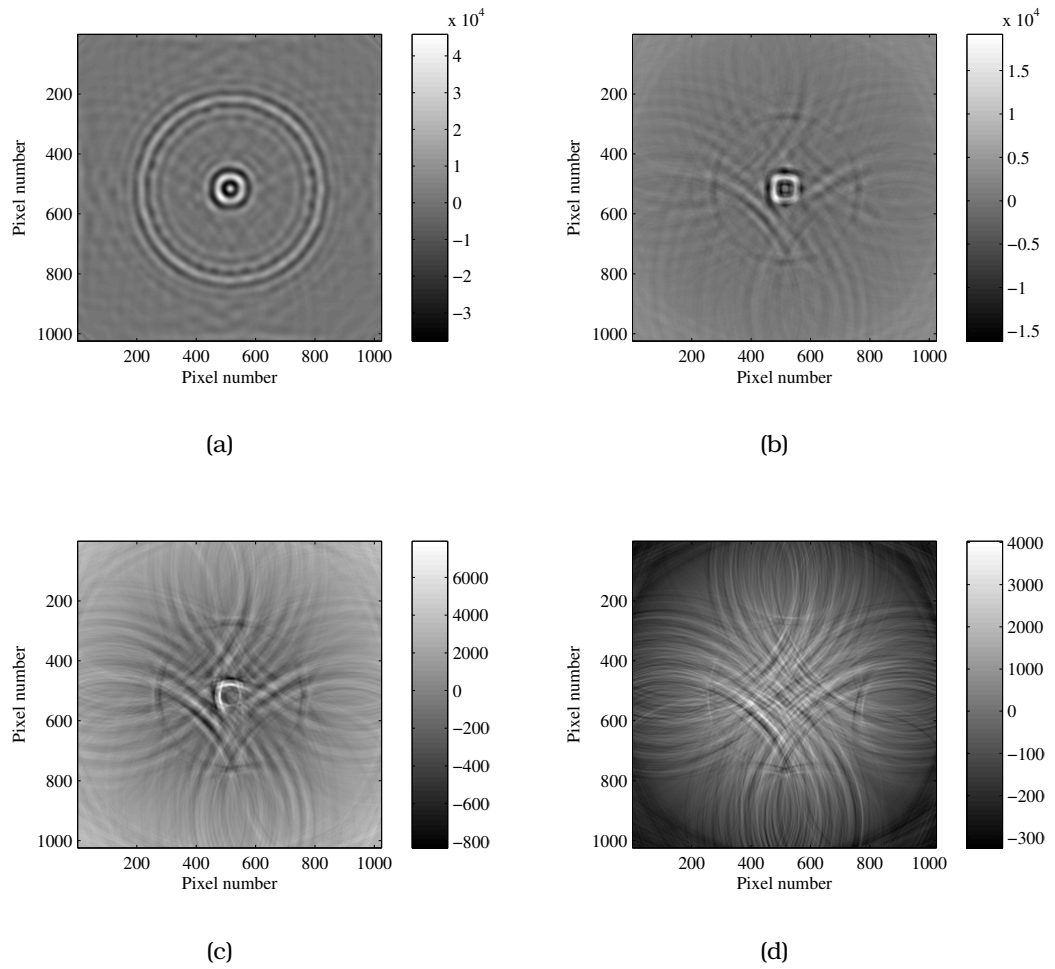
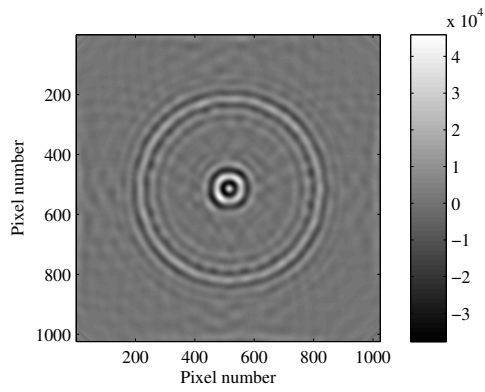
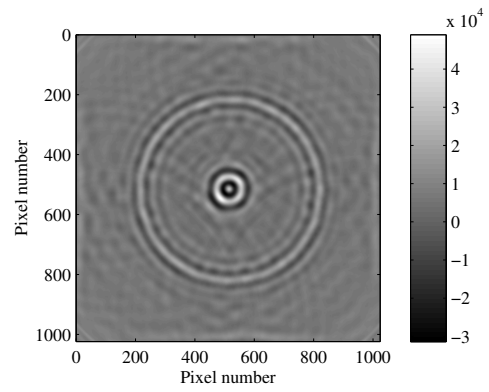


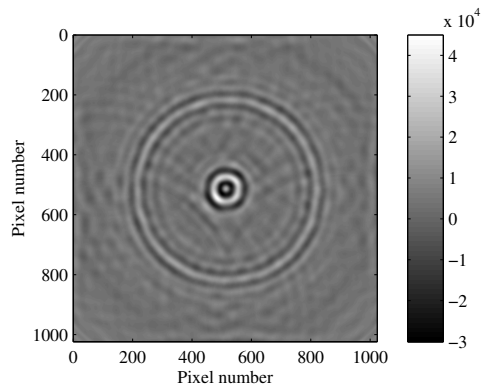
Figure 4.11: Original image for simulated dataset bloodbone (a) and the same slice of image for compression with Threshold at the compression ratios of (b) 10, (c) 20, and (d) 60.



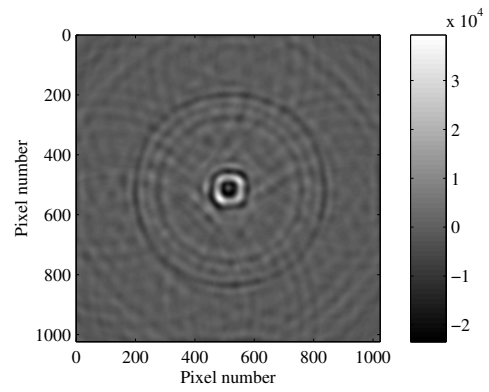
(a)



(b)

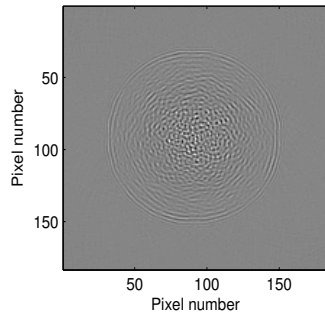


(c)

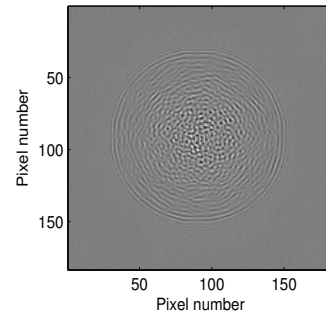


(d)

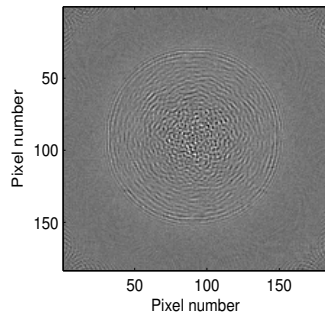
Figure 4.12: Original image for simulated dataset bloodbone (a) and the same slice of image for compression with MultiFractal at the compression ratios of (b) 10, (c) 20, and (d) 60.



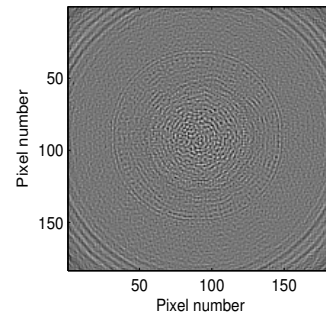
(a)



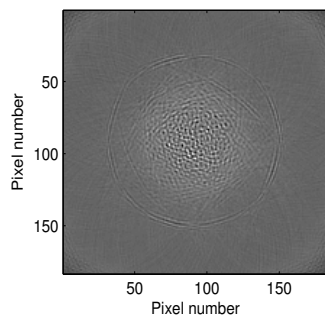
(b)



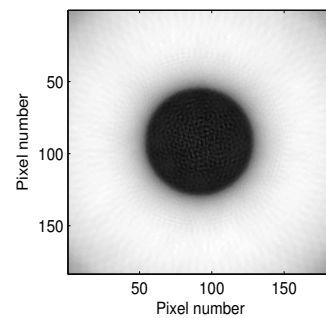
(c)



(d)



(e)



(f)

Figure 4.13: Images for the simulated dataset 6fatRand compressed with (a) DWT, (b) MultiFractal, (c) IKstd, (d) DCT, (e) Threshold and (f) DCV at a compression ratio of 10.

The images for the simulated dataset 6fatRand with different compression methods at a compression ratio 10 and 20 are shown in Fig. 4.13 and Fig. 4.14. The images compressed with DWT, IKstd and MultiFractal have higher quality than that with Threshold, DCT and DCV.

At compression ratio 20 or larger the reconstructed images have low quality. The contour of imaged objects is more degraded at high compression ratios than at low compression ratios, especially the reconstructed object is strongly degraded.

Due to human perception the images for the simulated dataset 6fatRand have relative high quality with DWT, IKstd and MultiFractal for compression ratios smaller than 20 compared to other methods. But the differences between these images are not significant. In order to compare the quality of these images objective image quality scores are tested.

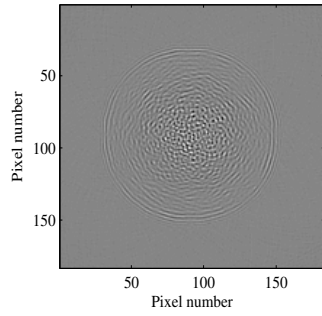
#### **4.2.1.2 Scores of standard estimators**

The images for compressed dataset bloodbone are scored with AMI by using the ideal reference shown in Fig. 3.6(a). The scores are shown in Fig. 4.15.

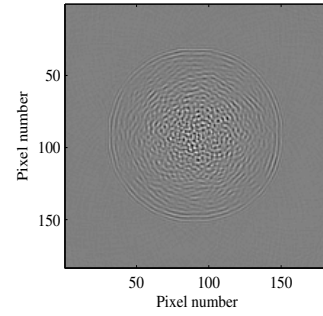
The main tendency of the AMI values decreases with increasing compression ratios. In the range of compression ratios from 0 to 30, IKstd, Wavelet, MultiFractal, and IK methods have larger AMI values than Threshold and DCV methods. DCT has a relative large AMI at low compression ratios, i.e.  $< 20$ . At high compression ratios, the AMI curve fluctuates for images of datasets compressed with DCT method. In either case compression ratios beyond 20 give to human perception irregular results.

At small thresholds run length encoding delivers only low compression ratios. The low compression ratios, which are smaller than one, are coming from the low performance of the run length encoding method for the compressed datasets with low threshold values. In this case the compression ratio should be set automatically to one, since there is no compression for datasets.

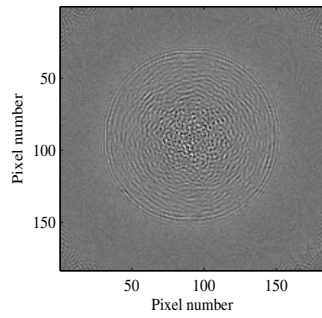
The standard image quality estimators introduced in section 3.4.1 are now compared to different simulated datasets. The scores for



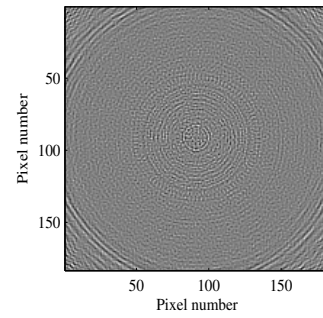
(a)



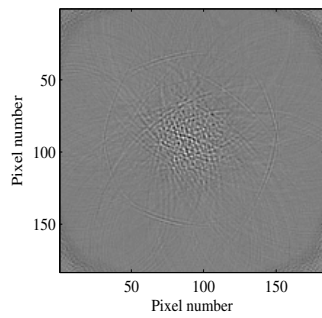
(b)



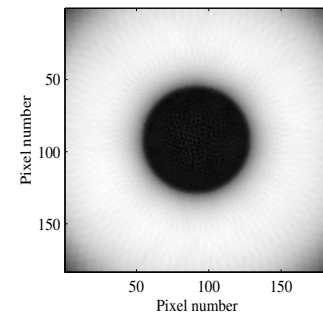
(c)



(d)



(e)



(f)

Figure 4.14: Images for the simulated dataset 6fatRand compressed with (a) DWT, (b) MultiFractal, (c) IKstd, (d) DCT, (e) Threshold and (f) DCV at a compression ratio of 20.

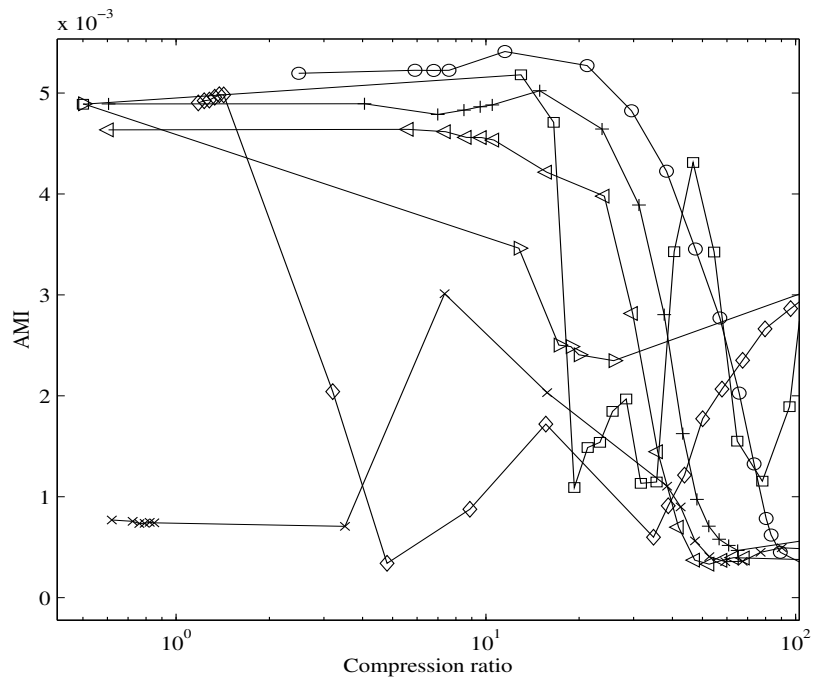


Figure 4.15: Scores obtained with AMI for dataset bloodbone compressed with DWT (+), MultiFractal (<-<), IK (<->), IKstd (o), DCV (x), DCT (square) and Threshold (diamond).

compression of dataset 6fatRand with different compression methods and compression ratios are shown in Fig. 4.16-Fig. 4.22. The reference is the ideal reference image designed in section 3.5.2.2.

6fatRand was used instead of bloodbone for the comparison of standard estimators, because 6fatRand is acoustically more similar to breast tissue than bloodbone. Breast tissues are not homogenous.

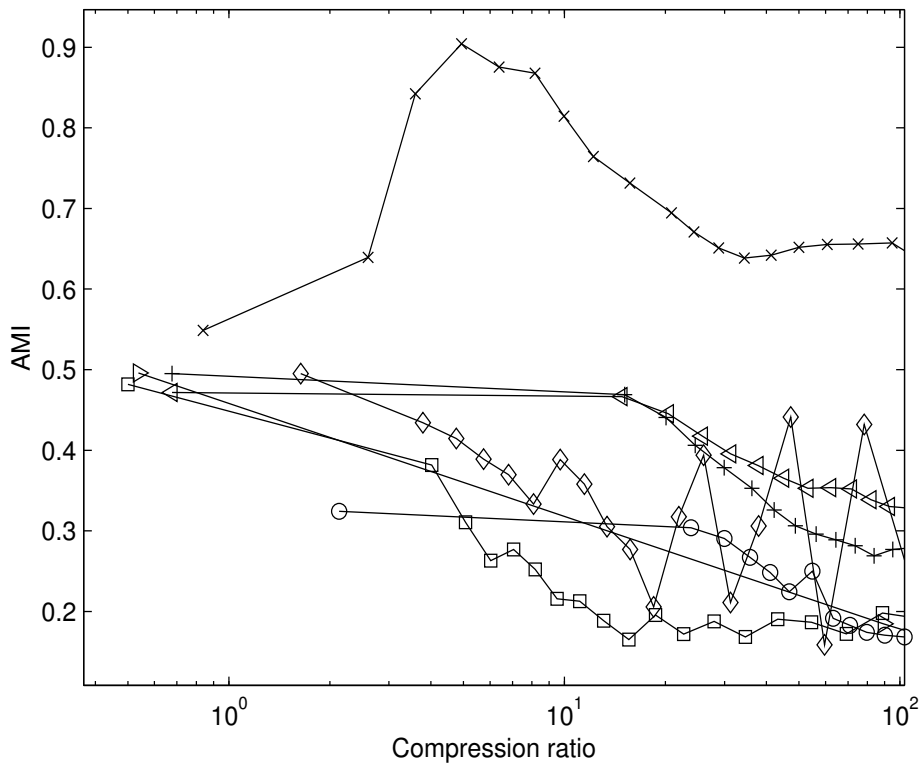


Figure 4.16: Scores obtained with AMI for dataset 6fatRand compressed with DWT (-+), MultiFractal (-<), IK (->), IKstd (-o), DCV (-x), DCT (-□) and Threshold (-◇).

The scores resulting from standard image quality estimators (see Fig. 4.16-4.23) are not very similar to the results obtained in section 4.2.1.1. According to the analysis images for compressed dataset 6fatRand with DCV have lower quality than that with other methods. However these images have higher scores with AMI, GVFMI and NMI. The scores of AMI are analyzed as follows.

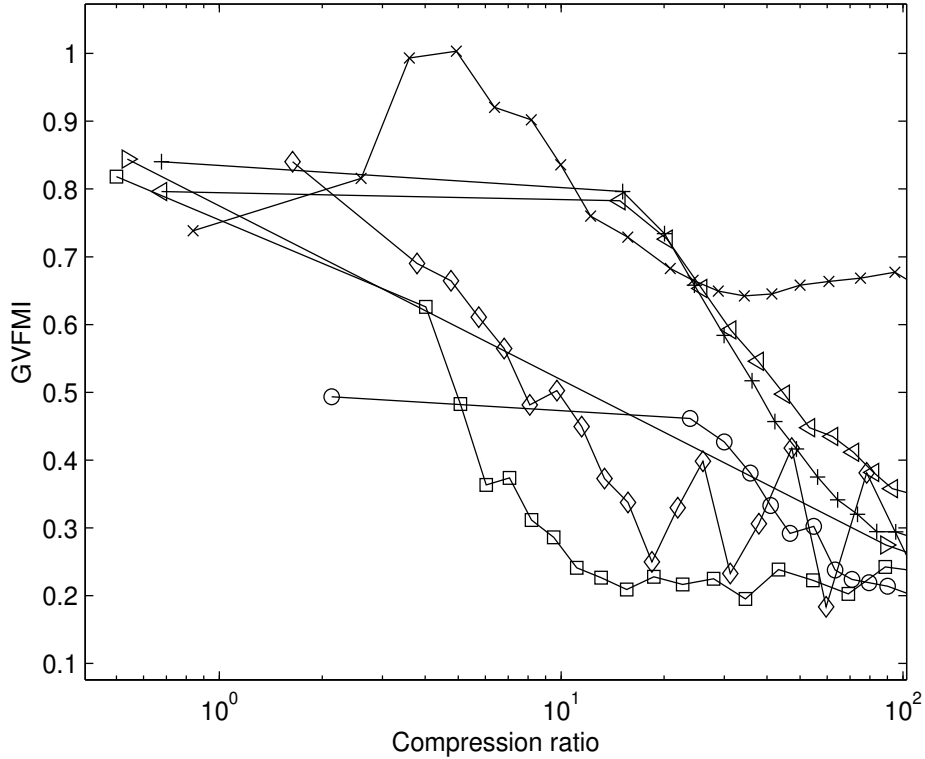


Figure 4.17: Scores obtained with GVFM I for dataset 6fatRand compressed with DWT (-+), MultiFractal (-<), IK (->), IKstd (-o), DCV (-x), DCT (-□) and Threshold (-◇).

The high scores of AMI after compression with DCV are based on the characteristics of the image distortions. The regions of similar tissues have similar gray values in the original image. The gray values of these regions may have different values in images of compressed datasets. However the distributions of these regions in the original and of compressed datasets are assumed to be similar. Based on this assumption the AMI has a high performance for evaluation of image quality [92, 94]. Obviously the AMI is unsuitable for the corresponding image distortions.

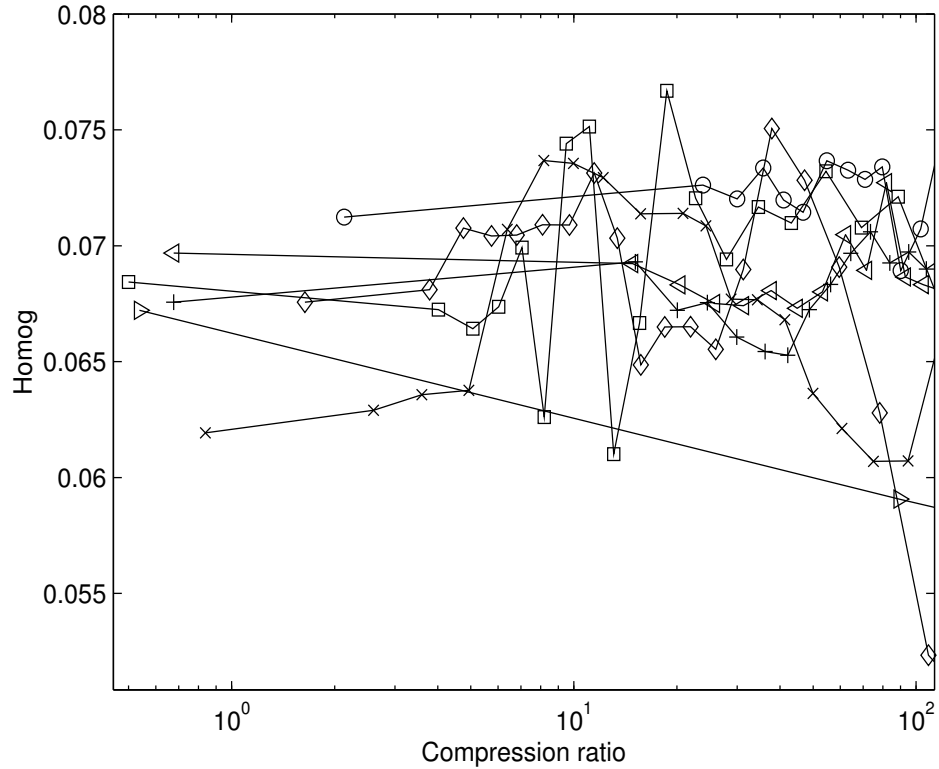


Figure 4.18: Scores obtained with Homog for dataset 6fatRand compressed with DWT (-+), MultiFractal (-◁), IK (-▷), IKstd (-◦), DCV (-×), DCT (-◻) and Threshold (-◊).

To understand this interpretation, following example is constructed:

$$X = [0000; 1111] \quad (4.1)$$

$$Y1 = [0000; 1111] \quad (4.2)$$

$$Y2 = [0101; 0101] \quad (4.3)$$

$$Y3 = [1234; 5678] \quad (4.4)$$

$$(4.5)$$

The values of AMI are:

$$AMI(X, Y1) = H(X) + H(Y1) - H(X, Y1) = 1 + 1 - 1 = 1 \quad (4.6)$$

$$AMI(X, Y2) = H(X) + H(Y2) - H(X, Y2) = 1 + 1 - 2 = 0 \quad (4.7)$$

$$AMI(X, Y3) = H(X) + H(Y3) - H(X, Y3) = 1 + 3 - 3 = 1 \quad (4.8)$$

$$(4.9)$$

where matrices  $X$ ,  $Y1$ ,  $Y2$ ,  $Y3$  represent distributions of pixel values for four different images as shown in Fig. 4.19.  $H(X)$  is Shannon entropy for the image  $X$ .  $H(X, Y)$  is the joint entropy between image  $X$  and  $Y$ . The cluster which is used to calculate the entropy for each image is so designed that each gray value is grouped to an individual cluster.

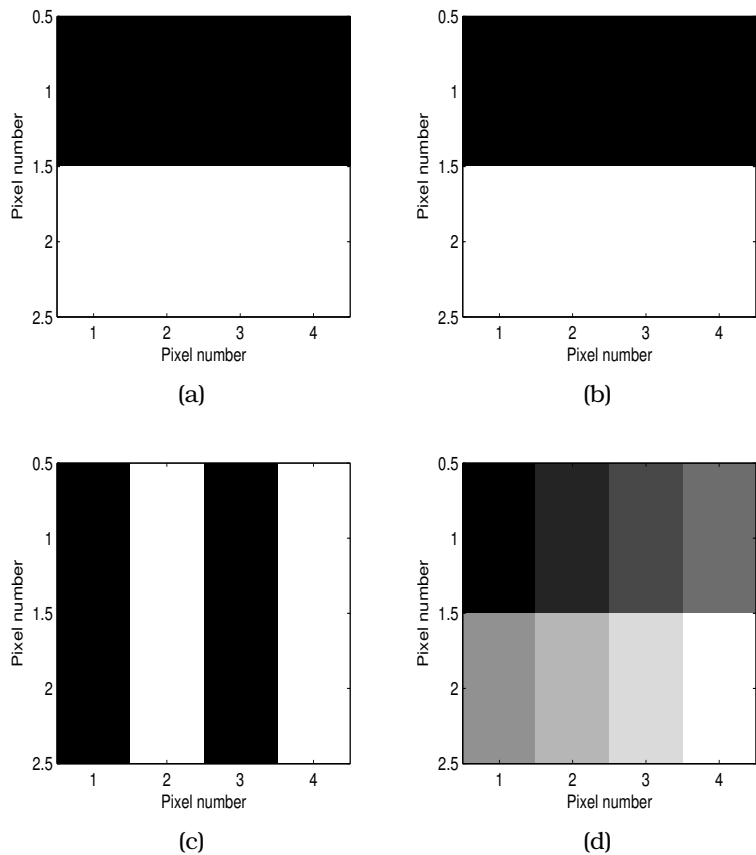


Figure 4.19: Example images for  $X$  (a),  $Y1$  (b),  $Y2$  (c) and  $Y3$  (d).

Since the reference image  $X$  has large homogeneous areas with values of 0 and 1, it is totally different from the image  $Y3$  which has the pixel-wise changed gray values. According to the values of AMI the perfect image  $Y1$  has the same score of image quality as the image  $Y3$  which is degraded significantly. The reason is that the entropy of distorted image  $H(Y3)$  increases as fast as the joint entropy  $H(X, Y3)$ . The achieved AMI values are not reduced due to the increased entropy of the image  $Y3$ . Therefore AMI is unsuitable for image with significant distortions.

The images of datasets compressed at compression ratios larger than 20 have decreasing tendency of quality with increasing compression ratios due to human perception. Nevertheless this tendency is not shown by the scores for Homog, NormGrdt, PSNR and SSIM. None of these scores after compression have similar behavior to the human perception as the images of the compressed dataset 6fatRand. The reason is that the imaged objects in dataset 6fatRand have a complex structure. At high compression ratios the distorted objects in images of compressed datasets are significantly different from that in the reference. Thus these scores are not capable for evaluation of these significant image distortions.

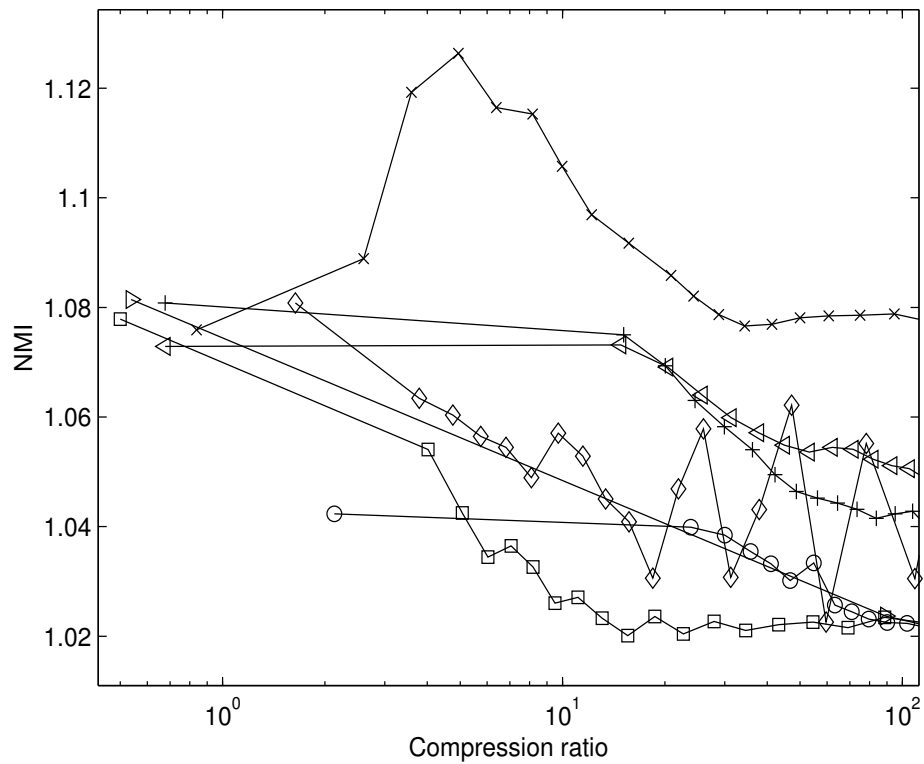


Figure 4.20: Scores obtained with NMI for dataset 6fatRand compressed with DWT (+), MultiFractal (<-<'), IK (<->'), IKstd (o), DCV (x), DCT (□) and Threshold (<->').

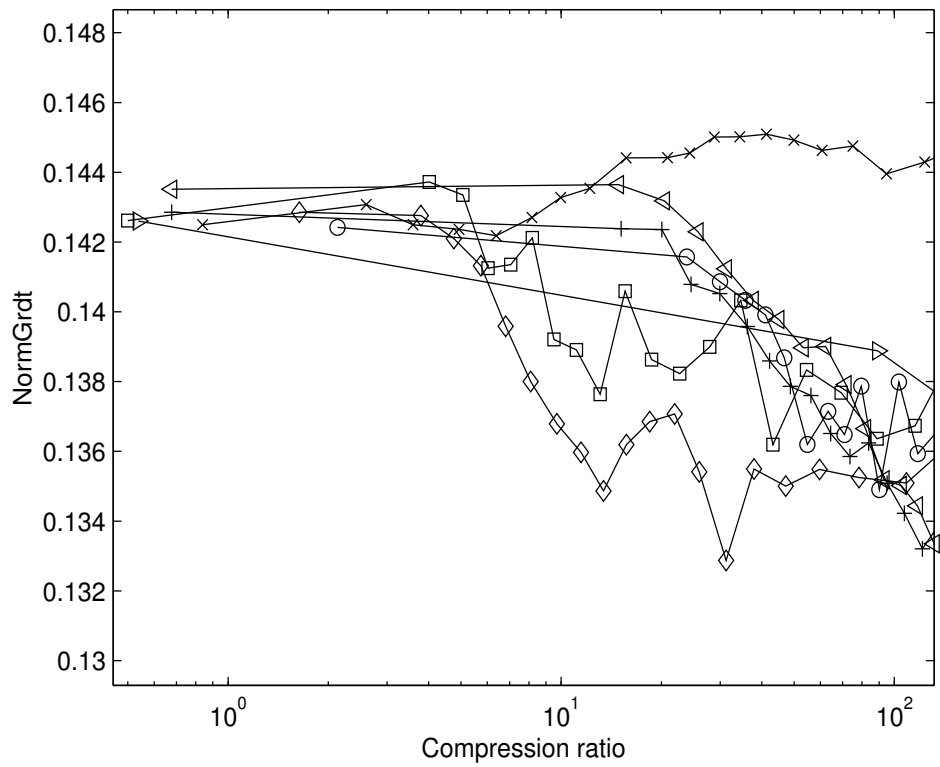


Figure 4.21: Scores obtained with NormGrdt for dataset 6fatRand compressed with DWT (-+), MultiFractal (-◁), IK (-▷), IKstd (-○), DCV (-×), DCT (-□) and Threshold (-◇).

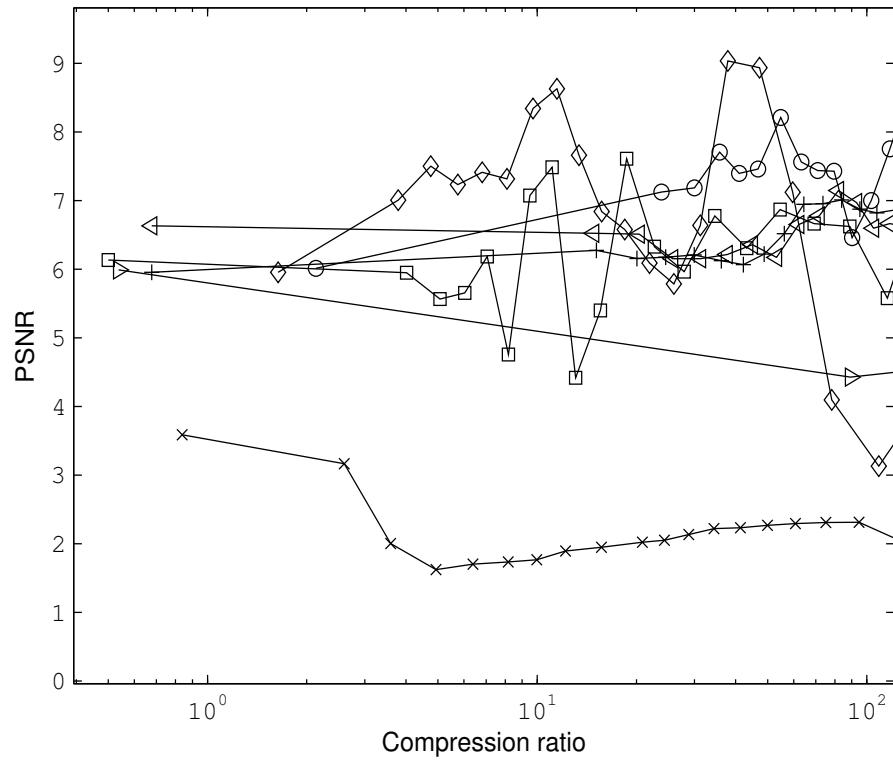


Figure 4.22: Scores obtained with PSNR for dataset 6fatRand compressed with DWT (-+), MultiFractal (-◁), IK (-▷), IKstd (-○), DCV (-x), DCT (-□) and Threshold (-◇).

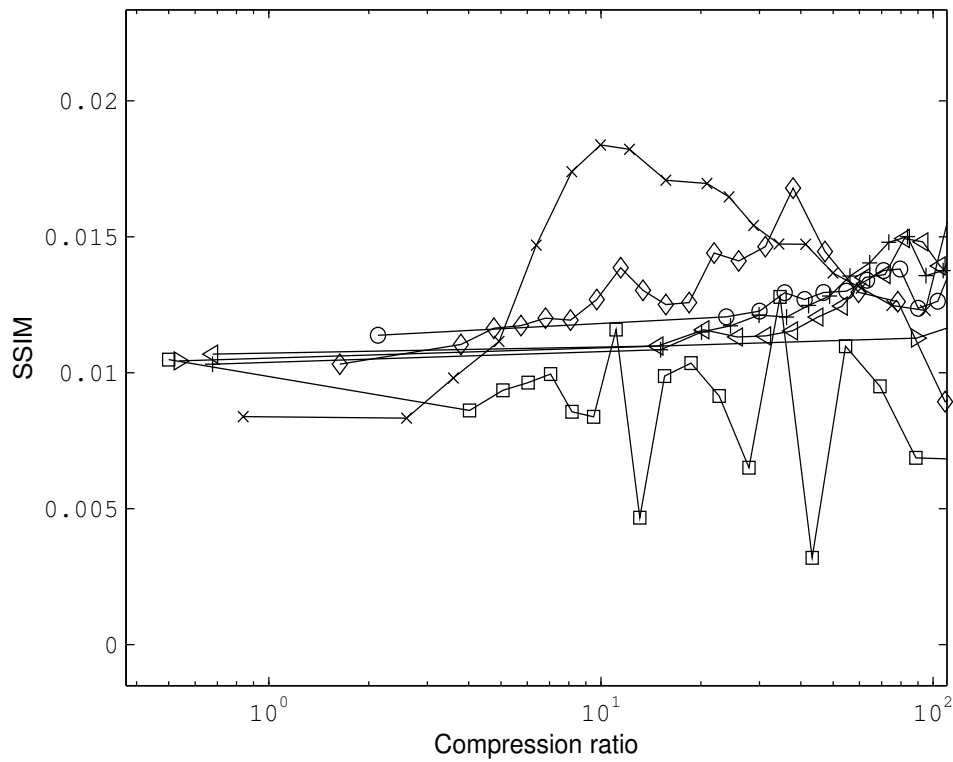


Figure 4.23: Scores obtained with SSIM for dataset 6fatRand compressed with DWT (+), MultiFractal ( $\triangleleft$ ), IK ( $\triangleright$ ), IKstd ( $\circ$ ), DCV ( $\times$ ), DCT ( $\square$ ) and Threshold ( $\diamond$ ).

### 4.2.1.3 Scores of optical flow based estimator

The optical flow based estimator was tested using the dataset 6fa-tRand compressed with different compression methods and compression ratios. The reconstructions are scored with the estimator OFintenEntry using the ideal reference image.

The experimental results are shown in Fig. 4.24. The scores of all compression methods have the fluctuating tendency. The maximum value of the scores is at the highest compression ratio. At the compression range from 20 to 100 the scores for images of datasets compressed with DCV have higher values than with all other compression methods. The rest of lines in Fig. 4.24 also fluctuate. This result is inconsistent with the human perception.

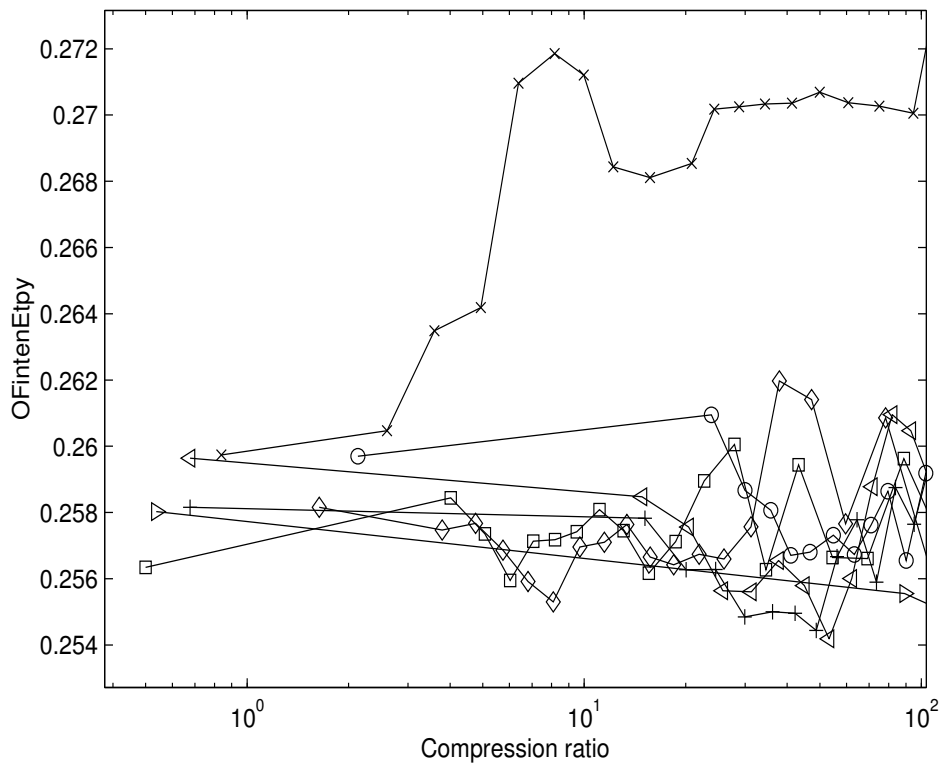


Figure 4.24: Scores obtained with OFintenEntry for dataset of 6fa-tRand compressed with the methods such as DWT (+), MultiFractal (◁), IK (▷), IKstd (○), DCV (×), DCT (◻) and Threshold (◊).

The reason to get the maximum score of the OFintenEntpy at the highest compression ratio is the small entropy of the image of compressed datasets at the highest compression ratio. In this image the imaged object has vanished. According to the definition of the OFintenEntpy in section 3.4.2.2, the values of scores increase with decreasing entropy of the optical flow image which is the image of compressed dataset.

A similar argument may be used to explain the high scores of the images compressed with DCV. The strong distortions in these images result in a significantly decreasing entropy of images. Thus the scores of OFintenEntpy have the highest values for unreasonable high compressions.

#### **4.2.1.4 Scores of the committee model based estimator**

The images of the compressed dataset 6fatRand are scored with CMM introduced in section 3.4.3. The training cases are designed by adding to the original image distortions defined in section 3.4.3.5 blurred image, dilated object, eroded image, and uniform noise. The other designed distortion types introduced in section 3.4.3.5 are not selected, since these distortions are not observed in images of datasets compressed at low compression ratios.

The selection of these distortion types for CMM depends on the evaluated images and the used different compression methods. The implemented compression methods influence the compression artifacts in images. The selected distortion type is used to simulated these artifacts. E.g. the resized or overlapping resized objects are only considered with the DCV method, because the pulse information is degraded in decompressed A-scans so strong that the size of the reconstructed object is changed.

The distortion grades are defined in section 3.4.3.5. To get an approximately linear relation between scores and distortion grade only small distortions are allowed to simulate compression artifacts. The chosen small range of the image distortions corresponds to the compression artifacts at compression ratios smaller than 20. E.g. the uniform noise from first to tenth grade is created in the range from 1 % to 10 % compared to the maximum gray value of images. The distorted images at the fifth distortion grade for the selected distortion types are shown in Fig. 4.25. The contours of the imaged

objects become unclear in Fig. 4.25(b) to 4.25(c) and 4.25(d). The background noise increases significantly in Fig. 4.25(e) and 4.25(f).

These training cases are evaluated at first with the selected image quality estimators introduced in section 3.4.1. The selected estimator has the ability to show the variation of grades for one or more selected distortion type. The achieved scores are then used to calculate the weight of each estimator in CMM with the method introduced in section 3.4.3.3.

The achieved CMM is used to score images of compressed datasets. The compression methods DWT, MultiFractal and IKstd are selected and compared here, since they have a relatively higher performances than other compression methods as discussed in section 4.2.1. The maximum compression ratio is limited to approx. 100, since the images of datasets compressed with a compression ratio of 100 have finally lost the most important information of the USCT image.

The achieved scores with CMM are shown in Fig. 4.26. The CMM values are decreasing until at a compression ratio of approx. 60 to 70 the score vanishes. The scores of CMM for DWT and MultiFractal methods are higher than for IKstd.

The results with CMM for dataset bloodbone are shown in Fig. 4.27. The local maximum values of scores for these three compression methods are at the range of compression ratios from 10 to 20. The CMM scores are decreasing at compression ratios larger than 20.

In all these cases compression ratios of about 10 to 20 seem to be obtainable with no unacceptable losses in image quality. This result agrees with human perception as it was shown in the sequence of figures in section 4.2.1.1.

#### **4.2.1.5 Filtered original images as reference**

According to the methodology proposed in section 3.5.1.2, the edge enhanced original image is used as the reference for the simulated dataset 6fatRand. The designed reference is shown in Fig. 4.28.

The reconstruction artifacts and parts of the noise in the A-scans affect the quality of the filtered original images. These artifacts and the noise cannot be removed completely by the edge enhancement

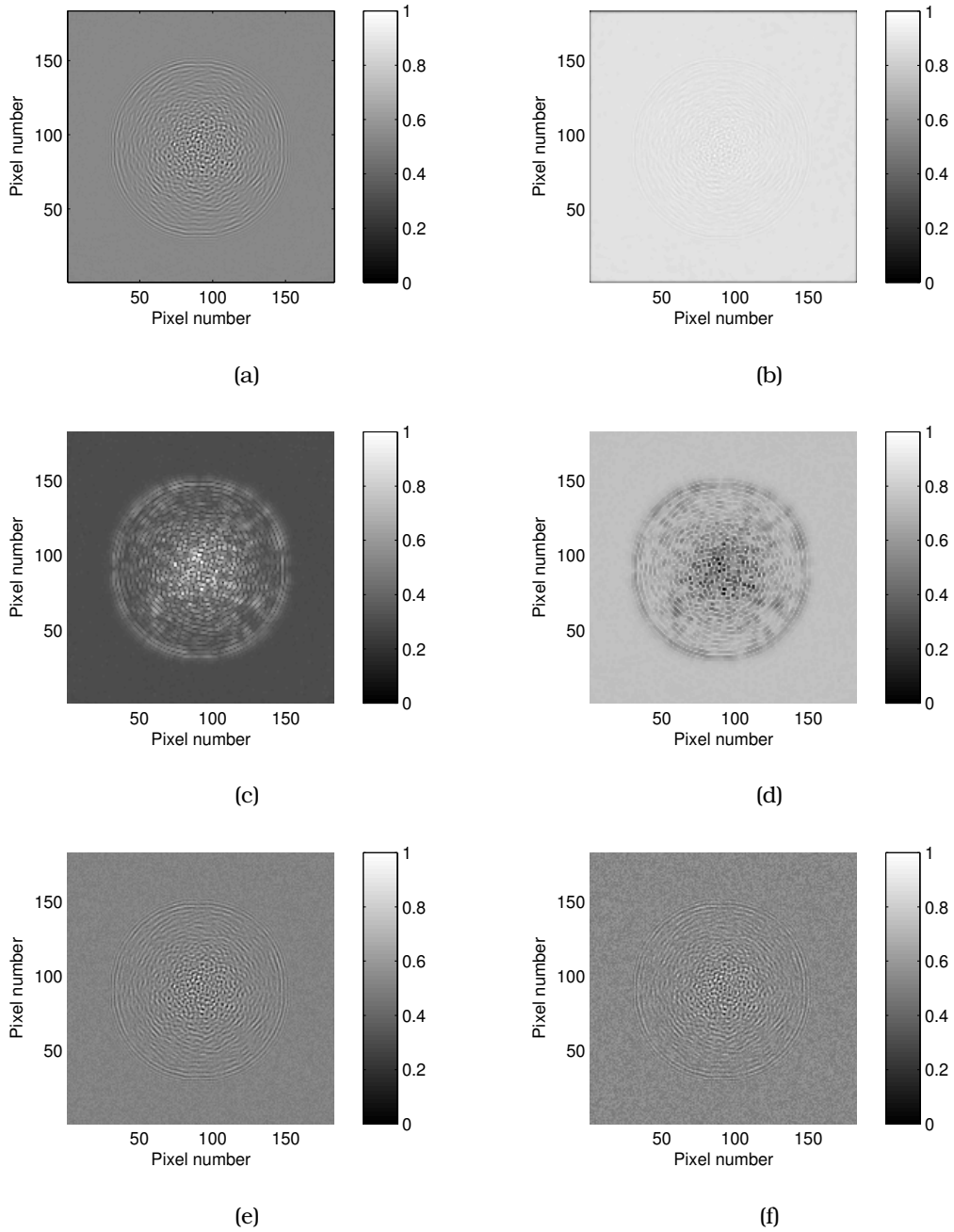


Figure 4.25: The original image(a) for dataset 6fatRand is degraded by adding simulated distortions at the fifth grade (b) blurred image, (c) dilated object, (d) eroded image, (e) uniform noise and (f) speckle noise.

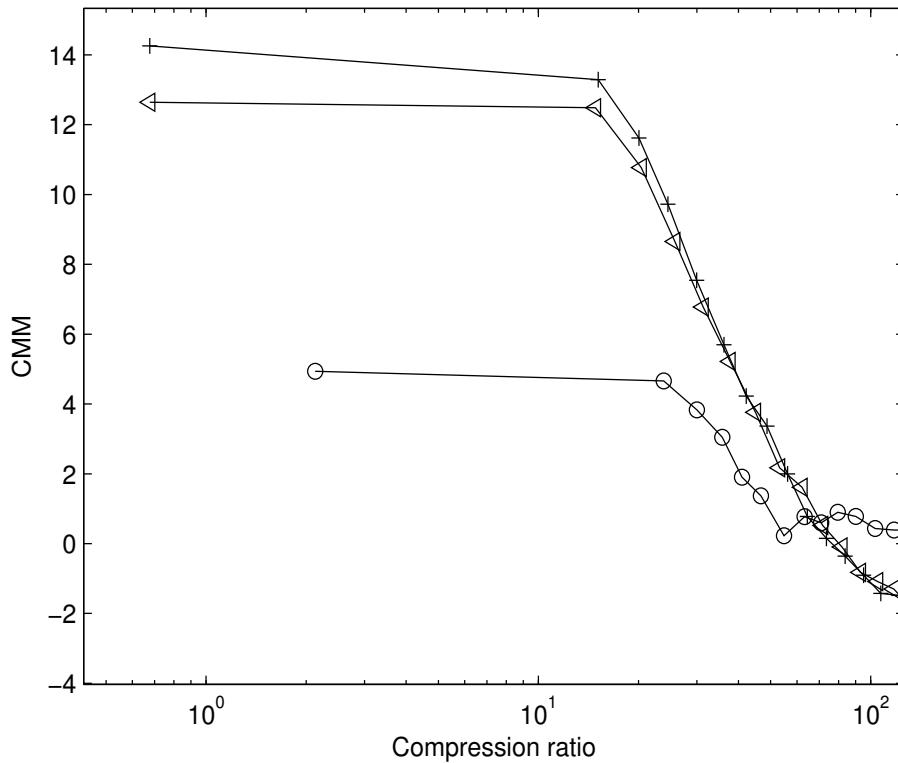


Figure 4.26: Scores obtained for dataset 6fatRand with CMM for compression methods DWT (+), MultiFractal (◁) and IKstd (o).

filters.

The corresponding evaluation results for AMI are shown in Fig. 4.29. The compared compression methods are DWT, MultiFractal, IK, IKstd, DCT and Threshold. The compression method DCV and the images with Threshold at compression ratios larger than 20 are not considered due to the observed distortions in images in Fig. 4.14.

The AMI curves decrease for all compression methods. The scores for DWT and MultiFractal are higher than for other compression methods. The DCT method has smallest values of scores at a large range of compression ratios.

Compared to the results with the ideal reference image in the section 4.2.1.2, there are no local maximum values for the scores with the filtered original image as references. The scores are mono-

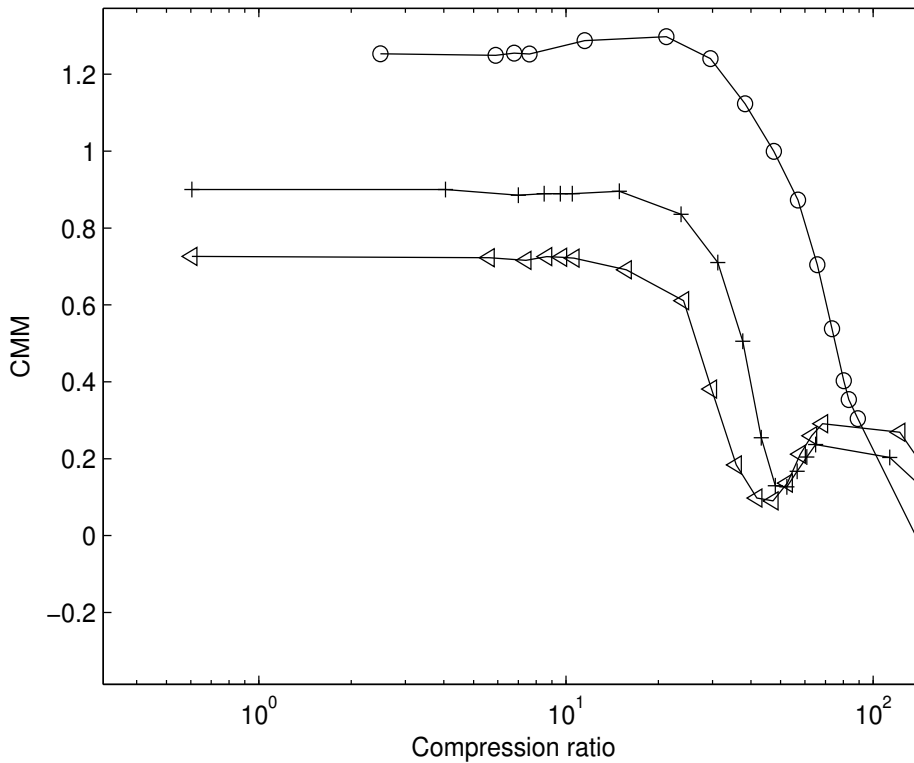


Figure 4.27: Scores obtained for dataset bloodbone with CMM for compression methods DWT (+), MultiFractal (◁) and IKstd (◊).

tonously decreasing. I.e. the differences between reference and images of compressed datasets are increasing with increasing compression ratios. One reason is that the compression artifacts in images of compressed datasets increase with increasing compression ratios. Another reason is that the artifacts and real content of the original image are reduced in the image of compressed dataset.

#### 4.2.1.6 Different mother wavelets

The different mother wavelets discussed in section 2.5.4 are analyzed with the simulated dataset 6fatRand to find the best wavelet for DWT. The standard image quality estimator AMI is employed with the filtered original image as the reference image.

The results are shown in Fig. 4.30. In the range of compression ra-

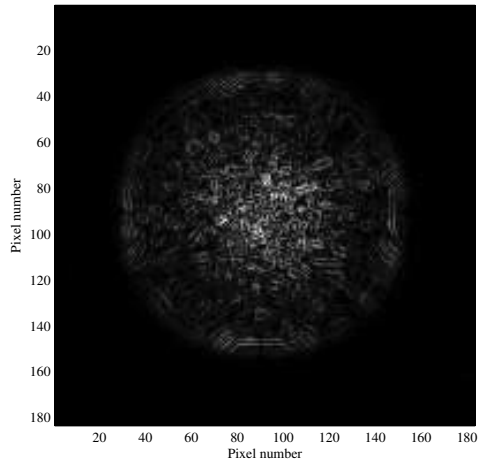


Figure 4.28: Edge enhanced image for simulated dataset 6fatRand.

tios from 1 to 100 the AMI values for Haar wavelet are smaller than for the others. All other tested mother wavelets have a very similar good behaviour.

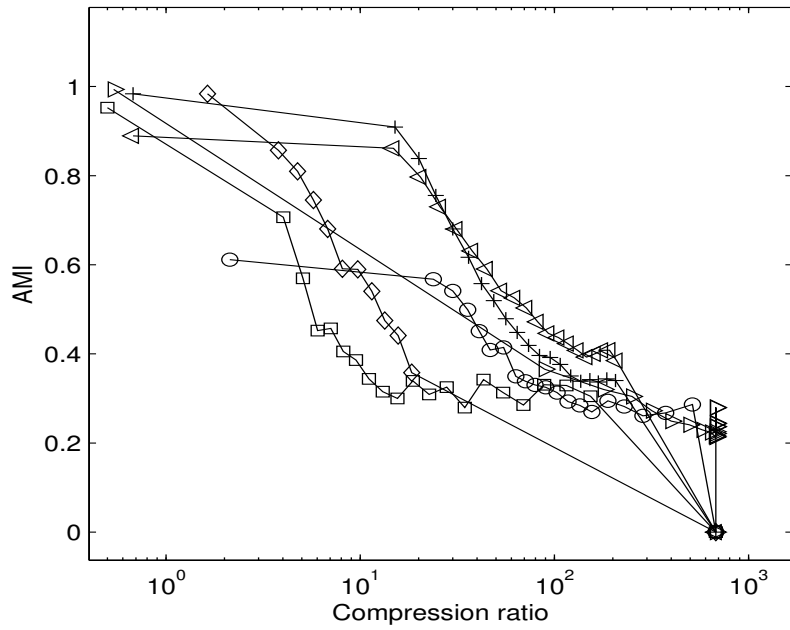


Figure 4.29: Scores obtained for simulated dataset 6fatRand with AMI and filtered original images as reference for compression methods DWT (+), MultiFractal (◁), IK (▷), IKstd (○), DCT (◻) and Threshold (◇).

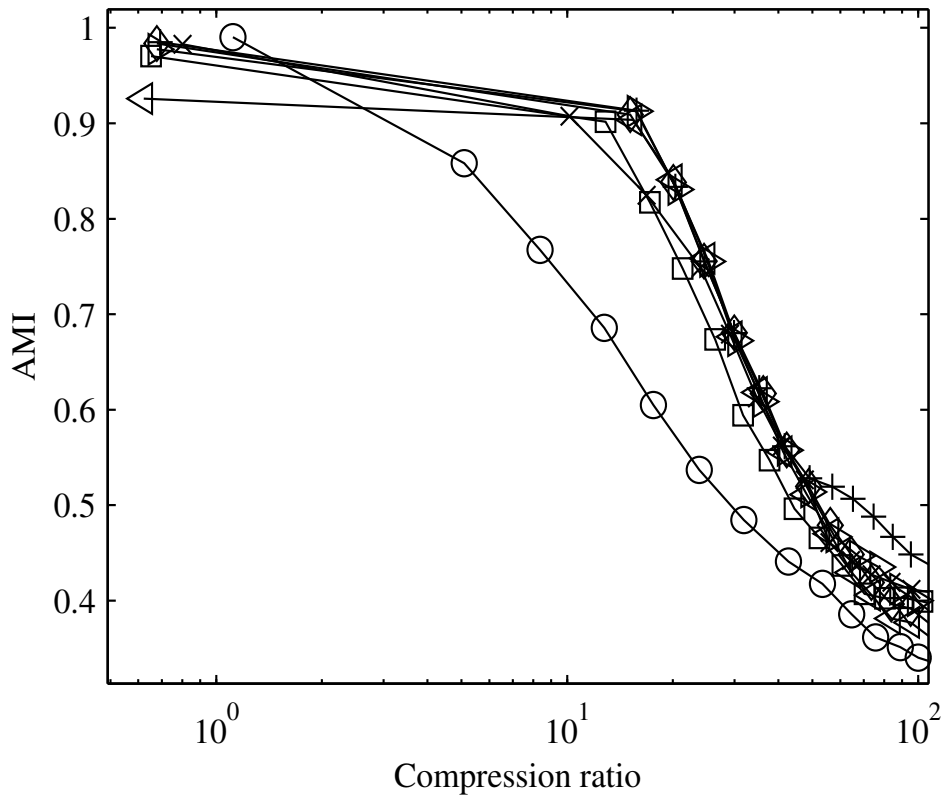


Figure 4.30: Scores with AMI using filtered original image as reference for comparison of different standard mother wavelets Beylkin (+), Coiflet 5-tap (◁), Daubechies 20-tap (▷), Haar (○), Symmlet 4-tap (×), Vaidyanathan (◻) and Symmlet 10-tap (◊).

## 4.2.2 Real datasets

The real datasets are measured with real USCT setups. The real USCT setups include 2D and 3D versions. The structure of 3D USCT is introduced in section 2.2.1. The 2D USCT setup is the previous version of 3D USCT and consists of one layer of emitters and receivers which are in the same horizontal plane. Compared to the 3D USCT setup there are 100 emitter and receiver positions of transducers in the 2D USCT setup. In this work only the dataset for the image object phantom2 is measured with the 2D USCT setup; other datasets are obtained with 3D USCT. For simplicity only one slice of these 3D images are shown.

In order to get the “real datasets”, phantoms are employed as imaged objects. The precise geometry and the relative positions of imaged objects in USCT setups are in most cases unknown for the real datasets. The acoustic properties of components in imaged objects are also unknown. Thus the ideal reference images are not available.

Compared to the simulated datasets which do not contain noise, the noise in the real datasets arises from the experimental environment (electronics etc.). The influences of the noise in the image of compressed dataset have to be considered during the evaluation of the compression.

### 4.2.2.1 Imaged objects and compressed datasets

The characteristics of each imaged object are listed blow:

1. Phantom2 : Several nylon threads and PVC rods are surrounded by a plastic tube of 9 cm in diameter filled with water. These objects are located near the center of the 2D USCT cylinder vertically. The diameter of the nylon thread is 0.15 mm.
2. NylonGelatin: A nylon thread with a diameter of 0.2 mm is placed approx. in the center of the USCT setup vertically and surrounded by a gelatin cylinder with a diameter of 6.4 cm [38].
3. EggSkinned: The imaged object is a cooked egg without shell.
4. Breastphantom1: The imaged object is a clinical breast phantom (triple biopsy breast phantom, CIRS, Inc., Norfolk, USA). This phantom is breast shaped and contains cancer and cyst

mimicking masses of 2 to 10 mm in diameter. Its physical characteristics resemble approx. a 50% glandular breast. One cross section of the Breastphantom1 imaged with X-ray is shown in Fig. 4.31

5. Breastphantom2: This phantom is the second version of breast phantom with similar characteristics as Breastphantom1. Parts of the phantom are imaged.
6. Breastphantom3: This phantom is the third version of breast phantom with similar characteristics as Breastphantom1. Parts of the phantom are imaged.

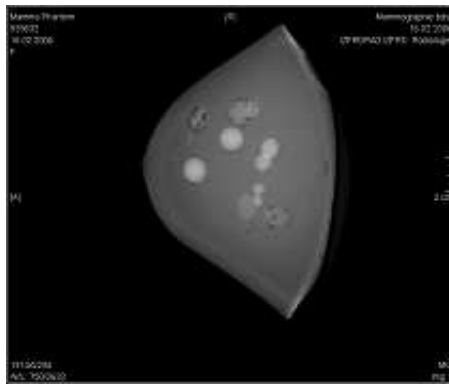


Figure 4.31: X-ray image of one cross section of Breastphantom1.

The smallest objects in the phantom2 are reconstructed in the original image in Fig 4.32. The cross section of the nylon threads with a diameter of 0.15 mm is visible in the image.

These contents of phantom2 in images of compressed datasets vary with increasing compression ratios 10, 20, and 60 shown in Fig. 4.33(b), Fig. 4.33(c) and Fig. 4.33(d), respectively. Compared to the original image shown in Fig. 4.33(a) details of nylon threads are visible in images of datasets compressed at compression ratios 10 and 20. I.e. The smallest details of the imaged objects are kept in the image reconstructed with the compressed dataset, which corresponds to 4.5% of the original data amount. Most details of the nylon threads are lost at the compression ratio of 60.

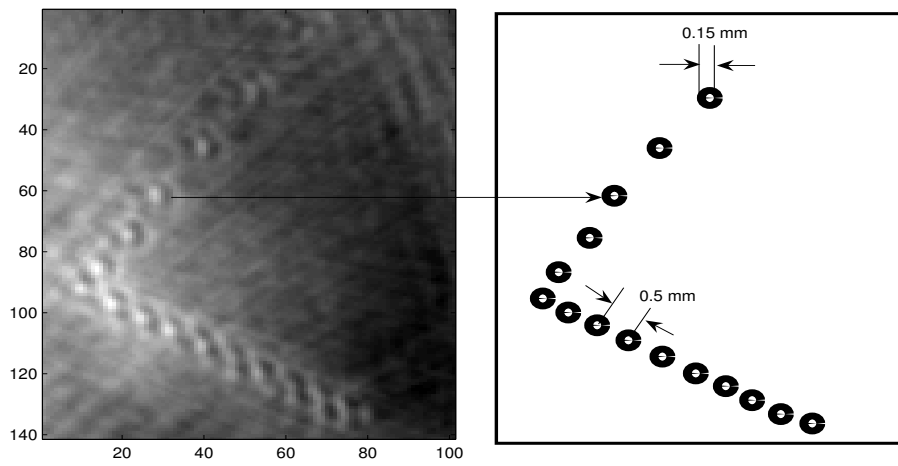


Figure 4.32: Position of the cross section of nylon threads (right) and the original image reconstructed with the uncompressed data-set (left).

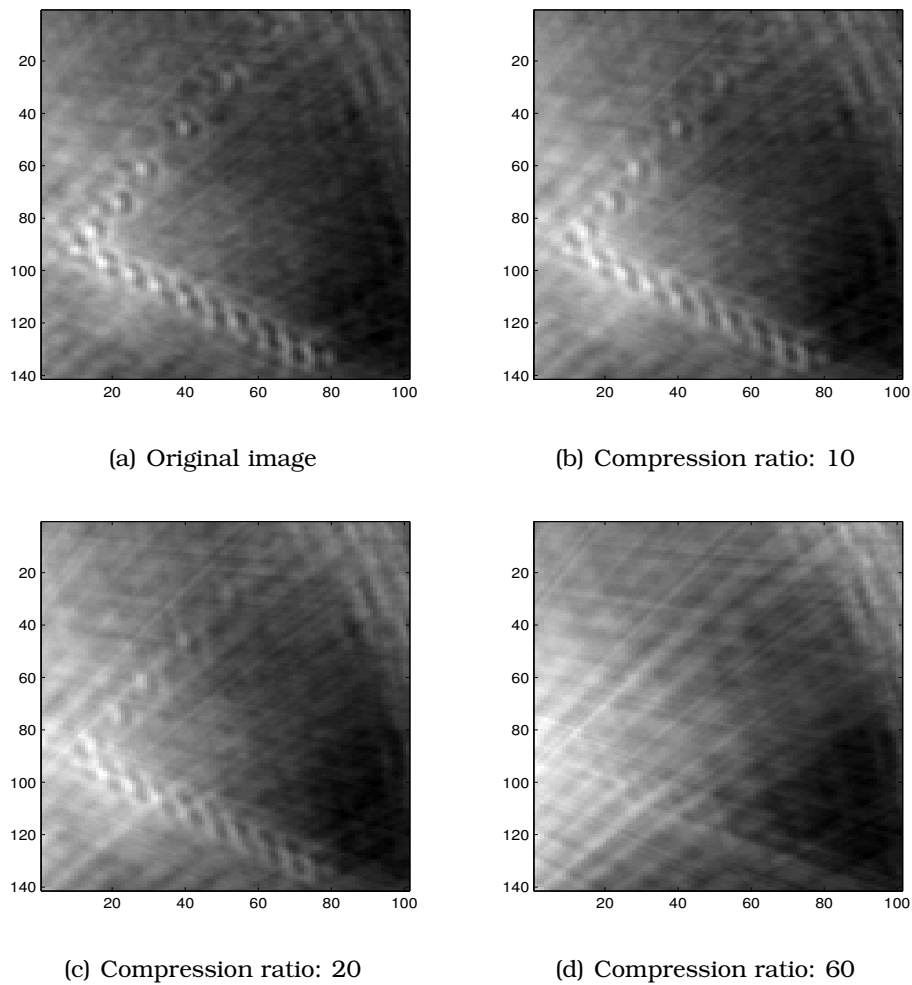


Figure 4.33: The original image (top left) and images of datasets compressed with DWT at compression ratios: 10 (top right), 20 (bottom left), 60 (bottom right).

The images for dataset Breastphantom1 compressed with different methods at the compression ratio 15 are shown in Fig. 4.34. The low quality of the original image is due to the low performance of the reconstruction method used in the year of 2006. With the improved version of reconstruction methods, the quality of original image is increasing. The main contours of breast phantom1 are visible in the images with DWT, MultiFractal and IKstd. In the images for DCT, Threshold and DCV the basic structures of imaged objects are invisible.

#### **4.2.2.2 Filtered original images as reference**

The filtered original image is used as reference to evaluate the images of compressed real datasets. The imaged Breastphantom1 is employed as an example. According to the methodology proposed in section 3.5.1.2, the original image is filtered to achieve the edge enhanced objects for evaluation of the compressed datasets.

The evaluation results with AMI are shown Fig. 4.35. A local maximum of AMI at compression ratios between 10 and 20 for DWT and MultiFractal compression is visible. Optimal images are obtained for DWT and MultiFractal at compression ratios of about 12. For larger compression ratios the scores decrease.

#### **4.2.2.3 Designed ideal reference**

The ideal reference images are designed for evaluation of the image of compressed dataset. The precise information of the position and geometry as well as acoustic properties of imaged objects is unknown for the real datasets. The contours of imaged objects in the original images are used to deduce the ideal reference images.

A software tool in Matlab is designed to extract the contour information of imaged objects. The pixels of the contours in the original images are selected manually for the reference image. The gray values of selected pixels are used as gray values in the reference image.

The original and reference images for the imaged object NylonGelatin are plotted in Fig. 4.36. The nylon thread has a high gray value in the ideal reference image due to its high acoustic impedance relative to the gelatin cylinder. The contour of gelatin cylinder corresponds to a circle in the center with a low pixel value in the reference image.

The original and reference images for the imaged object EggSkinned are plotted in Fig 4.37. The main shape of the egg is an ellipse. Parts of details in the egg is drawn with a dotted line in the ideal reference image, since these details are not reconstructed clearly in the original image.

The original and reference images for the imaged object Breastphantom1 are plotted in Fig. 4.38. The contours of the Breastphantom1

are drawn with solid and dotted lines in the ideal reference image, respectively. The dotted lines within the contours of the Breastphantom1 accentuate the cysts.

The original and reference images for the imaged objects Breastphantom2 and Breastphantom3 are plotted in Fig. 4.39 and Fig. 4.40, respectively. The cysts of these phantoms are shown with small circles in the ideal reference images.

The evaluation of the achieved reference image for the imaged object NylonGelatin is based on the measured geometric information and acoustic properties of the materials which are used to construct the phantom. The ideal reference image designed for the imaged object EggSkinned is evaluated by using the shape of the egg. The reference images for imaged objects Breastphantom1, Breastphantom2 and Breastphantom3 are evaluated with the corresponding X-ray images.

In original images for imaged objects NylonGelatin, EggSkinned and Breastphantom1 are shown in Fig. 4.36(a), Fig. 4.37(a) and Fig. 4.38(a). The main contours of imaged objects gelatin cylinder, egg and breast phantom1 are visible. The details in the images are distorted significantly by the background noise. For the imaged objects Breastphantom2 and Breastphantom3 in the original images shown in Fig. 4.39(a) and Fig. 4.40(a) parts of cysts are reconstructed and visible. The shape of some cysts can be distinguished. The other cysts are not clearly reconstructed in the original image due to their relative positions to the observers.

#### **4.2.2.4 Scores with CMM**

The CMM is implemented for the evaluation of the compression methods with real datasets. The imaged objects Breastphantom1, Breastphantom2 and Breastphantom3 are used as examples. There are fewer objects in the reconstructed images for Breastphantom2 and Breastphantom3 than in Breastphantom1. The designed reference images in section 4.2.2.3 are used for comparison with the images of compressed datasets.

The evaluation results are shown in Fig. 4.41, Fig. 4.42 and Fig. 4.43, respectively. The used compression methods are DWT, MultiFractal and IKstd. Based on the analysis in section 4.2.1 these

compression methods have higher performance than other adapted lossy compression methods.

The scores in Fig. 4.41 are increasing for Breastphantom1 with compression methods DWT and IKstd at compression ratios smaller than 50. For compression method MultiFractal the increasing tendency continuous until the compression ratio 100 is reached. The high values of CMM at the compression ratios above 50 is possible due to the simplified structure of imaged objects in the reference image. The main structures of imaged objects are kept in the images of datasets compressed also at high compression ratios.

The scores in Fig. 4.42 for Breastphantom2 are decreasing for compression methods DWT and MultiFractal at compression ratios larger than 15. The local maximum values of CMM are within the range of compression ratios from 10 to 20. The values of CMM for compression method IKstd are not stable and have smaller values than the other methods.

The results in Fig. 4.43 for Breastphantom3 have unstable behaviour for all three compression methods at compression ratios larger than 15. These results may be related to the low quality of the original image as well as the reference image. In the meantime 3D-USCT has a very much improved reconstruction method which was not available at the time of this work.

### **4.3 Evaluation of data compression with human perception**

The image of compressed dataset in USCT are also scored by subjective estimators by using 16 students. The scores of the standard image quality estimators selected in section 3.4.1 and CMM are compared with the subjective scores.

The mean vote score (MVS) is employed as the subject image quality estimator. The MVS are achieved with 16 observers, who are educated people in image processing. Images of compressed datasets are scored by these observers. The scores are averaged to achieve a high quality of the score.

The consistency of the objective estimators with the MVS is evalu-

	Fig. 4.14(a)	Fig. 4.14(b)	Fig. 4.14(c)	Fig. 4.14(d)	Fig. 4.14(e)	Fig. 4.14(f)	CC_MVS
AMI	0.44	0.45	0.30	0.17	0.21	0.70	0.00
NMI	1.07	1.07	1.04	1.02	1.03	1.09	0.06
PSNR	6.16	6.51	7.13	6.33	6.58	2.02	0.30
SSIM	0.01	0.01	0.01	0.01	0.01	0.02	0.11
Homog	0.07	0.07	0.07	0.07	0.07	0.07	0.05
NormGrdt	0.14	0.14	0.14	0.14	0.14	0.14	0.17
GVFMI	0.73	0.73	0.46	0.22	0.25	0.68	0.31
CMM	11.62	10.77	4.66	0.47	1.00	10.14	0.81
MVS	4.63	5.25	4.06	1.50	1.75	1.00	1.00

Table 4.1: Images of dataset 6fatRand compressed with implemented compression methods at compression ratio 20 is scored with standard image quality scores, CMM and MVS. CC\_MVS is the correlation coefficient between objective scores and MVSs.

ated with the correlation coefficients between the scores estimated with MVS and objective estimators. The objective estimator with a high correlation coefficient has a high consistency with human perception [81].

#### 4.3.1 Simulated datasets

The images of compressed simulated datasets 6fatRand in Fig. 4.14 are used here as examples to show the correlation coefficients CC\_MVS between the objective estimators and MVS. The results are tabulated in Table. 4.1.

The correlation coefficient between CMM and MVS is approx. two times larger than that for other objective image quality estimators. The CMM shows a higher consistent with human perception than the state-of-the-art image quality estimators.

#### 4.3.2 Real datasets

The images of the compressed real dataset Breastphantom1 are shown in Fig. 4.34. The experimental results with objective and subjective estimators are shown in Table 4.2.

The correlation coefficient between CMM and MVS is larger than that for other objective image quality estimators. These results are similar to that with the simulated dataset 6fatRand and showed the

	Fig. 4.34(a)	Fig. 4.34(b)	Fig. 4.34(c)	Fig. 4.34(d)	Fig. 4.34(e)	Fig. 4.34(f)	CC_MVS
AMI	0.01	0.01	0.01	0.01	0.00	0.21	0.26
NMI	1.00	1.00	1.00	1.00	1.00	1.02	0.24
PSNR	16.34	17.21	15.77	13.50	11.00	19.08	0.10
SSIM	0.01	0.01	0.01	0.00	0.00	0.25	0.27
Homog	0.00	0.00	0.00	0.00	0.00	0.52	0.28
NormGrdt	0.00	0.00	0.00	0.00	0.00	0.51	0.27
GVFMI	0.02	0.02	0.02	0.02	0.01	0.05	0.04
CMM	1.24	0.92	1.07	0.72	0.62	0.52	0.74
MVS	4.43	4.92	4.64	3.02	1.00	1.34	1.00

Table 4.2: Images of dataset Breastphantom1 compressed with implemented compression methods at compression ratio 15 is scored with standard image quality estimators, CMM and MVS. CC\_MVS is the correlation coefficient between objective scores and MVSs.

large superiority of CMM over the standard estimators.

## 4.4 Validation of denoising ability

### 4.4.1 Noisy datasets

In order to test the denoising ability of adapted compressed methods, the simulated dataset 6fatRand is employed. The quality of denoising images is scored with AMI using the processed original images as the reference images. The denoising ability of the compression method DWT is validated as an example, since it has a high performance for compression of USCT datasets as shown with the experimental results in section 4.2.1.

The artificial noise is simulated with the methods introduced in section 2.6.2.1. The simulated noise has the size of  $-40\text{dB}$ ,  $-26\text{dB}$  and  $-20\text{dB}$  compared to the maximum value of A-scans. These noises are added into the A-scans of the dataset 6fatRand to construct the noisy datasets. The images reconstructed with noisy datasets are termed as noisy images. The noisy images are shown in Fig. 4.44(a), Fig. 4.44(c) and Fig. 4.44(e).

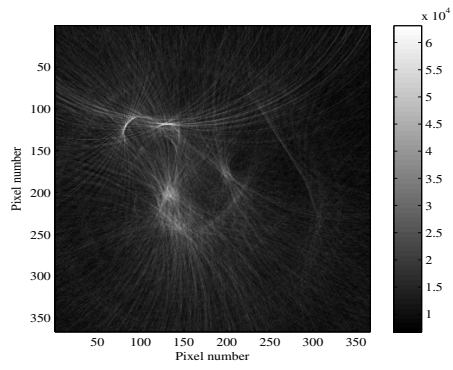
### 4.4.2 Compression of noisy datasets

The noisy datasets are filtered and compressed with DWT and reconstructed, as shown in Fig. 4.44(b), Fig. 4.44(d), and Fig. 4.44(f).

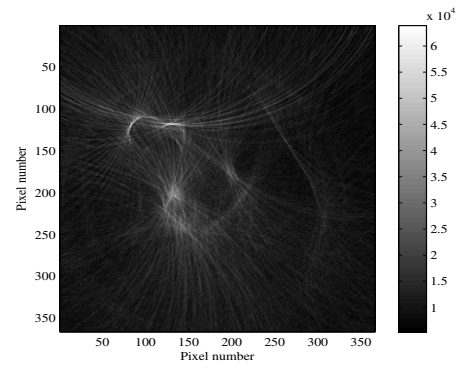
Images of compressed datasets are compared against noisy images. The noise in the image of dataset compressed with DWT is reduced in the background for the simulated dataset 6fatRand. Thus the contours of the objects in the images of the compressed datasets are again recognizable.

#### **4.4.3 Scores of denoising datasets**

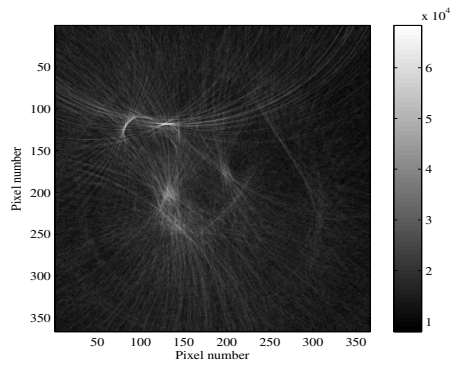
The denoising ability of the compression method DWT is evaluated with AMI. The corresponding scores of AMI are shown in Fig. 4.45. There are local maxima of AMI for the noisy datasets at all noise grades with the increasing compression ratios. These local maximum values are at the compression ratio approx. 20. These results are consistent with the subjectively obtained results shown in Fig. 4.44.



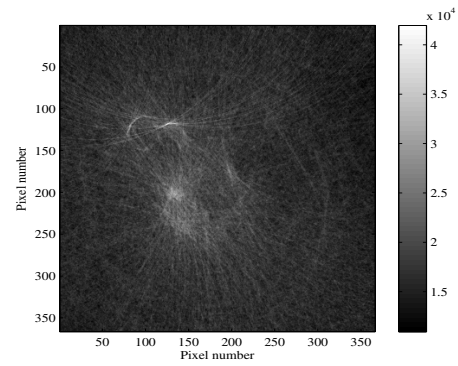
(a)



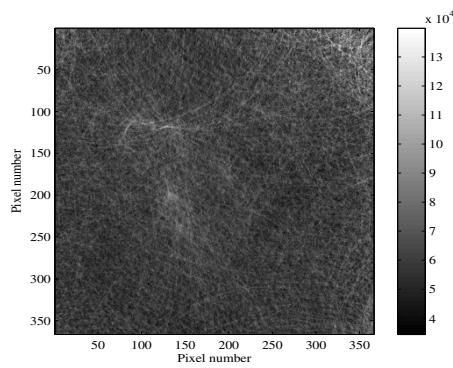
(b)



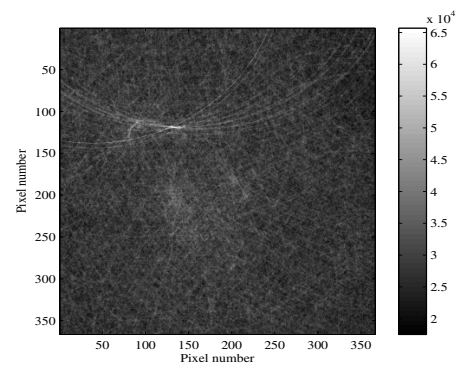
(c)



(d)



(e)



(f)

Figure 4.34: (a) Images of the real dataset Breastphantom1 compressed with (a) DWT, (b) MultiFractal, (c) Threshold, (d) IKstd (e) DCT and (f) DCV at a compression ratio of 15.

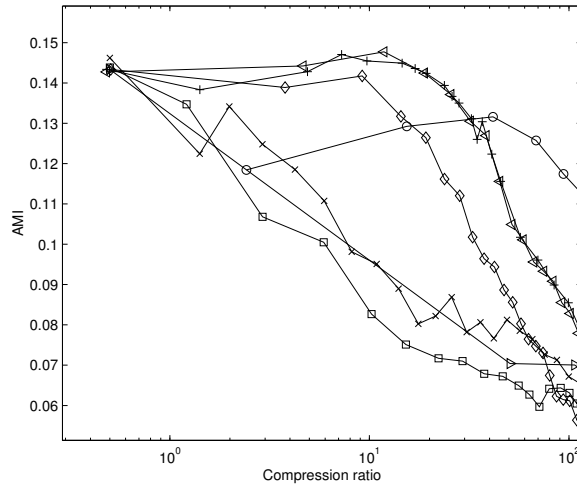


Figure 4.35: Scores obtained for real dataset Breastphantom1 with edge enhanced reference for DWT (-+), MultiFractal (-◁), IK (-▷), IK-std (-○), DCV (-×), DCT (-□), Threshold (-◇) and WavePDT(-▽).

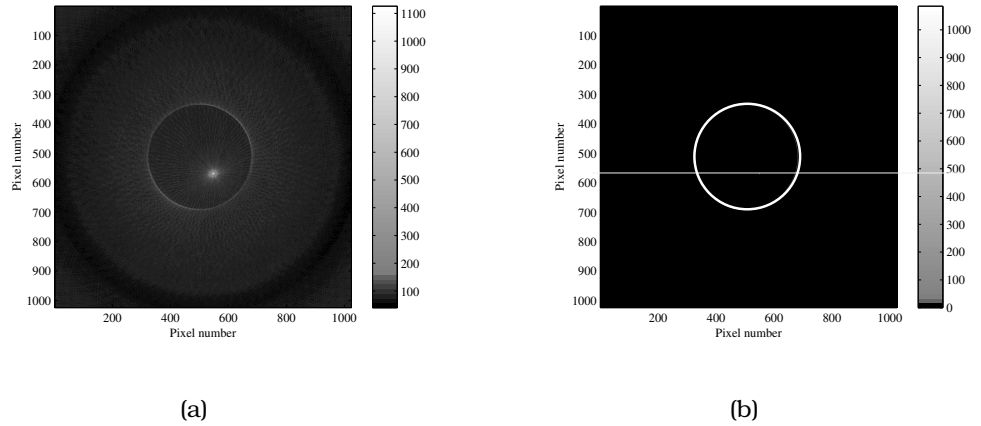


Figure 4.36: Real dataset NylonGelatin. (a) Original and (b) reference images (with enhanced edges for demonstration).

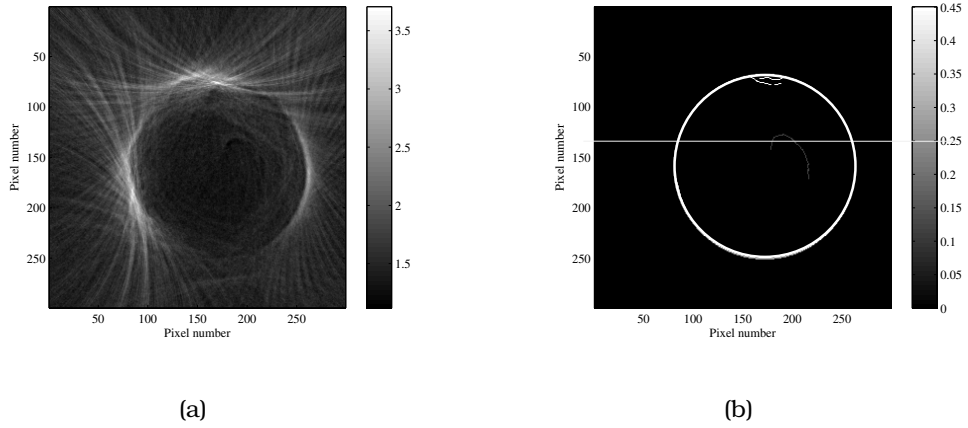


Figure 4.37: Real dataset EggSkinned. (a) Original and (b) reference images (with enhanced edges for demonstration).

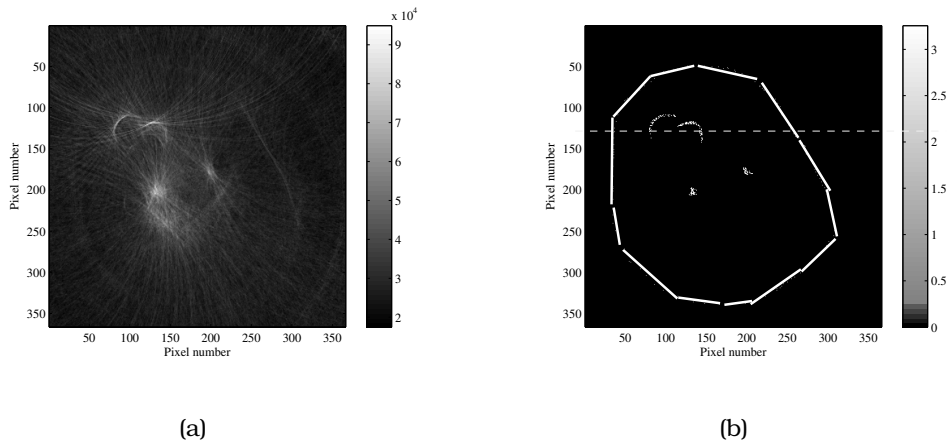
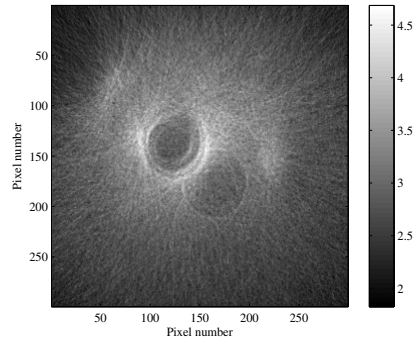
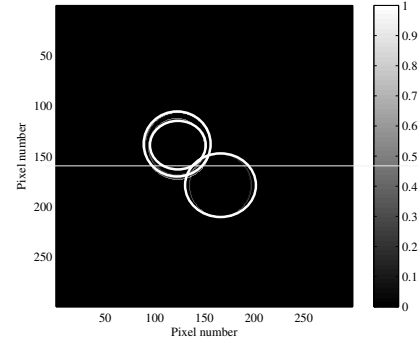


Figure 4.38: Real dataset Breastphantom1 for imaging CIRS breast phantom. (a) Original and (b) reference images (with enhanced edges for demonstration).

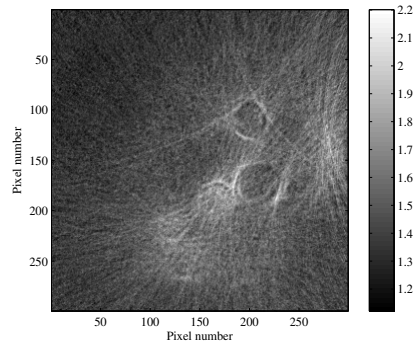


(a)

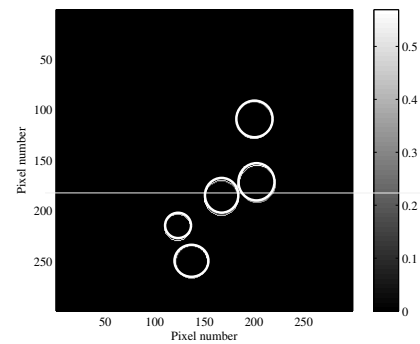


(b)

Figure 4.39: Real dataset Breastphantom2 for imaging CIRS breast phantom. (a) Original and (b) reference images (with enhanced edges for demonstration).



(a)



(b)

Figure 4.40: Real dataset Breastphantom3 for imaging CIRS breast phantom. (a) Original and (b) reference images (with enhanced edges for demonstration).

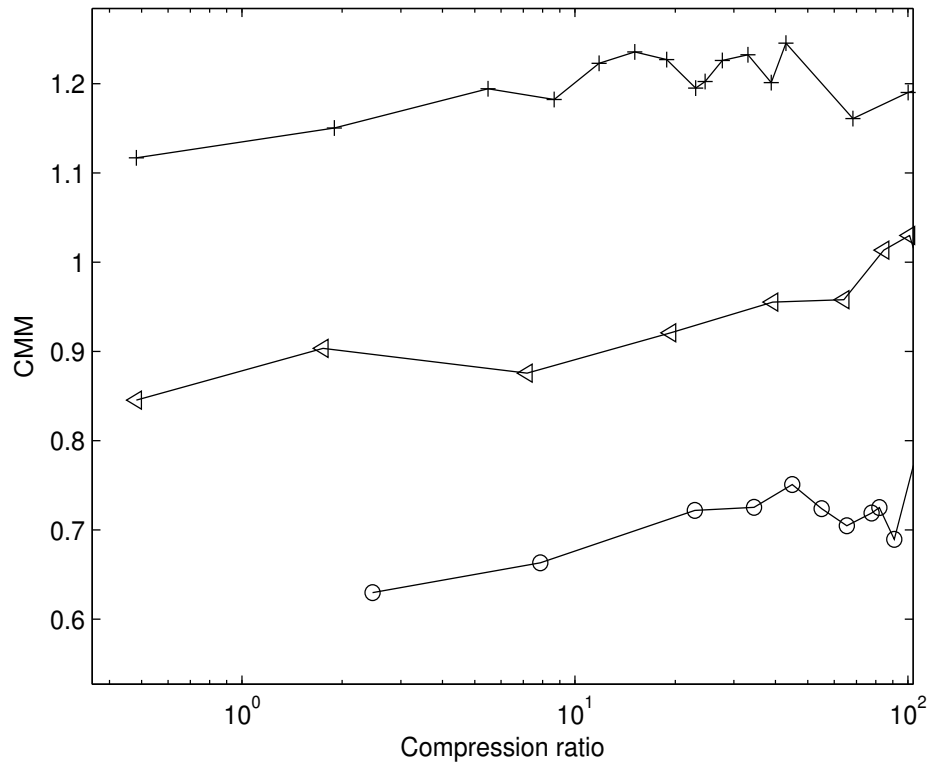


Figure 4.41: Scores of CMM for images of datasets Breastphantom1 compressed with DWT (+), MultiFractal (<-) and IKstd (-o).

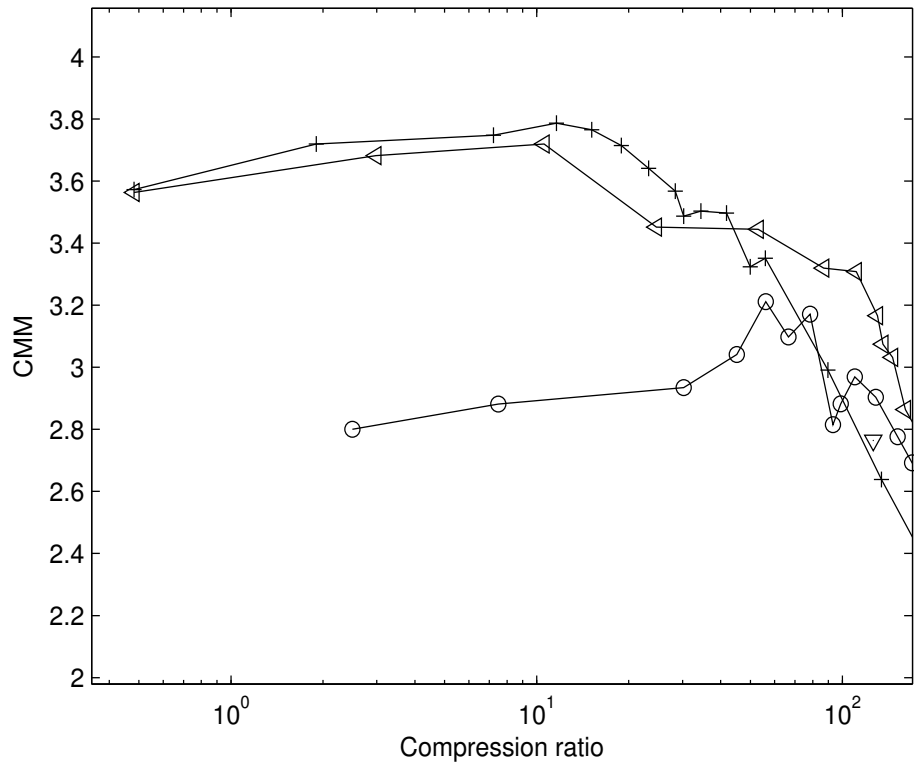


Figure 4.42: Scores with CMM for images of dataset Breastphantom2 compressed with DWT (+), MultiFractal (<-) and IKstd (o).

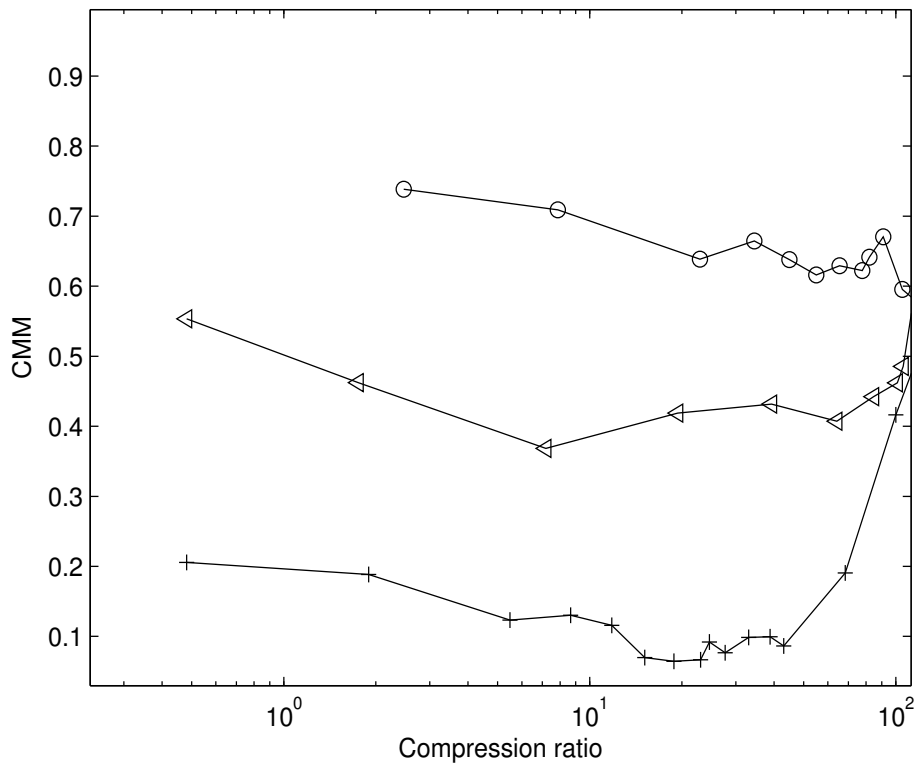
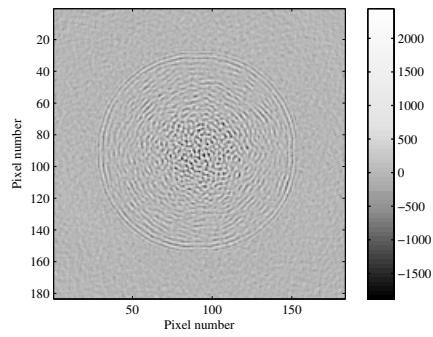
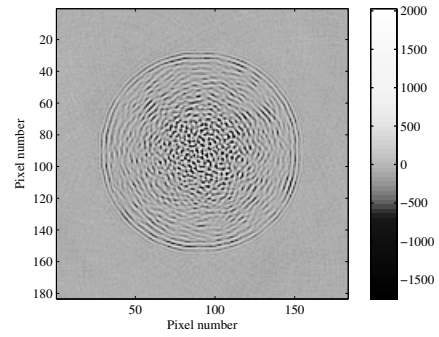


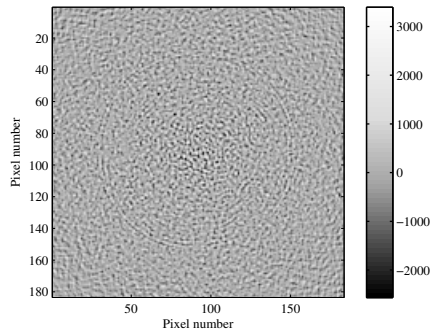
Figure 4.43: Scores obtained for dataset Breastphantom3 with CMM for compression methods DWT (+), MultiFractal ( $\triangleleft$ ) and IK-std ( $\circ$ ).



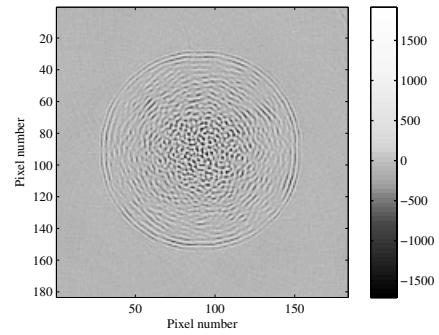
(a)



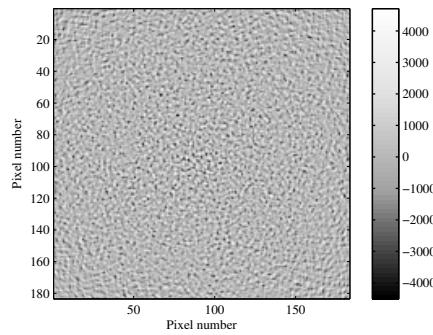
(b)



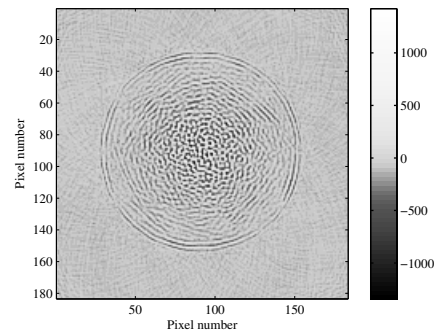
(c)



(d)



(e)



(f)

Figure 4.44: Noisy images with different noise grades (the size of noise is (a)  $-40\text{dB}$  (b)  $-26\text{dB}$ , (c)  $-20\text{dB}$  compared to the maximum amplitude in the A-scans) and the corresponding reconstructed images (b), (d) and (f) of the with DWT compressed datasets at a compression ratio of 20.

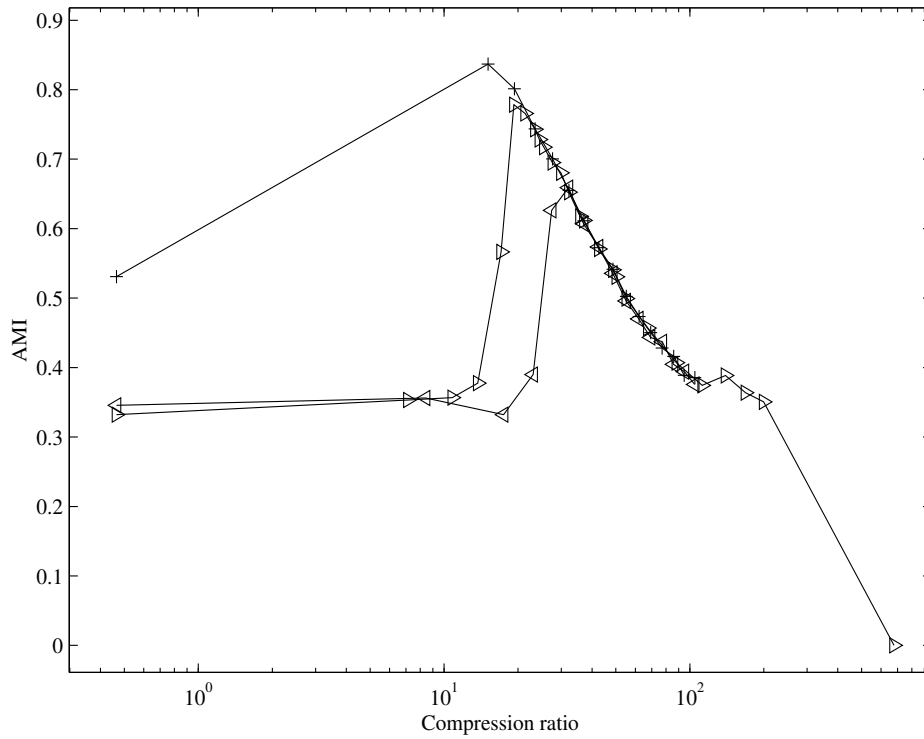


Figure 4.45: Scores with AMI for images of datasets compressed with DWT to evaluate denoising ability of compression method. Noise with a size of  $-40\text{dB}$  ( $-+$ ),  $-26\text{dB}$  ( $-▷$ ) and  $-20\text{dB}$  ( $-◁$ ) compared to the maximum amplitude of A-scans are added to A-scans before the compression process. Best imaging quality in respect to the AMI estimator is obtained at compression ratios between 10 to 20.

## **Chapter 5**

# **Discussion and conclusion**

In this work a data compression system for USCT was developed. The state-of-the-art and new tailored compression methods were implemented and evaluated systematically. A part of the system is an image quality based evaluation system for comparison and optimization of data compression methods. Based on the experimental results with real and simulated datasets a suitable compression method was selected for USCT.

The introduced methods combined with the corresponding experimental results are analyzed and discussed in the first part of this chapter. In the second part a quantitative comparison of different compression methods will be given. Finally the proposed image quality estimator and the acceptable compression ratios are concluded.

### **5.1 Discussion**

#### **5.1.1 Multiple scattering and dispersion**

The experimental results for multiple scattering in USCT are shown in section 2.3.4. Based on the analysis of distances between emitters and receivers, diameter of scattering objects and the speed of ultrasound, the structure of B-scans can be explained.

Multiple scattering may affect the image quality but depends strongly on considered magnitude of reflectivity. A large reflection intensity happens for large differences of acoustic impedances and that is not to be expected in the breast in USCT.

The simulations about the attenuation and dispersion of ultrasound pulses in section 2.3.5 show that the ultrasound pulse is deformed due to frequency dependent attenuation and dispersion. Ultrasound pulse is deformed stronger in human tissues than in water. This complicates the correct reconstruction of the images.

### **5.1.2 Image quality estimators**

A reasonable image quality evaluation system was the necessary basis for the search of the best possible data compression in USCT. The performance of standard and newly designed image quality estimators are analyzed with subjective and objective estimations. The advantages and disadvantages of these estimators are compared.

#### **5.1.2.1 No-reference estimators**

The results for no-reference image quality estimators in section 3.3 show that all image quality estimators are insensitive to changed offset values in images, but they have different sensitivities to different distortion types. None of these image quality metrics show reasonable sensitivity to all of the designed distortion types. Therefore the reference based image quality estimators were investigated for the case that a suitable reference image could be found.

#### **5.1.2.2 Standard reference based estimators**

The standard reference based estimators have a low performance for objects with a complex structure as the dataset 6fatRand. Thus the curves of these estimators have a low performance for the dataset 6fatRand as shown in figures from Fig. 4.16 - Fig. 4.22. The values of the scores do not correlate with human perception.

A comparison of the sensitivity for selected reference based estimators (see Table 3.1) shows that AMI and NMI have similar performance. The changes of structure in images cannot be scored efficiently by PSNR.

As shown in section 4.2.1.2, AMI is not suitable for measurement of significant structure changes in images of compressed datasets

compared to the reference image. Thus it is unsuitable for estimating the image quality of datasets compressed at high compression ratios, i.e.  $> 100$ . All standard estimators have disadvantages for scoring some distortions in images of compressed datasets. Therefore a new image quality estimator was searched in this work.

### 5.1.2.3 New image quality estimators

An estimator which correlates well with human perception was searched. Two possible solutions were proposed. First, the design of a new image quality estimator which can overcome the shortcomings of the state-of-the-art image quality estimators. Second, the use of subjective measure as additional measure to get rid of the significantly distorted images of artificial datasets.

**Optical flow** The scores obtained with simulated datasets in Fig. 4.24 with OFintenEtpy do not show the quality of the images as the human perception.

According to the introduction about the optical flow in section 3.4.2, the assumption of optical flow based methods is that the structures of the imaged objects in reference and distorted images are similar. The objects in images of compressed datasets are significantly different from those in the reference image; therefore the optical flow based image quality estimator has a low performance and is not further considered.

**CMM** The committee model based estimator (CMM) combines the sensitivity of the underlying estimators. The performance has been measured as described in section 4.2.1.4 and section 4.2.2.4 for simulated and real datasets, respectively.

An ideal reference was used for CMM. For real datasets the ideal reference is not available. If the ideal reference was designed with the original image and had a high similarity to the imaged objects, the CMM is robust. Unreasonable results were achieved as shown in the experiment with the real dataset for imaged object Breast-phantom3 in section 4.2.2.4, if the ideal reference could not be designed properly in all details of the objects, e.g. a part of the imaged

object was not depicted well in the original image.

The applied distortions are based on empirical observations. To select a suitable set of types and grades of distortions, the characteristics of reconstruction artifacts and compression artifacts have to be considered. The flexible selection of the simulated distortion types and grades makes the CMM capable to score arbitrary distortions, thus it can be used to evaluate very different imaging systems. The compression artifacts vary significantly with the complexity of imaged objects. The image objects with similar structure and acoustic properties have comparable compression artifacts in images of compressed datasets. The optimal estimator in USCT may be obtained for an imaged object with similar structure and acoustic properties as the human breast.

According to human perception the image quality decreases from Fig. 4.14(a) to 4.14(f) for the simulated dataset and from Fig. 4.34(a) to 4.34(e) for the real dataset, respectively. The scores listed in Table 4.1 and Table 4.2 show the performance of different image quality estimators used in CMM. Most of these estimators are inefficient for scoring the images of datasets compressed with DCV, which are serious distortions. The correlation coefficients between CMM and the subjective estimator (i.e. MVS) are two times larger than that for other estimators, thus it has the best consistency with human perception. Based on the high consistency with human perception CMM is used to score the similarity between ideal reference and the image of compressed dataset.

### **5.1.3 Comparison of results with different types of references**

The influences of the implemented reference images on the performances of the image quality estimators are discussed below.

#### **5.1.3.1 Original image as reference**

The theoretical analysis in section 3.5.1 shows that the useful contents in the original image are the contours of the imaged objects, since USCT uses the information of reflected ultrasound signals. These contours are affected by the background noise and the original image has to be improved to be used as a reference image.

### **5.1.3.2 Ideal reference**

The ideal reference has no background noise. The simulated noise is added in the ideal reference to evaluate the denoising ability of the compression methods.

For real datasets the design of an ideal reference is different from that for simulated datasets. The methods for simulated and real datasets were explained in section 3.5.2.3 and 4.2.2.3, respectively. The design of an ideal reference for a real dataset has to be done manually and depends on the experience of the designer.

### **5.1.3.3 Filtered original image as reference**

The abstraction of the contours of the imaged objects in the original image is the basic idea to apply the filtered original images as reference for real datasets. The significant advantages of using the filtered original image are the availability of the original images and the reproducibility of the results. The size and structure for the image filter are selected by the user.

With the filtered original image as reference the experimental results are shown in section 4.2.1.5 for the simulated dataset 6fatRand and in section 4.2.2.2 for the real dataset Breastphantom1. The main tendencies of all curves in Fig. 4.29 and Fig. 4.35 are decreasing with increasing compression ratios. Results show that DWT and Multifractal based method have better performance, in terms of AMI, than the others within a large range of compression ratios. The local maximum of AMI for the Breastphantom1 is located at compression values of 10 to 20. This result is consistent with the human perception.

The results with the filtered original image as reference are compared to that with ideal reference using the standard image quality estimators. The differences between filtered original images and images of compressed datasets are significantly smaller than that between ideal reference and images of compressed datasets. This reduced differences increase the performance of AMI. Therefore the performance obtained with the filtered original image as reference are more similar to the human perception than what is obtained

with an ideal reference.

Based on the advantages of the filtered original image as reference different mother wavelets and the denoising ability of the compression methods were evaluated. The experimental results are shown in section 4.2.1.6 and section 4.4.3, respectively. For noisy datasets local maxima of AMI in Fig. 4.45 are 50% higher than that for images reconstructed with uncompressed datasets. Local maxima are at compression ratios from 10 to 30 depending on different noise levels. These evaluation results have a high consistency with the human perception.

#### **5.1.4 Lossless compression**

Lossless compression methods avoid the loss of information in original datasets.

A new lossless method was developed based on the characteristics of A-scans for higher compression ratios than state-of-the-art lossless methods. The data from real A-scans were used to verify the method. The compression ratio achieved with the proposed cascading bitwise RLE method is about 1.6 for A-scans in experiments. That is about 80 % of the theoretical optimal compression ratio obtained by Shannon theory. The compression ratio with the cascading bitwise RLE is about 10 % larger than that with WinZip V14.0.

Other methods of lossless compression could be theoretically rejected because of poor results, see section 2.4.1 and 2.4.2.

#### **5.1.5 Lossy compression**

Lossy compression was investigated to achieve higher compression ratios than for lossless methods. Most of the tested lossy compression methods in this work contain at the final end run length encoding. The reduction of data may result in a degradation of the USCT images. The process to find a suitable lossy compression method for USCT is as follows:

**In the first step** the adapted lossy compression methods introduced in section 2.5 were tested with synthetic A-scans. These re-

sults have no pulse deformation but different noise grades were applied (see section 4.1.1). The performance of the compression methods were scored with PSNR which shows the distance between original and compressed A-scans. DCV shows higher performance than DWT and IKstd compression methods, since the synthetic A-scans contain no deformation of the ultrasound pulses. Breast tissues have a higher attenuation factor than water as shown in section 2.3.5. Ultrasound wave propagation in breast tissues is frequency dependent, therefore pulse deformation occurs. Compression methods as DWT, which are strongly dependent on pulse deformation, had to be analyzed due to the frequency dependent attenuation for breast tissue.

**In the second step** simulated and real datasets were employed. An ideal reference image can be precisely designed for the simulated dataset to evaluate the image quality. Although there is no noise in the simulated dataset as in the real dataset, the evaluation results for simulated and real datasets are expected to be similar.

**In the third step** the results of subjective evaluation was used. DWT and MultiFractal method have the highest performance due to their time-frequency representation of data. The useful contents in A-scans are separated well from irrelevant parts and are maintained during compression processes with these methods, because the imaged objects become clear in images reconstructed with corresponding compressed datasets.

The IKstd method has a better performance for the dataset bloodbone than for 6fatRand. The imaged objects in dataset bloodbone have a simpler structure than that of 6fataRand. Reflected pulses are not interfered strongly with each other in the A-scans for the dataset bloodbone. For a dataset with a simple structure of the imaged objects and a low level of noise, IK and IKstd are recommended for a high performance of lossy compressions, since the IKstd method is suitable to identify peaks of well separated pulses in A-scans.

DCV has a low performance for compression of USCT datasets. The high sensitivity to pulse deformation limits the utilization of DCV for USCT datasets. Similar results were achieved for both simulated and real datasets. Thus the DCV method was not further consid-

ered for USCT data compression.

**In the fourth step** the objective evaluation of the adapted compression methods were carried out by comparing the obtained scores of the used image quality estimators. The estimator AMI is used for dataset bloodbone in section 4.2.1.2, which has a simple structure. The IKstd method shows a higher AMI than the other methods because of the simple structure of the dataset bloodbone. At low compression ratios, e.g.  $< 30$  the scores of AMI are consistent with the subjective perception.

The starting points of the AMI curves at the lowest compression ratio (shown in Fig. 4.15) are not identical for different compression methods because the decompressed A-scans at the smallest compression ratio are not identical to the original A-scans. Thus images reconstructed with original and compressed datasets are at very small compression ratios not identical. The reason is that the compression and decompression processes of different compression methods results in different quantization errors. The lowest compression ratio should correspond to the case of uncompressed dataset as explained in section 4.2.1.2. This is not correctly handled in conventional algorithm of compression methods in this work.

The local maximum of the AMI curve at low compression ratios indicates that the compression process improves the image quality (see section 4.4.2). This local maximum appears for noisy datasets, since a suitable compression method is capable to keep the useful contents and to reduce the noise. The optimal compression ratio is based on the position of this maximum.

For a more objective evaluation of the compressed datasets with a complex structure, CMM with an ideal reference and AMI with filtered original image as reference were employed. The results for the simulated dataset 6fatRand were shown in section 4.2.1.4 and section 4.2.1.5. DWT and MultiFractal methods have higher performances than other methods. Similar results are achieved with real datasets as Breastphantom2 in section 4.2.2.4 and Breastphantom1 in section 4.2.2.2. The local maximum value of the scores is at a compression ratio of approx. 20.

**Finally** different mother wavelets as a parameter used in DWT were selected. Performance of standard mother wavelets for DWT is compared using the simulated dataset 6fatRand in section 4.2.1.6. The images of compressed datasets have different qualities for different mother wavelets, but all wavelets except Haar showed similar results.

The mother wavelet which is smooth and similar to the coded excitation of the ultrasound pulses has the best performance. Thus the design of a new mother wavelet with high smoothness and similarity to the coded excitation is suggested for improving the performance of data compression DWT in USCT.

## **5.2 Conclusion**

### **5.2.1 Compression**

#### **5.2.1.1 De-noising ability and computational complexity**

The de-noising ability for synthetic A-scans was shown in section 4.1.1. The local maxima of the PSNR curves represent the de-noising abilities of different compression methods. The DCV method show its significant high de-noising ability since there are no pulse deformations in the synthetic A-scans.

The high denoising ability of the DWT method is estimated not only by human perception but also by image quality estimators. The experimental results are shown in section 4.4.1. The maximum value in Fig. 4.45 shows that the DWT method has higher de-noising ability than a band-pass de-noising filter which is applied for preprocessing of A-scans in USCT. As expected, the values and positions of local maxima in Fig. 4.45 are changed with the noise level. For a dataset with a higher noise level the maximum value of AMI can be found at a higher compression ratio. In this case an increasing threshold value is used to remove noise.

The adapted compression methods for datasets are compared based on the denoising ability and the computational complexity. The comparison results are shown in Table 5.1. The computational complexity is defined as low when the number of operation is  $< N^2$  (with  $N$  the length of A-scans), otherwise high. The DWT, MultiFractal and IKstd have similar good performance, therefore the properties and the performance of these methods are compared further.

Name	Computational complexity relative (High/Low)	Denoising ability relative (High/Low)
DWT	Low	High
MultiFractal	Low	High
DCV	Low	Low
DCT	High	High
IKstd	Low	High
IK	Low	Low
WavePDT	High	High
Threshold	Low	Low

Table 5.1: Comparison of state-of-the-art compression methods.

### 5.2.1.2 Property and performance

Based on the experimental results of adapted compression methods, their performance for USCT is analyzed. A comparison of their characteristics as well as advantages and disadvantages are listed in Table 5.2.

The DWT and MultiFractal methods have a better performance than all other compression methods, because the discrete wavelet transformation has the ability to represent the information in the time and frequency domain and is suitable for analysis of the non stationary signals. IKstd and IK methods have a low computational complexity, but the precise position of ultrasound pulses may not be found. Although the DCV method achieves a high compression ratio for synthetic A-scans (in section 4.1.1), this method is sensitive to pulse deformation. WavePDT is used for achievement of a high compression ratio, but it has a significantly higher computational complexity than other compression methods. The DCT method has a low performance because of neglecting the pulse shape informa-

Name	Short introduction	Advantages	Disadvantages
DWT	Quantize coefficients from discrete wavelet transform	Fast; Low sensitivity to noise and pulse deformation	-
MultiFractal	Adjust coefficients from discrete wavelet transform	Low sensitivity to noise	-
IKstd	Peak detection with fixed neighborhood relation	Low sensitivity to pulse shape deformation	High sensitivity to noise
IK	Peak detection with various neighborhood relation	High compression ratio for simple objects	Hard to control compression ratio
DCV based	Convolute with deconvolution filter from coded excitation	Fastest; pulse shape dependent	High sensitivity to noise and pulse deformation
DCT	Quantize and code coefficients from DCT	Keep frequency component with high value	Influenced by distorted frequency component with high value
WavePDT	Search local maximum of wavelet coefficients from CWT	Pulse detection possible	High computational complexity; pulse parameter sensitive
Threshold	Quantization with hard threshold method and coding	Simplest	Low performance for signal smaller than noise

Table 5.2: Comparison of compression methods.

tion in A-scans. Threshold is simple to be implemented, but useful contents with smaller amplitudes than the threshold are lost.

Based on the analysis in Table 5.1 and Table 5.2, the DWT and MultiFractal methods are more feasible than all other used methods for compression of USCT datasets.

### 5.2.2 Image quality estimators

An ideal reference is expected to have a better performance than that of original images for using as a reference image. But it is difficult to achieve an ideal reference for real datasets. The manually designed ideal reference for real datasets is not reproducible and limits the implementation of an ideal reference based estimator.

The standard no-reference estimators are not suitable for evaluating images of compressed datasets in USCT. CMM has better performance than standard reference and optical flow based estimators for evaluation of USCT images. The advantage of CMM is the flexibility of selecting underlying estimators for evaluated images.

**In conclusion, a new image quality estimator CMM** is proposed for comparison of images influenced by data compression in USCT. The CMM utilizes the advantages of state-of-the-art image quality estimators by combining them to a generalized committee model and parameterizes the model with simulated distortions. Based on the experimental results from 1200 images of compressed simulated and real datasets, the CMM has the ability to score the distortion types in images caused by data compression in USCT and has a higher correlation with human perception than all other state-of-the-art image quality estimators.

### 5.2.3 Acceptable data compression in USCT

A **new lossless compression method** based on the characteristics of ultrasound signals in USCT was designed for improvement of compression ratios up to 80 % of the theoretical limit yielding a compression of factor 1.6.

The discrete wavelet transform based compression method among the state-of-the-art compression methods proves to be optimal for data compression in USCT with a low computational complexity, a

significant reduction of data, a high quality of reconstructed images and a high denoising ability. A compression ratio of 10 to 15 is feasible for real ultrasound imaging of the breast with the version of the USCT 2006.

# Bibliography

- [1] World Health Organization (WHO) Media Center, "Fact sheet no. 297: Cancer, retrieved on 2007-04-26," 2007.
- [2] D. B. Thomas, D. L. Gao, R. M. Ray, W. W. Wang, C. J. Allison, F. L. Chen, P. Porter, Y. W. Hu, G. L. Zhao, L. D. Pan, W. Li, C. Wu, Z. Coriaty, I. Evans, M. G. Lin, H. Stalsberg, and S. G. Self, "Randomized trial of breast self-examination in shanghai: Final results," *J. Natl. Cancer Inst.*, vol. 94(19), pp. 1445–57, 2002.
- [3] J. Austoker, "Breast self examination," *BMJ*, vol. 326, pp. 1–2, 4 January 2003.
- [4] M. Morrow, "Magnetic resonance imaging in breast cancer: One step forward, two steps back?," *JAMA*, vol. 292 (22), pp. 2779–80, 2004.
- [5] C.-K. Yeh, S.-J. Miao, W.-C. Fan, and Y.-S. Chen, "Automatic ultrasonic breast lesions detection using support vector machine based algorithm," *Proceedings of the SPIE*, pp. 6513–6517, March. 2007.
- [6] R. Stotzka, H. Widmann, T. O. Mueller, K. Schlote-Holubek, H. Gemmeke, N. V. Ruiter, and G. Goebel, "Prototype of a new 3d ultrasound computer tomography system: Transducer design and data recording," *Proceedings of the SPIE*, vol. 5373, pp. 70–79, apr 2004.
- [7] N. V. Ruiter, G. F. Schwarzenberg, M. Zapf, R. Liu, R. Stotzka, and H. Gemmeke, "3D ultrasound computer tomography: Results with a clinical breast phantom," *IEEE Ultrasonics Symposium*, vol. 2-6, pp. 989–992, Oct. 2006.
- [8] N. V. Ruiter, R. Stotzka, T. O. Mueller, R. Liu, and H. Gemmeke, "State of the art and challenges in ultrasound computer tomography," *EMBEC05*, 2005.

- [9] T. Strutz, "Datenkompression - Grundlagen, Verfahren und deren Anwendung in der Verarbeitung von Graustufen- und Farbbildern." Habilitationsschrift, Universität Rostock, April 2002. ISBN:3-89825-575-1.
- [10] D. Salomon, *A guide to compression methods*. New York: Springer-Verlag, 2002. ISBN:0-387-95260-8.
- [11] K. Sayood, *Introduction to Data Compression*. Morgan Kaufmann Publishers, 1996.
- [12] S. Wolfram, *A New Kind of Science. chapter 10: Processes of Perception and Analysis. Section: Data Compression. Page:1069*. Champaign, IL: Wolfram Media, May 14, 2002. ISBN 1-57955-008-8.
- [13] D. Salomon, *Data Compression, The Complete Reference*. Northridge, USA: Springer, 3 ed., 2004. ISBN:0-387-40697-2.
- [14] I. Wikipedia Foundation, "Principal components analysis," 2007.
- [15] C. Delgorge, P. Vieyres, G. Poisson, C. Rosenberger, and P. Arbeille, "Comparative survey of ultrasound images compression methods dedicated to a tele-echography robotic system," *Proceeding of the IEEE EMBS 2001 International Conference*, 2001.
- [16] J. Ziv and A. Lempel, "Compression of individual sequences via variable-rate coding," *IEEE Transactions on Information Theory*, vol. 24, no. 5, pp. 530–536, 1978.
- [17] C. E. Shannon, *Claude E. Shannon: Collected Papers*. NJ: Institute of Electrical and Electronics Engineers, Inc., 1993.
- [18] C. Shannon, "A mathematical theory of communication," *The Bell System Technical Journal*, vol. 27, pp. 379–423, July, 1948.
- [19] D. A. Huffman, "A method for the construction of minimum redundancy codes," *Proceedings of the IRE*, vol. 40, pp. 1098–1101, 1952.
- [20] R. Asraf, "Diagnostically lossless compression-2 of medical images," *Proceedings of the 1st Distributed Diagnosis and Home Healthcare (D2H2) Conference*, April 2-4, 2006.

- [21] S. Grgic, M. Mrak, M. Grgic, and B. Zovko-Cihlar, "Comparative study of JPEG and JPEG2000 image coders," *Proceedings of the 17th Conference on Applied Electromagnetics and Communications*, pp. 109–112, October 2003.
- [22] D. T. Hoang and J. S. Vitter, *Efficient Algorithms for MPEG Video Compression*. New York: John Wiley and Sons, Inc., 2002. ISBN:0-471-37942-5.
- [23] J. Watkinson, *MPEG Handbook*. Focal Press, 2001.
- [24] D. Salomon, *Data Compression*. London: Springer, 2007.
- [25] S. G. Mathen, "Wavelet transform based adaptive image compression on FPGA," Master's thesis, University of Calicut, 1996.
- [26] Z. H. Zeng and I. G. Cumming, "SAR image data compression using a tree-structured wavelet transform," *IEEE Transactions on Geoscience and Remote Sensing*, vol. 39, no. 3, 2001.
- [27] Z. Yao, G. F. Margrave, and E. V. Gallant, "Optimal time-delay spiking deconvolution and its application in the physical model measurement," *CREWES Research Report*, vol. 11, 1999.
- [28] E. J. Candes and M. B. Wakin, "An introduction to compressive sampling," *IEEE Signal Processing Magazine*, pp. 21–30, 2008.
- [29] M. Raz, S. K. Setarehdan, and M. P. Jabbedar, "Design a data compression method in a tele-ultrasound system," *International Symposium on Telecommunications (IST)*, August 2003.
- [30] T. Mueller, R. Stotzka, N. Ruiter, K. Schlote-Holubek, and H. Gemmeke, "3D ultrasound-computertomography: Data acquisition hardware," in *IEEE Nuclear Science Symposium and Medical Imaging Conference*, 2004.
- [31] M. P. Wachowiak, A. S. Elmaghraby, R. Smolikova, and J. M. Zurada, "Classification and estimation of ultrasound speckle noise with neural networks," *BIBE '00: Proceedings of the 1st IEEE International Symposium on Bioinformatics and Biomedical Engineering*, p. 245, 2000.
- [32] R. Czerwinski, D. Jones, and J. O'Brien, W.D., "Detection of lines and boundaries in speckle images-application to medical

- ultrasound,” *Medical Imaging, IEEE Transactions on*, vol. 18 Issue:2, pp. 126–136, 1999.
- [33] X. Hao, S. Gao, and X. Gao, “A novel multiscale nonlinear thresholding method for ultrasonic speckle suppressing,” *Medical Imaging, IEEE Transactions on*, vol. 18 Issue:9, pp. 787–794, 1999.
- [34] J. Goodman, “Statistical properties of laser speckle patterns,” *Laser Speckle and Related Phenomena*, vol. 9, pp. 9–75, 1984.
- [35] T. Srinivasan, V. Srinivasan, and B. Suresh, “Speckle noise model and its optional removal in ultrasound 2d b-scan images,” *Engineering in Medicine and Biology Society, 1988. Proceedings of the Annual International Conference of the IEEE*, vol. 1, p. 466, 1988.
- [36] K. Robinson and J. Miao, “Three dimensional coherent X-ray diffraction microscopy,” *MRS Bulletin*, vol. 29, pp. 177–181, 2004.
- [37] V. Behar, D. Adam, and Z. Friedman, “A new method of spatial compounding imaging,” *Ultrasonics*, vol. 41(5), pp. 377–384, 2003.
- [38] R. Schnell, *Rekonstruktion von Reflexionsbildern unter Berücksichtigung der Schallgeschwindigkeitsverteilung für 3D Ultraschall Computertomographie*. Forschungszentrum Karlsruhe in der Helmholtz-Gemeinschaft, Institut für Prozessdatenverarbeitung und Elektronik: Master Thesis, 2006.
- [39] B. A. Auld, *Chapter 1 Particle Displacement and Strain, Chapter 2 Stress and the Dynamical Equation. Acoustic Fields and Waves in Solids*. Stanford University: A Wiley-interscience Publication, 1973. ISBN:0-471-03700-1.
- [40] S. Barnett and G. Kossoff, *Safety of Diagnostic Ultrasound*. Carnforth, UK: Parthenon Publishing, 1998.
- [41] O. Dössel, “Bildgebende Verfahren in der Medizin II,” in *Bildgebende Verfahren Course Notes*, (Institut für Biomedizinische Technik, Universität Karlsruhe), Karlsruhe University, 2005.
- [42] V. Le Floch, D. McMahon, G. Luo, A. Cohen, J. Kaufman, E. Shane, and S. RS., “Ultrasound simulation in the distal radius using clinical high-resolution peripheral-ct images,” *Ultrasound in Medicine and Biology*, vol. 34, 2008.

- [43] F. A. Duck, *Physical Properties of Tissue: A Comprehensive Reference Book*. Royal United Hospital and University of Bath, Bath, England: Academic Press INC., 1990.
- [44] R. Millner, *Section 1.2 Wellenausbreitung in elastischen Medien. Ultraschalltechnik: Grundlagen und Anwendungen*. Altenburg: Weinheim : Physik-Verl., 1987.
- [45] I. CyberLogic, "Software for 3d ultrasound simulation," 2006.
- [46] T. L. Szabo, "Diagnostic ultrasound imaging," Newburyport, Massachusetts, 2004. chapter 3 Acoustic Wave Propagation, chapter 4 Attenuation.
- [47] A. Guerrero, C. Mailhes, and F. Castanie, "First results on new modeling-based ECG data compression methods," *Engineering in Medicine and Biology Society, 1998. Proceedings of the 20th Annual International Conference of the IEEE*, vol. 1, pp. 194–197, 1998.
- [48] F. Simonetti, "Multiple scattering: The key to unravel the subwavelength world from the far-field pattern of a scattered wave," *Physical Review E73*, no. 036619, 2006.
- [49] P. M. Morse, *Theoretical Acoustics*. Massachusetts Institute of Technology: McGraw-Hill, Inc., 1968.
- [50] NDT resource center, "Introduction to ultrasonic testing: Data presentation," 2007.
- [51] A. R. Selfridge, "With further discription for the measurement method," *IEEE Transactions On Sonics and Ultrasonics*, vol. SU-32, no. 3, pp. 381–394, 1985.
- [52] P. N. T. Wells, "Review: Absorption and dispersion of ultrasound in biological tissue," *Ultrason. Medl Biol.*, vol. 1, pp. 369–376, 1975.
- [53] P. He, "Simulation of ultrasound pulse propagation in lossy media obeying a frequency power law," *IEEE Transaction on Ultrasonics, Ferroelectrics and Frequency Control*, vol. 45, p. 1, January 1998.
- [54] M. Liebler, S. Ginter, T. Dreyer, and R. E. Riedlinger, "Full wave modelling of therapeutic ultrasound: Efficient time-domain implementation of the frequency power-law attenuation," *Acoustical Society of America Journal*, vol. 116, pp. 2742–2750, 11 2004.

- [55] L. Brillouin, *Ultraschalltechnik : Grundlagen und Anwendungen*. New York and London: Academic Press Inc., 1960.
- [56] J. Daintith, *WinZip: A Dictionary of Computing 2004*. Oxford University: Oxford University Press, 2004.
- [57] D. Salomon, *Data Compression: The Complete Reference*. New York: Springer-Verlag, 1998. ISBN:0-387-95045-1.
- [58] C. S. Burrus, J. H. McClellan, A. V. Oppenheim, T. W. Parks, R. Schafer, and H. Schuessler, "Computer-based exercises for signal processing using MATLAB," 1994.
- [59] M. Balzer and H. Stripf, "Online data reduction system with DSPs," *6th International Symposium on Signal Processing and its Applications*, 1995.
- [60] R. M. Cramblitt and et al., "Ultrasound image compression exploiting image formation modles," *IEEE International Ultrasonics Symposium*, 1996.
- [61] K. R. Rao and P. Yip, *Discrete Cosine Transform: Algorithms, Advantages, Applications*. Boston: Academic Press, 1990. discret cosine transform.
- [62] N. Ahmed, T. Natarajan, and K. R. Rao, "Discrete cosine transform," *IEEE Transactions on Computers*, vol. C-23, no. 90-93, 1974.
- [63] L. Cohen, "Time-frequency distributions - a review," *Proceedings of the IEEE*, vol. 77(7), pp. 941-980, 1989.
- [64] P. S. Addison, *The Illustrated Wavelet Transform Handbook*. Institute of Physics Publishing, 2002.
- [65] A. L. Goldberger, L. A. N. Amaral, L. Glass, J. M. Hausdorff, P. C. Ivanov, R. G. Mark, J. E. Mietus, G. B. Moody, C.-K. Peng, and H. E. Stanley, "PhysioBank, PhysioToolkit, and PhysioNet: Components of a new research resource for complex physiologic signals," *Circulation*, vol. 101, no. 23, pp. e215-e220, 2000 (June 13). Circulation Electronic Pages: <http://circ.ahajournals.org/cgi/content/full/101/23/e215>.
- [66] P. Legrand and J. L. Veheil, "Local regularity-based image denoising," *International Coference on Image Processing 2003*, vol. 3, pp. III-377-80, 14-17 Sept. 2003.
- [67] J. L. Veheil and B. Guiheneuf, "Multifractal image denoising," *SCIA'97*, 1997.

- [68] M. Weber, *Robuste Pulsdetektion für die Ultraschall-Computertomographie*. Forschungszentrum Karlsruhe in der Helmholtz-Gemeinschaft, Institut für Prozessdatenverarbeitung und Elektronik: Master Thesis, 2006.
- [69] G. Cardoso and J. Saniie, "Ultrasonic data compression via parameter estimation," *IEEE Transaction on Ultrasonics, Ferroelectrics and Frequency Control*, vol. 52(2), 2005.
- [70] A. Graps, "An introduction of wavelets," *IEEE computational science and engineering*, vol. 2, 1995.
- [71] J. W. Cooley and J. W. Tukey, "An algorithm for the machine calculation of complex fourier series," *Mathematics of Computation*, pp. 297–301, 1965.
- [72] L. Rabiner and B. Gold, *Theory and Application of Digital Signal Processing*. Englewood Cliffs, NJ: Prentice-Hall, 1975.
- [73] J. Kerekes, "Image data compression," *Geoscience and Remote Sensing Society Instrumentation and Future Technologies Committee*, 2002. Technical Briefs, <http://www.ewh.ieee.org/soc/grss/ift/kerek19.html>.
- [74] A. Klibanov, "Ligand-carrying gas-filled microbubbles: Ultrasound contrast agents for targeted molecular imaging," *Bioconjug Chem.*, vol. 16, pp. 9–17, 2005.
- [75] J. Lindner, "Microbubbles in medical imaging: current applications and future directions," *Nat Rev Drug Discov.*, vol. 3, pp. 527–532, 2002.
- [76] C. Delgorge, C. Rosenberger, G. Poisson, and P. Vieyres, "Evaluation of the quality of ultrasound image compression for a robotic tele-echographic system," *Computers in Cardiology*, pp. 775–778, 2005.
- [77] Y. L. Huang, W. M. Chen, and C. C. Tao, "Evaluation of image compression for computer-aided diagnosis of breast tumors in sonography," *SPIE Visual Communications and Image Processing*, vol. 5960, 2006.
- [78] T. A. Lasko, J. Bhagwat, K. Zou, and L. Ohno-Machado, "The use of receiver operating characteristic curves in biomedical informatics," *Journal of Biomedical Informatics*, vol. 38(5), pp. 404–415, Oct. 2005.

- [79] Z. Bojkovic, "Image quality estimation in sub-band coding techniques based on human visual system," *International Conference on Communication Technology Proceedings, ICCTapos*, vol. 2, pp. 651 – 653, 5-7 May 1996.
- [80] Z. Wang and A. C. Bovik, "Why is image quality assessment so difficult?," *IEEE International Conference on Acoustics, Speech, and Signal Processing*, 2002.
- [81] I. Avcibas, B. Sankur, and K. Sayood, "Statistical evaluation of image quality measures," *Journal of Electronic Imaging*, vol. 11(2), p. 206-223, April 2002.
- [82] H. Lopez, M. H. Loew, and D. Goodenough, "Objective analysis of ultrasound images by use of a computational observer," *Medical Imaging, IEEE Transactions on*, vol. 11, pp. 496-506, Dec 1992.
- [83] S. D. Pye, W. Ellis, and T. MacGillivray, "Medical ultrasound: A new metric of performance for greyscale imaging," *Journal of Physics*, vol. 1, pp. 187-192, 2004.
- [84] J. Thijssen, G. Weijers, and C. de Korte, "Objective performance testing and quality assurance of medical ultrasound equipment," *Ultrasound in Medicine and Biology*, vol. 33, pp. 460-471, Feb 2007.
- [85] Z. Wang and A. C. Bovik, "A universal image quality index," *IEEE Signal Processing Letters*, vol. 9, no. 3, pp. 81-84, 2002.
- [86] Z. Wang and A. C. Bovik, "No-reference perceptual quality assessment of JPEG compressed images," *IEEE International Conference on Image Processing*, 2002.
- [87] J. Dusek and K. Roubik, "Simulation of human visual perception properties using the human visual system model," *Proceedings of the SPIE*, vol. 5036, pp. 204-210, 07/2003.
- [88] Z. Wang and A. Bovik, *The Handbook of Image and Video Processing*. Austin, Texas, USA: Academic Press, 2 ed., 2005.
- [89] H. R. Sheikh, A. C. Bovik, and L. K. Cormack, "No-reference quality assessment using natural scene statistics: JPEG2000," *IEEE Transactions on Image Processing*, vol. 14, pp. 1918-1927, December 2005.

- [90] VQGE, "Final report from the video quality experts group on the validation of objective models of video quality assessment," tech. rep., Video Quality Experts Group, U.S. Dept. of Commerce, NTIA/ITS, Boulder, Colorado U.S.A., 2003.
- [91] R. Miri, S. K. Setarehdan, and P. J. Maralani, "Design a data compression method in a tele-ultrasound system," *IST2003*, 2003.
- [92] P. W. Josien, J. B. Pluim, A. Maintz, and M. A. Viergever, "Mutual information based registration of medical images: a survey," *IEEE Transactions on Medical Imaging*, vol. 22(8), pp. 986–1004, Aug. 2003.
- [93] H. Sheikh, M. Sabir, and A. Bovik, "A statistical evaluation of recent full reference image quality assessment algorithms," *Image Processing, IEEE Transactions on*, vol. 15, pp. 3440–3451, Nov. 2006.
- [94] M. Wirth, M. Frascini, M. Masek, and M. Bruynooghe, "Performance evaluation in image processing," *EURASIP Journal on Applied Signal Processing*, vol. 2006, pp. 1–3, April 2006.
- [95] K. Matkovic, L. Neumann, A. Neumann, T. Psik, and W. Purgathofer, "Global contrast factor—a new approach to image contrast," in *Computational Aesthetics in Graphics, Visualization and Imaging 2005*, (Girona, Spain), pp. may, 159–168, Eurographics Association, 2005.
- [96] J.-L. Starck, F. Murtagh, E. J. Candes, and D. L. Donoho, "Gray and color image contrast enhancement by the curvelet transform," *IEEE TRANSACTIONS ON IMAGE PROCESSING*, vol. 12, no. 6, pp. 706–717, 2003.
- [97] D. Sitter, J. Goddard, and R. Ferrell, "Method for the measurement of the modulation transfer function of sampled imaging systems from bar-target patterns," *Applied Optics*, vol. 34, no. 4, pp. 746–751, 1995.
- [98] C. Dickinson, "An evaluation of the current state of digital photography," Master's thesis, Center for Imaging Science, Rochester Institute of Technology, May 1999.
- [99] S. Inoue and K. R. Spring, *Video Microscopy: The Fundamentals (The Language of Science)*. Plenum Publishing Corporation, 1997. chapter 5.4, MTF.

- [100] G. D. Boreman, *Modulation transfer function in optical and electro-optical systems*. SPIE Press, illustrated ed., 2001.
- [101] O. Dössel, *Bildgebende Verfahren in der Medizin: von der Technik zur medizinischen Anwendung*. Institut für Biomedizinische Technik, Universität Karlsruhe: Springer-Verlag Berlin Heidelberg, 2000.
- [102] J. P. W. Pluim, J. B. A. Maintz, and M. A. Viergever, "Mutual information based registration of medical images: a survey," *IEEE Transaction on Medical Imaging*, vol. XX(Y), 2003.
- [103] K. An, J. Sun, and W. Du, "Homogeneity based image objective quality metric," *Intelligent Signal Processing and Communication Systems 2005*, vol. E89-D, pp. 649–652, Dec. 2005.
- [104] Y. Guo and C. C. Lu, "Multi-modality image registration using mutual information based on gradient vector flow," *18th International Conference on Pattern Recognition*, pp. 697–700, 2006.
- [105] C. Xu and J. L. Prince, "Generalized gradient vector flow external forces for active contours," *18th International Conference on Pattern Recognition*, vol. 71, pp. 131–139, 1998.
- [106] E. Haber and J. Modersitzki, "Beyond mutual information: A simple and robust alternative," *Springer Berlin Heidelberg*, pp. 350–354, March 2005.
- [107] T. Camus, "Real-time quantized optical flow," *Computer Architectures for Machine Perception*, pp. 126–131, 1995.
- [108] J. Barron and N. Thacker, "Tutorial: Computing 2d and 3d optical flow," 2005.
- [109] B. Horn and B. Schunck, "Determining optical flow," 1981.
- [110] B. K. Horn and B. G. Rhunckd, "Determining optical flow," *Artificial Intelligence*, vol. 17, pp. 185–203, 1981.
- [111] M. Perrone, *Improving Regression Estimation: Averaging Methods for Variance Reduction with Extension to General Convex Measure Optimization*. PhD thesis, Department of Physics, Brown University, May, 1993.
- [112] M. Guidolin and C. F. Na, "The economic and statistical value of forecast combinations under regime switching: An application to predictable us returns," 2006.

- [113] J. Bates and C. Granger, *Essays in Econometrics: Spectral Analysis, Seasonality, Nonlinearity, Methodology, and Forecasting*. New York: Cambridge University Press, 2001.
- [114] P. W. Munro and B. Parmanto, "Competition among networks improves committee performance," *NIPS*, pp. 592–598, 1996.
- [115] K. K. Aggarwal, Y. Singh, P. Chandra, and M. Puri, "An expert committee model to estimate lines of code," *ACM SIGSOFT Software Engineering Notes*, vol. 30(5), pp. 1–4, Sep. 2005.
- [116] C. M. Bishop and G. E. Hinton, *Neural Networks for Pattern Recognition*. Edinburgh University: Oxford University Press, 1995.
- [117] S. Chatterjee and A. S. Hadi, "Influential observations, high leverage points, and outliers in linear regression," *Statistical Science*, vol. 1(3), pp. 379–393, Aug. 1986.
- [118] R. D. Cook, *Residuals and Influence in Regression*. New York: Chapman and Hall, 1982.
- [119] R. Plackett, "Some theorems in least squares," *Biometrika*, vol. 37 No.1/2, pp. 149–157, Jun, 1950.
- [120] J. Cohen, P. Cohen, S. West, and L. Aiken, *Applied Multiple Regression/Correlation Analysis for the Behavioural Sciences*. New York: Hillsdale NJ: Lawrence Erlbaum Associates, 2nd ed., 2003.
- [121] S. Cho, S. Choi, and P. Wong, "Data selection based on Bayesian error bar," *6th International Conference on Neural Information Processing*, vol. 1, pp. 418–422, 1999.
- [122] M. Born, *Principles of Optics*. Cambridge University Press, 1997.
- [123] M. Weber and et al., "Ultraschallsimulation für die Ultraschall-Computertomographie," *BVM2006*, vol. 9, pp. 439–443, 2006.
- [124] P. P. Delsanto, R. S. Schechter, and R. B. Mignogna, "Connection machine simulation of ultrasonic wave propagation in materials III: The three-dimensional case," *Wave Motion*, vol. 26, no. 4, pp. 329–339(11), 1997.

- [125] G. Takas and B. Pataki, "Fast detection of mammographic masses with difficult case exclusion," *IEEE Workshop on Intelligent Data Acquisition and Advanced Computing Systems: Technology and Applications*, pp. 424–428, 5-7 September 2005.
- [126] R. Kaas, R. Kroger, J. L. Peterse, A. A. M. Hart, and S. H. Muller, "The correlation of mammographic-and histologic patterns of breast cancers in brca1 gene mutation carriers, compared to age-matched sporadic controls," *European Radiology*, vol. 16(12), pp. 2842–2848, December 2006.
- [127] A. M. Bowcock, *Breast Cancer: Molecular Genetics, Pathogenesis, and Therapeutics (Contemporary Cancer Research)*. Washington University School of Medicine, St. Louis, MO: Humana Press, 1999.
- [128] J. E. Bresenham, "An incremental algorithm for digital plotting," *ACM National Conference*, 1963.
- [129] A. Oppenheim and R. Schaffer, *Discrete-Time Signal Processing*. Englewood Cliffs: Prentice-Hall, 1989.
- [130] T. Parks and C. Burrus, *Digital Filter Design*. New York: John Wiley, 1987.

# Resume

**Given name:** Rong            **Family name:** Liu  
**Data of birth:** 20-03-1975    **Highest degree:** Diplom  
**Place of birth:** Xi'an, China    **Nationality:** P.R.China

## Education

1990-1994    Xi'an Middle School  
  
1994-1998    Department of Electrical Engineering, Xi'an Jiaotong University  
  
                 Bachelor's degree in Electrical Machinery, Apparatus and Control  
  
2000-2003    Department of Electrical Engineering  
                 and Information Technology, University Karlsruhe  
  
                 Diplom's degree in Communications Engineering Lab

## Working experience

2003-2008    PhD work  
                 Institute for Data Processing and Electronics  
                 Institute of Biomedical Engineering  
  
2008-present    Herterkom GmbH

## Publication

1. R. Liu, Y. Shang, F. B. Sachse, and O. Dössel, "3D active surfaces for segmentation of medical image data: Assessment of different image forces," Biomedizinische Engineering, vol. 48, pp. 28-29, 2003.
2. R. Liu, N. V. Rüter, R. Stotzka, H. Stripf, H. Gemmeke, and A. Wardana, "Wavelet, multifractal and spiking deconvolution

based signal compression for ultrasound signals in medical imaging, " BMT2005, 2005.

3. N. V. Ruiter, R. Stotzka, T. O. Mueller, R. Liu, and H. Gemmeke, "State of the art and challenges in ultrasound computer tomography, " EMBEC05, 2005.
4. N. V. Ruiter, G. F. Schwarzenberg, M. Zapf, R. Liu, and H. Gemmeke, "3D ultrasound computer tomography: Results with a clinical breast phantom, " IEEE Ultrasonics Symposium, vol. 2-6, pp. 989-992, Oct. 2006.
5. R. Liu, N. V. Ruiter, M. Zapf, R. Stotzka, M. Weber, and H. Gemmeke, "New assessment system for data compression in ultrasound computer tomography, " BioMED 2007, vol. Proceeding, p. 468, Feb. 2007.